Enhancing power and fuel generation efficiency in solid oxide electrochemical cells via advanced electrode materials design

by

Liyang Fang

B.S., East China University of Science and Technology, 2019
M.S., Rutgers University, 2021

AN ABSTRACT OF A DISSERTATION

submitted in partial fulfillment of the requirements for the degree

DOCTOR OF PHILOSOPHY

Tim Taylor Department of Chemical Engineering
Carl R. Ice College of Engineering

KANSAS STATE UNIVERSITY
Manhattan, Kansas

2024

Abstract

Addressing the severe impacts of climate change necessitates a profound overhaul of our current energy system, which includes transitioning away from carbon-intensive fossil fuels and embracing low-carbon alternatives. This transformation involves a range of strategies, including deploying more renewable energy sources as well as adopting energy-efficient technologies, and building sustainable infrastructure. The solid oxide electrochemical cells (SOCs) stand out as a highly promising clean energy technology that offers several benefits, showing significant potential to play a pivotal role in the transition towards a sustainable, low-carbon energy future.

Intermediate temperature SOCs can convert fuels to electricity in fuel cell mode and produce various fuels from renewable electricity working as electrolyzers. A key issue in the development of SOCs is the sluggish oxygen reduction reaction (ORR) and oxygen evolution reaction (OER). Double perovskite $PrBa_{0.5}Sr_{0.5}Co_{1.5}Fe_{0.5}O_{5+\delta}$ (PBSCF) is known to have high oxygen mobility and excellent surface exchange properties at intermediate temperatures. And based on conventional PBSCF material, we successfully designed a hybrid electrode material which significantly enhanced the catalytic activities in the ORR/OER processes and drastically improved the performance. Our hybrid electrode showed great potential as a high-performance oxygen electrode for next generation intermediate temperature SOCs.

CO_2 electrolysis is considered as another promising technology base for the development of sustainable energy systems, as it has the potential to facilitate the attainment of carbon neutrality. However, despite its potential, the electro-catalytic activity of the negative electrode in CO_2 electrolysis remains a challenge, thereby hindering its performance and commercial viability. As such, there exists a pressing need to develop a negative electrode characterized by high catalytic activity for CO_2 adsorption, dissociation, and reduction. Here we report a Ni and

Co co-doping strategy to realize the in situ exsolution of Ni-Co alloy nanoparticles on the surface of $Sm_{0.2}Ce_{0.2}O_{2-\delta}$ (SDC) as a cathode material for SOECs. The doping ratio of Ni-Co was optimized and its effect on physicochemical and electrochemical properties were systemically studied. Moreover, the synergetic effect of Ni-Co alloy was highlighted when compared to single metallic dopant. By tuning the dopant types and concentration, SOECs equipped with the optimized cathode, SDC doped with 25% Ni-Co (SDCNiCo25), achieved a superior current density of 2.7 A cm^{-2} at 750 °C, 1.5 V.

Enhancing power and fuel generation efficiency in solid oxide electrochemical cells via advanced electrode materials design

by

Liyang Fang

B.S., East China University of Science and Technology, 2019
M.S., Rutgers University, 2021

A DISSERTATION

submitted in partial fulfillment of the requirements for the degree

DOCTOR OF PHILOSOPHY

Tim Taylor Department of Chemical Engineering
Carl R. Ice College of Engineering

KANSAS STATE UNIVERSITY
Manhattan, Kansas

2024

Approved by:

Major Professor
Dr. Chuancheng Duan

Copyright

Abstract

Addressing the severe impacts of climate change necessitates a profound overhaul of our current energy system, which includes transitioning away from carbon-intensive fossil fuels and embracing low-carbon alternatives. This transformation involves a range of strategies, including deploying more renewable energy sources as well as adopting energy-efficient technologies, and building sustainable infrastructure. The solid oxide electrochemical cells (SOCs) stand out as a highly promising clean energy technology that offers several benefits, showing significant potential to play a pivotal role in the transition towards a sustainable, low-carbon energy future.

Intermediate temperature SOCs can convert fuels to electricity in fuel cell mode and produce various fuels from renewable electricity working as electrolyzers. A key issue in the development of SOCs is the sluggish oxygen reduction reaction (ORR) and oxygen evolution reaction (OER). Double perovskite $PrBa_{0.5}Sr_{0.5}Co_{1.5}Fe_{0.5}O_{5+\delta}$ (PBSCF) is known to have high oxygen mobility and excellent surface exchange properties at intermediate temperatures. And based on conventional PBSCF material, we successfully designed a hybrid electrode material which significantly enhanced the catalytic activities in the ORR/OER processes and drastically improved the performance. Our hybrid electrode showed great potential as a high-performance oxygen electrode for next generation intermediate temperature SOCs.

CO_2 electrolysis is considered as another promising technology base for the development of sustainable energy systems, as it has the potential to facilitate the attainment of carbon neutrality. However, despite its potential, the electro-catalytic activity of the negative electrode in CO_2 electrolysis remains a challenge, thereby hindering its performance and commercial viability. As such, there exists a pressing need to develop a negative electrode characterized by high catalytic activity for CO_2 adsorption, dissociation, and reduction. Here we report a Ni and

Co co-doping strategy to realize the in situ exsolution of Ni-Co alloy nanoparticles on the surface of $Sm_{0.2}Ce_{0.2}O_{2-\delta}$ (SDC) as a cathode material for SOECs. The doping ratio of Ni-Co was optimized and its effect on physicochemical and electrochemical properties were systemically studied. Moreover, the synergetic effect of Ni-Co alloy was highlighted when compared to single metallic dopant. By tuning the dopant types and concentration, SOECs equipped with the optimized cathode, SDC doped with 25% Ni-Co (SDCNiCo25), achieved a superior current density of 2.7 A cm^{-2} at 750 °C, 1.5 V.

Table of Contents

List of Figures xii
List of Tables xvii
Acknowledgements xviii
Chapter 1 - Introduction 1
1.1 Solid oxide electrochemical cells 1
1.1.1 Introduction to SOCs 1
1.1.2 Current challenges 4
1.1.3 Potential approaches 5
1.2 CO_2 electrolysis in solid oxide electrolysis cells (SOECs) 8
1.2.1 Introduction to CO_2 SOEC 8
1.2.2 Current challenges 10
1.2.3 Recent developments of cathode materials 11
Chapter 2 - Materials and Methods 14
2.1 Design of high-performance SOCs with a novel hybrid oxygen electrode 14
2.1.1 Material synthesis and characterization 14
2.1.1.1 $Pr_{1.39}Ba_{0.14}Sr_{0.53}Co_{1.48}Fe_{0.76}O_{6-\delta}$-$Ba_{0.66}Sr_{0.34}CoO_{3-\delta}$ (PBSCF-b+BSC) electrode material 14
2.1.1.2 Previous $PrBa_{0.5}Sr_{0.5}Co_{1.5}Fe_{0.5}O_{6-\delta}$ (PBSCF-a) electrode material 14
2.1.1.3 Electrical conductivity relaxation (ECR) samples 15
2.1.1.4 Material slurry preparation 15
2.1.1.5 Structural characterization 16
2.1.2 SOC cell manufacturing and testing 16
2.1.2.1 SOC half-cell manufacturing 16
2.1.2.2 SOC single cell testing with PBSCF-b+BSC oxygen electrode 17
2.1.2.3 SOC single cell testing with previous PBSCF-a oxygen electrode 17
2.1.2.4 Hydrogen production cost calculation 17
2.1.2.5 Electrical conductivity relaxation (ECR) measurement 18
2.2 Design of highly efficient electrode with in situ exsolved Ni-Co alloy nanoparticles for CO_2 SOEC 19

2.2.1 Preparation of electrode materials and cell fabrication 19
2.2.1.1 Cathode material synthesis 19
2.2.1.2 Cathode ink preparation 19
2.2.1.3 Electrolyte-supported single cell fabrication 20
2.2.2 Structural and electrochemical Characterization 20
2.2.2.1 Structural and physicochemical properties characterization 20
2.2.2.2 Electrochemical characterization for CO_2 electrolysis 21
2.3 Design of high-performance reversible solid oxide cells for powering electric vehicles, long-term energy storage, and CO_2 conversion 22
2.3.1 preparation and testing of MS-SOCs 22
2.3.1.1 Air electrode material synthesis 22
2.3.1.2 Air electrode ink preparation 22
2.3.1.3 Preparation and testing of MS-SOCs 22
2.3.1.4 Structural characterizations 24
2.3.2 Calculation for the vehicle power systems comparison 24
2.3.2.1 Volumetric and gravimetric power densities of RSOC, battery, and internal combustor systems 24
2.3.2.2 Volumetric and gravimetric energy densities of RSOC, battery, and internal combustor systems 26
2.3.2.3 Charging/refueling time of RSOCEVs and comparison with BEVs and ICEVs.. 27
2.3.2.4 Fuel economy comparison of these three types of vehicles 28
2.3.2.5 Energy efficiency (EE) and electric power consumption (EPC) of CO_2 MS-SOECs 29
Chapter 3 - Boosting the performance of reversible solid oxide electrochemical cells with a novel hybrid oxygen electrode, $Pr_{1.39}Ba_{0.14}Sr_{0.53}Co_{1.48}Fe_{0.76}O_{6-\delta}$-$Ba_{0.66}Sr_{0.34}CoO_{3-\delta}$ 30
3.1 Hybrid oxygen electrode enables improved performance in both fuel cell and electrolysis modes 30
3.2 Structural properties of the in-situ formed hybrid electrode 35
3.3 Hybrid oxygen electrode enhances surface oxygen exchange coefficient and bulk oxygen-ion diffusion coefficient, leading to improved electrochemical performance. 43

3.4 SOECs equipped with the hybrid oxygen electrode achieve outstanding fuel cell performance. 54
3.5 Durability in fuel cell mode at intermediate operating temperatures 61
3.6 SOECs equipped with the hybrid oxygen electrode attain a current density of 4.4 A cm^{-2} at 1.3 V and 750 °C, and good durability during the accelerated stability testing 63
3.7 Conclusion 65
Chapter 4 - Tuning the *in situ* exsolution of Ni-Co alloy nanoparticles on doped ceria for improved performance in CO_2 electrolysis 67
4.1 Introduction to CO_2 SOECs 67
4.2 Structural characteristics of SDCNiCo15-30, SDCNi, and SDCCo 70
4.3 Tuning the Ni and Co doping percentage to achieve superior electrochemical performance. 79
4.4 Synergistic effects of NiCo alloy on CO_2RR activity enhancement. 83
4.5 Electrochemical performance of SDCNiCo25 in CO_2 SOEC and H_2 SOFC. 89
4.6 Conclusion 92
Chapter 5 - High-performance reversible solid oxide cells for powering electric vehicles, long-term energy storage, and CO_2 conversion 93
5.1 Metal-supported solid oxide cells 93
5.2 Reversible MS-SOC performance in H_2-H_2O 97
5.2 Stability and reversible operation of MS-SOCs 101
5.3 Employing reversible MS-SOCs to power vehicles 102
5.4 Reversible MS-SOC operation in CO-CO_2 106
5.5 CO_2 electrolysis comparison 111
5.6 Conclusion 116
Chapter 6 - Conclusion 117
Bibliography 120
Appendix A - Boosting the performance of reversible solid oxide electrochemical cells with a novel hybrid oxygen electrode, $Pr_{1.39}Ba_{0.14}Sr_{0.53}Co_{1.48}Fe_{0.76}O_{6-\delta}$-$Ba_{0.66}Sr_{0.34}CoO_{3-\delta}$-$Ba_{0.66}Sr_{0.34}CoO_{3-\delta}$ 129
Appendix B - Tuning the *in situ* exsolution of Ni-Co alloy nanoparticles on doped ceria for improved performance in CO_2 electrolysis 149

Appendix C - High-performance reversible solid oxide cells for powering electric vehicles, long-term energy storage, and CO_2 conversion 154

List of Figures

Figure 1. Schematic diagram of a solid oxide electrochemical cell. Reproduced with permission [10]. Copyright 2020, American Chemical Society. 2
Figure 2. Carbon-neutral cycle based on CO_2 electrolysis in SOECs. Reprinted with permission [32]. Copyright 2019, Wiley-VCH. 8
Figure 3. Schematic illustration of the SOEC with the newly developed hybrid electrode in fuel cell mode, which displays the oxygen reduction reaction. 31
Figure 4. The H_2 production cost as a function of H_2 production rate achieved in this work and reported in literature results [12,14–16,59,61,65–70]. 32
Figure 5. Performance comparison of YSZ-based SOECs in steam electrolysis mode, which indicates our SOECs equipped with the hybrid oxygen electrode achieve unprecedented performance (Table A1). 34
Figure 6. Comparison of peak power densities of our YSZ based SOEC in fuel cell mode with literature results (Table A2). 34
Figure 7. The XRD pattern and Rietveld refinement of as-synthesized hybrid electrode. 35
Figure 8. Bright-field TEM image of the hybrid electrode. 36
Figure 9. The SAED patterns collected from the area shown in Figure 9. 37
Figure 10. HAADF-STEM image and corresponding EDX elemental mapping images of the hybrid electrode. 38
Figure 11. HR-TEM images of PBSCF-b phase and BSC phase. 39
Figure 12. Overlay chemical mapping image with both Ba and Pr elements, which shows the Ba-rich area (magenta) is BSC and the Pr-rich area (green) is the PBSCF-b phase. 41
Figure 13. EDX spectra of the BSC phase and PBSCF-b phase (see the marked boxes in Fig 2F), which were used to quantify the stoichiometries of these two phases. 42
Figure 14. surface oxygen exchange coefficients (k_{chem}) for the hybrid electrode and previous PBSCF-a. 44
Figure 15. bulk oxygen-ion diffusion coefficient (D_{chem}) for the hybrid electrode and previous PBSCF-a. 45

Figure 16. Area-specific electrode polarization resistance (ASR_p) of SOECs equipped with the hybrid electrode and the previous PBSCF-a electrode, which were measured under OCV conditions. 47
Figure 17. Area-specific ohmic resistance (ASR_{ohm}) of SOECs equipped with the hybrid electrode and the previous PBSCF-a electrode, which were measured under OCV conditions. 48
Figure 18. Representative EIS comparison at 700 °C under 0.8 V. 50
Figure 19. DRT analysis of EIS data shown in Figure 19. 51
Figure 20. Temperature dependence of the partial polarization resistances of the electrode reactions of SOFCs with hybrid electrodes at 0.8 V. 52
Figure 21. Temperature dependence of the partial polarization resistances of the electrode reactions of SOFCs with previous PBSCF-a electrodes at 0.8 V. 53
Figure 22. I-V and I-P curves of the SOECs with the hybrid oxygen electrode at different operating temperatures. H_2 is fed to the fuel electrode as fuel. 55
Figure 23. I-V and I-P curves of the SOECs with the previous PBSCF-a oxygen electrode at different operating temperatures. H_2 is fed to the fuel electrode as fuel. 56
Figure 24. EIS spectra of the SOECs with two electrodes, which were collected at 0.8V, at temperatures of 700 °C and 600 °C, respectively. 57
Figure 25. Comparison of the SOEC peak power densities achieved with the hybrid oxygen electrode and previously developed PBSCF-a electrode. 58
Figure 26. I-V and I-P curves of the SOEC with the hybrid oxygen electrode. Humidified C_3H_8 was fed to the fuel electrode as fuel. 59
Figure 27. Comparison of our direct-C_3H_8 SOEC with literature results (Table A4). 60
Figure 28. Durability testing of the SOEC equipped with the hybrid oxygen electrode in fuel cell mode at a current density of 0.8 A cm^{-2} and temperature of 650 °C with 3% humidified H_2 fed to the fuel electrode. 61
Figure 29. Durability testing of the SOEC equipped with the hybrid oxygen electrode in fuel cell mode at a current density of 0.2 A cm^{-2} and temperature of 550 °C with 3% humidified H_2 fed to the fuel electrode 0.2 A cm^{-2} 62
Figure 30. Durability testing of the SOEC equipped with the hybrid oxygen electrode in fuel cell mode at a current density of 0.4 A cm^{-2} and temperature of 600 °C with 3% humidified C_3H_8 fed to the fuel electrode. 62

Figure 31. *I-V* curves of one representative SOEC with the hybrid oxygen electrode at different operating temperatures in steam electrolysis mode with 40% steam. 63
Figure 32. Durability testing of the SOEC at a current density of 0.8 A cm^{-2} and temperature of 650 °C in steam electrolysis mode with 40% steam. 64
Figure 33. Accelerated stability testing of the SOEC at a high current density of 3.0 A cm^{-2} and temperature of 650 °C in steam electrolysis mode with 40% steam. 64
Figure 34. Accelerated stability testing of the SOEC at a high current density of 5.0 A cm^{-2} and temperature of 750 °C in steam electrolysis mode with 40% steam. 64
Figure 35. XRD patterns of SDCNiCo15-30 before and after reduction treatment under 15% H_2/Ar at 650 °C for 2 h. 71
Figure 36. XRD patterns of SDCNiCo25, SDCNi, and SDCCo before and after reduction treatment under 15% H_2/Ar at 650 °C for 2 h. 71
Figure 37. TEM image and elemental maps of SDCNiCo25 sample after reduction. 72
Figure 38. HR-TEM images of SDCNiCo25 sample after reduction. 73
Figure 39. Quantitative analysis of the elemental ratios of three points where the NiCo alloy presents. 74
Figure 40. H_2-TPR curves of the SDCNiCo15-30 samples. 76
Figure 41. H_2-TPR curves of the SDCNiCo25, SDCNi, and SDCCo samples. 77
Figure 42. CO_2-TPD curves of the SDCNiCo25, SDCNi, and SDCCo samples. 78
Figure 43. I-V curves of SDCNiCo15-30 at 750 °C. 81
Figure 44. Current densities of SDCNiCo15-30 at 1.5 V, 750-650 °C. 81
Figure 45. Nyquist plots at 750 °C, OCV condition, with ASR_o subtracted. 82
Figure 46. Arrhenius plots for ASR_p of SDCNiCo15-30. 82
Figure 47. I-V curves of SDCNiCo25, SDCNi25, and SDCCo25 at 750 °C. 84
Figure 48. Current densities of SDCNiCo25, SDCNi25, and SDCCo25 at 1.5 V, 750-650 °C. 85
Figure 49. Arrhenius plots for ASR_p at 1.5 V at 750 °C, 1.5 V of SDCNiCo25, SDCNi25, and SDCCo25. 86
Figure 50. DRT plots at 750 °C, 1.5 V of SDCNiCo25, SDCNi25, and SDCCo25. 87
Figure 51. I-V-P curves and corresponding Nyquist plots under OCV of SDCNiCo25 in dry hydrogen under SOFC mode. 90

Figure 52. I-V curves and corresponding Nyquist plots at 1.5 V of SDCNiCo25 in CO_2/CO = 90/10 under SOEC mode. 91
Figure 53. Schematic illustration of the future energy system that relies heavily on RSOC technology. Illustration of RSOCs incorporated into the renewable energy system and further integration with RSOCEV technologies. 96
Figure 54. I-V curves in EC mode and I-V-P curves in FC mode at different operating temperatures. H_2O/H_2 = 40/60, and H_2O/H_2 = 3/97 gas mixture were fed to the fuel electrode for EC and FC testing, respectively. 99
Figure 55. EIS spectra collected under OCV condition in 3% humidified H_2. 100
Figure 56. Round-trip efficiency at different operating temperatures and the corresponding charging current densities and running time of the RSOCEV. The charging time is set at 12 minutes, the charging voltage for single cell at 1.3 V, and the average power output of RSOCEV at 40 kW across the operating temperature range. 100
Figure 57. Reversible MS-SOC operation with feeding 60 vol. % H2 and 40 vol. % H2O to the fuel electrode and air electrode exposed to the ambient air. (A) Discharging at a current density of 250 mA cm-2 for 2 hours and charging at a current density of 500 mA cm-2 for 1 hour in each cycle. The operating temperature is 550 °C. (B) Discharging at a current density of 250 mA cm-2 for 2 hours and charging at a current density of 500 mA cm-2 for 1 hour in each cycle. The operating temperature is 600 °C. 101
Figure 58 Comparison between ICEV, BEV and RSOCEV. (A) Gravimetric power densities. (B) Volumetric power densities. (C) Gravimetric energy densities. (D) Volumetric energy densities. (E) Refueling/Charging time. (F) Fuel economy. 105
Figure 59. I-V curves in EC mode and I-V-P curves in FC mode at different operating temperatures. CO/CO_2 = 10/90, and CO/H_2O= 97/3 gas mixture were fed to the fuel electrode for EC and FC testing, respectively. 107
Figure 60. SOEC EIS spectra collected under OCV condition in CO/CO_2 = 10/90, and SOFC EIS spectra collected under OCV condition in CO/H_2O= 97/3. 108
Figure 61. CO_2 electrolysis stability testing under a current density of 2000 mA cm^{-2} at 700 °C, and under a current density of 600 mA cm^{-2} at 600 °C. 110

Figure 62. Comparisons of our CO_2 SOEC with other electrolysis technologies regarding their energy efficiencies. The details of low-temperature electrolysis references are in Table S6. 112
Figure 63. Comparisons of our CO_2 SOEC with other electrolysis technologies regarding electric power consumption. The details of low-temperature electrolysis references are in Table S6. 113
Figure 64. Comparison of the current density of our SOEC with other state-of-the-art SOECs at 750 °C and 1.5 V..... 115

List of Tables

Table 1. Parameters for the RSOCEV stack derived from the MS-SOC experimental results. ... 25
Table 2. Parameters for calculating power and energy densities. ... 27
Table 3. Parameters for comparing the charging/refueling time of ICEVs, BEVs, and RSOCEVs ... 28
Table 4. Calculated kWh per 100 miles of ICEVs, BEVs, and RSOCEVs ... 29

Acknowledgements

I would like to express my gratitude to my advisor, Dr. Duan for his invaluable patience and mentoring. I am also grateful to my committee members, Dr. Anthony, Dr. Liu, and Dr. Munoz, for their support and advice.

And I cannot thank my parents and family enough for their support and encouragement. To my friends, thank you for the laughter over the years.

Chapter 1 - Introduction

1.1 Solid oxide electrochemical cells

1.1.1 Introduction to SOCs

The growing concern over global greenhouse effects and climate change has led to a surge in demands for clean and sustainable energy across the globe. This has generated significant interest in highly efficient energy technologies that produce considerably less greenhouse gas emissions. Among such technologies, SOCs have emerged as a promising option for next-generation electrochemical energy conversion and storage system, due to their exceptional efficiency and minimal environmental impact. Solid oxide cells are devices that operate at high temperatures and serve a dual purpose. They function as solid oxide fuel cells (SOFCs) to convert fuels such as hydrogen, natural gas, and other hydrocarbons into electricity with remarkable efficiency. Additionally, they can operate as solid oxide electrolysis cells (SOECs) to generate hydrogen, carbon monoxide, or syngas, contingent upon the composition of the input gases, as illustrated in Figure 1 [1,2].

Compared to traditional combustion technology, SOCs are a highly efficient option for generating electrical power in fuel cell mode, which have a significant advantage in terms of fuel flexibility, as they can operate on a variety of fuels such as hydrogen, methanol, ethanol, natural gas, and hydrocarbons, making it particularly well-suited for implementation in stationary applications and distributed power supply systems with high scalability. When operating in fuel production mode, SOCs can efficiently convert electrical energy into chemical energy, through a reversible operation of SOFC, which is especially useful in converting electrical energy from intermittent renewable energy sources such as solar PV panels and wind turbines. By applying an external electrical load, SOECs can split water and/or carbon dioxide to yield hydrogen and/or

carbon monoxide. Due to their high-temperature operation, the electrical energy required for SOECs can be much lower than that of low-temperature alkaline and polymer electrolyte membrane (PEM) electrolyzers [3–5]. Therefore, SOECs are promising technologies for efficient and cost-effective fuel production. If operated at thermoneutral voltage, SOECs are the most efficient type of electrolysis technology and can achieve very high conversion efficiencies of electrical-to-chemical energy, particularly when supplemented with additional thermal energy [6–8]. The roundtrip efficiency of SOCs used for electricity generation and fuel production can reach as high as approximately 65% in lab scale [9]. The unique characteristics of SOCs make them an essential component of our future energy system.

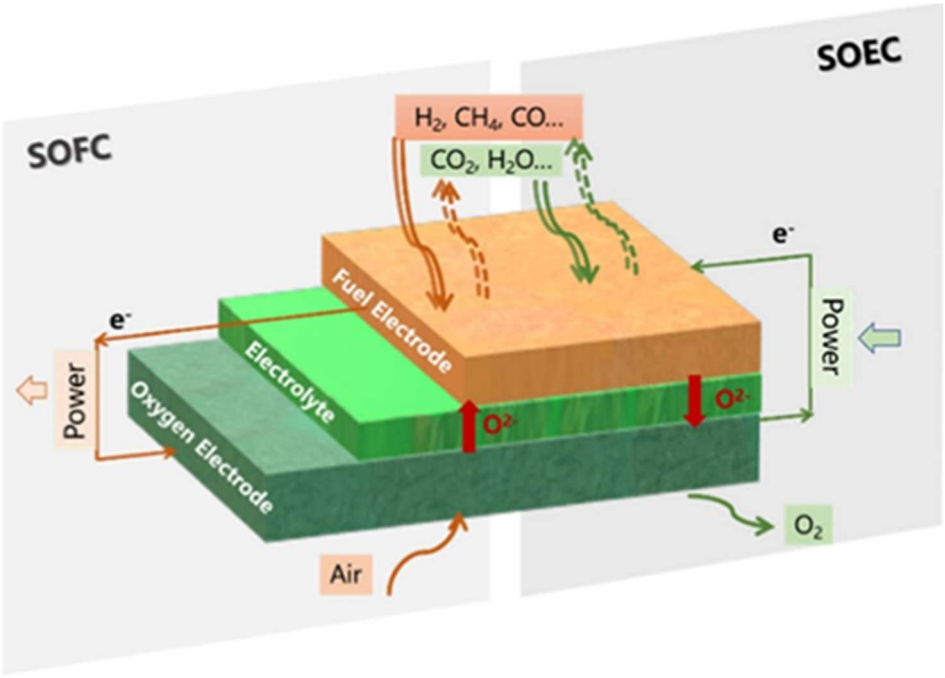

Figure 1. Schematic diagram of a solid oxide electrochemical cell. Reproduced with permission [10]. Copyright 2020, American Chemical Society.

SOCs are made up of three basic components: a porous fuel electrode, a porous air electrode, and a dense electrolyte. In principle, SOCs with oxygen-ion-conducting or proton-conducting electrolytes are referred to as O-SOCs or H-SOCs, respectively. When O-SOCs are operating in SOFC mode, H_2 is oxidized by O^{2-} at the anode side, releasing two electrons which are then transported via the external circuit. Meanwhile, O_2 is adsorbed, dissociated, and reduced to O^{2-} at the cathode side. The difference in oxygen partial pressure between the cathode an anode drives O^{2-} towards the anode through the oxide conducting electrolyte and produce H_2O [11]. This charge-carrier transport circuit generates electricity output and the reaction occur at the cathode and anode sides under SOFC mode can be written as follows:

H_2 oxidation at anode:

$$H_2 + O^{2-} \rightarrow H_2O + 2e^- \tag{1.1}$$

O_2 reduction at cathode:

$$\frac{1}{2}O_2 + 2e^- \rightarrow O^{2-} \tag{1.2}$$

Overall reaction:

$$H_2 + \frac{1}{2}O_2 \rightarrow H_2O \tag{1.3}$$

And in SOEC operating mode, external power sources provide electrons at the cathode side (fuel electrode side), which then electrochemically splits H_2O into H_2 and O^{2-}. The O^{2-} ions then diffuse through the dense electrolyte to reach the anode side (air electrode side), releasing O_2. This type of operation is also referred to as high-temperature steam electrolysis and the reactions occur at the cathode and anode sides can be written as follows:

H_2O reduction at cathode:

$$H_2O + 2e^- \rightarrow H_2 + O^{2-} \tag{1.4}$$

O_2 oxidation at anode:

$$O^{2-} \rightarrow \frac{1}{2}O_2 + 2e^- \quad (1.5)$$

Overall reaction:

$$H_2O \rightarrow H_2 + \frac{1}{2}O_2 \quad (1.6)$$

1.1.2 Current challenges

The commercial success of SOCs depends mainly on their capital and operating costs, lifespan, and stability. Ideally, the preferred materials should meet both performance and stability requirements, but this is challenging to achieve. SOC technology has undergone drastic improvements over the past decade, but for its commercialization, further research and development are needed to decrease the operating temperature without sacrificing much performance. The current state-of-the-art SOC materials are mainly limited to Ni-based cermet fuel electrodes like Ni-YSZ, one of the most common electrolytes for SOCs due to its negligible electrical conductivity, high ionic conductivity and high mechanical strength; perovskite-based oxide air electrodes such as Lanthanum strontium manganite (LSM), cobalt doped lanthanum ferrite perovskites, double perovskites, and ABO_3 type lanthanum nickelates; and zirconia-based electrolytes such as YSZ and ScSZ [12–14]. Despite the considerable advancements in the electrolyte and electrode material development, it is still necessary to conduct additional evaluations and the investigation of degradation mechanisms in both fuel and air electrode compartments. The notoriously sluggish ORR and OER in the oxygen electrode inevitably increase the area-specific resistance (ASR) of cells at reduced temperatures because of their thermally activated nature [15]. Therefore, significant amounts of effort have been put into developing positive electrode materials to alleviate the restricted electrochemical activity and decreased performance.

Achieving long-term stability is a major challenge that involves addressing fundamental issues related to the device's performance and degradation, including the chemical and physical stability of materials, microstructural stability, and the impact of various impurities present in fuels and air streams, as well as those that may come from stack components like stainless steel interconnect or glass-ceramic sealants. The microstructure of electrodes and the interface between the electrode and electrolyte in SOCs undergoes continuous evolution during operation of charging/discharging polarization at high temperatures [16–18]. The change in microstructure at the electrode/electrolyte interface is inherently linked to segregation/migration of cations like Sr, and the interaction with various species from the electrolyte, gas flow components, or SOC stack components [19,20].

It has been established that cobalt based mixed ion-electron conductors (MIECs) react with the YSZ electrolyte forming insulating phases such as $La_2Zr_2O_7$ and $SrZrO_3$. Thus, a doped ceria barrier layer, which is chemically compatible with cobalt based MIECs is usually employed between the positive electrode and YSZ electrolyte [21,22]. But this could be another stumbling block for the commercialization of the SOCs and development of an economical and efficient electrode material that is compatible is urgently needed.

1.1.3 Potential approaches

The enhancement of SOCs performance greatly depends on the modification of electrodes, which involves the careful design and construction of intricate electrode and electrode/electrolyte interface architecture. This modification can significantly improve the electrochemical activity and structural stability of an electrode material. One commonly used example is infiltration method. The process of infiltration or impregnation involves introducing a

functional phase into the backbone of an air/fuel electrode. To begin the process, the electrode backbone is first pre-sintered with adequate porosity on the electrolyte. A solution containing the active electrode phase precursor is then injected into the backbone using a syringe with controlled loading. After a moderate temperature calcination, the electrode particles form and bond to the backbone material at a nanoscale level. The loading can be further increased by repeating the infiltration process. For instance, Lu et al. [23] successfully increased the electrochemical oxidation activity of an anode-supported SOFC by infiltrating CeO_2 and Ni nanoparticles into the $La_{0.2}Sr_{0.25}Ca_{0.45}TiO_3$ (LSCT) backbone which led to a significant improvement in peak power density of 0.96 Wcm^{-2} at 800°C in H_2. However, the infiltration technique is not without its drawbacks. As the infiltrated electrode nanoparticles are not sintered at high temperatures, they cannot firmly bond with the backbone. Consequently, during long-term SOC operation, these infiltrated nanoparticles may migrate and coalesce, leading to cell performance degradation. Additionally, the infiltrated phase tends to reduce the porosity of the pre-sintered backbones, thereby limiting the loading of the infiltrated phase. Furthermore, in order to fabricate effective nanostructured electrode, many repeated infiltration/annealing cycles in the wet infiltration process are required and it may not be feasible for scale-up and commercial applications.

Another approach of modification of the electrodes is by in situ exsolution, which refers to a phenomenon that nanoparticles precipitate locally from the perovskite backbone surface after reduction. The nanoparticles that are exsolved typically consist of reducible transition and noble metals (such as Ni, Fe, Co, and Pt) that were previously doped into the backbone lattice. These nanoparticles exhibit high activity and are resistant to agglomeration and carbon deposition due to their socketed interface structure with the backbone material. However, this

application lacks diversity due to the limitation of reducible cation species and the requirement of reducing conditions makes it difficult for the application to the air electrodes [24]. Other novel processing methods such as pulsed laser deposition, sputtering, and freeze-casting, also are limited by high costs, complex procedures, and scale-up issues [25–27].

The double perovskite material, PBSCF and its related materials has been investigated as a promising air electrode for SOCs. For SOFC application, Chen et al. [28] reported an in-situ assembled PBSCF-GDC composite cathode achieving a peak power density (PPD) of 1.37 W cm^{-2} at 750 °C. And Tian et al. [29] utilized pure PBSCF as the air electrode for SOEC and achieved 1.74 A cm^{-2} at 2 V at 800 °C with relatively stable performance. Moreover, using infiltration method, Zhang et al. [30] reported that PBSCF infiltrated YSZ scaffold showed a low polarization resistance of 0.03 Ω cm^2 with stable charging performance at 700 °C for 600 h.

More efforts should be made to develop multi-phase electrodes from more efficient and facile fabrication methods. A nanostructured multi-phase positive electrode was fabricated by Chen et al. [31] via combination of $Gd_{0.2}Ce_{0.8}O_{1.9}$ (GDC) decorated $PrBa_{0.8}Ca_{0.2}Co_2O_{5+\delta}$ (PBCC) and direct assembly approach without the conventional sintering process. SOCs with such electrodes achieve PPD of 1.74 W cm^{-2} at 750 °C and current density of 1.77 A cm^{-2} at 1.3 V with stable performance. In a similar manner, Liu et al. [11] designed an $Er_{0.4}Bi_{1.6}O_{3-\delta}$ (ESB) functionalized $La_{0.8}Sr_{0.2}MnO_{3-\delta}$ (LSM) positive electrode via a co-synthesis modified Pechini method. Single cell testing with such an electrode revealed that performance in both fuel cell and electrolysis modes are improved compared to that of the mechanically mixed LSM-ESB electrode.

1.2 CO_2 electrolysis in solid oxide electrolysis cells (SOECs)

1.2.1 Introduction to CO_2 SOEC

Since the "Industrial Revolution" the atmospheric CO_2 concentration has drastically increased because of the enormous growth in the consumption of fossil fuels, which contributes to the global warming. Among various strategies to reduce the atmospheric CO_2 concentration, CO production through SOECs show unrivaled advantages because the high operating temperature enables effectively breaking of the bottleneck of slow reaction kinetics. Thus, CO_2 electrolysis in SOECs is the key step to close the carbon-neutral cycle, as shown in Figure 2 [32,33].

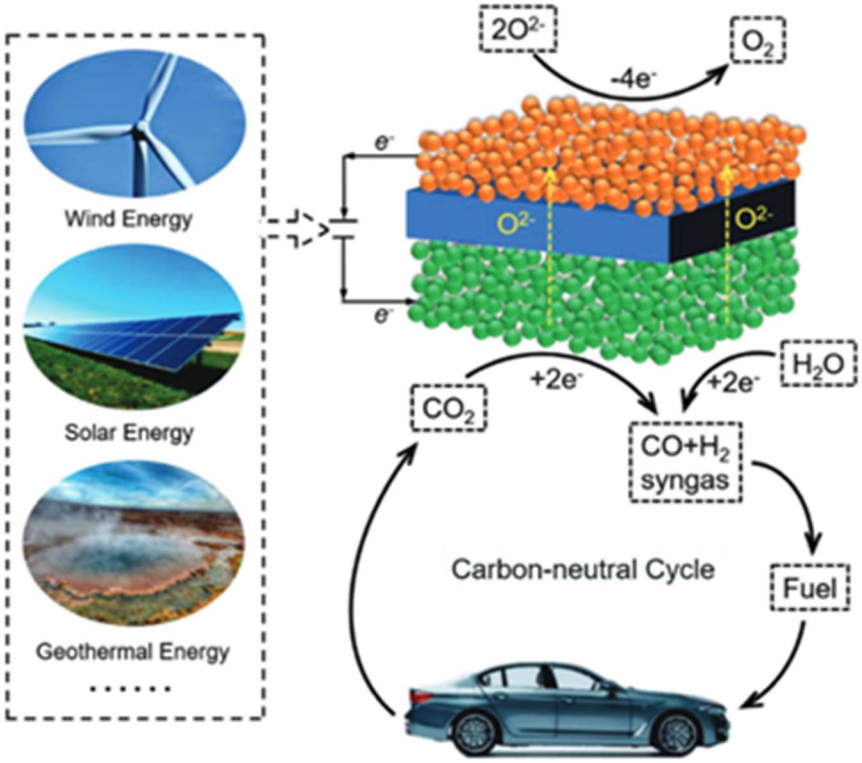

Figure 2. Carbon-neutral cycle based on CO_2 electrolysis in SOECs. Reprinted with permission [32]. Copyright 2019, Wiley-VCH.

Similar to steam electrolysis SOEC in the previous section, a SOEC for the electrochemical reduction of CO_2 also has three components: an anode for the oxidation reaction, a cathode for the reduction reaction, and in the middle an electrolyte for the transport of the ions and preventing the crossover of the gas at the electrodes. The oxygen vacancies in the solid electrolyte of SOECs allow conduction of oxygen ions, and CO_2 molecules at cathode receive electrons to produce CO and oxygen ions, as demonstrated in Equation 7. The produced oxygen ions transport through the dense electrolyte to the anode and generate oxygen molecules by losing electrons (Equation 8). In a SOEC, the reactions occurring on the anode and cathode take place at the triple phase boundaries (TPB), which consist of oxygen ionic conductors or protonic conductors, electronic conductors, and the reactant gases. Thus, the electrochemical reduction of CO_2 is not limited by the mass transport of CO_2. This means that the current density of SOECs is significantly higher compared to the electrochemical reduction of CO_2 in aqueous electrolytes. Furthermore, the easy activation of CO_2 at elevated temperatures also contributes to the high current density. However, it should be noted that the major carbon-containing product generated from this process is CO, while carbon and methane are produced as by-products [34–36].

$$CO_2 + 2e^- = CO + O^{2-} \quad (1.7)$$

$$O^{2-} = 1/2O_2 + 2e^- \quad (1.8)$$

The electrolyte in a SOEC must exhibit high oxygen ionic or protonic conductivity and low electronic conductivity, while also remaining stable in varying redox conditions and CO_2/steam atmospheres. Additionally, the electrolyte should be readily fabricated into a dense, and sturdy film to prevent gas mixing at the anode and cathode. Many efforts have been made by researchers to develop materials that fulfill the above requirements, resulting in the availability of various types of materials that can be used as electrolytes for SOECs. Examples of such materials include zirconia-based oxides, ceria-based oxides, lanthanum gallates-based oxides,

bismuth-based oxides, and others. Perovskite oxides based on lanthanum gallates (ABO_3) exhibit high oxygen ionic conductivity when doped with Sr in the La (A) sites and Mg in the Ga (B) sites, respectively, leading to the formation of $La_{1-x}Sr_xGa_{1-y}Mg_yO_{3-\delta}$ (LSGM), which has an oxygen ionic conductivity of 0.15 S cm^{-1} at 1073 K [37,38]. This high level of conductivity is comparable to that of ceria-based oxygen ionic conductors and significantly higher than that of YSZ. However, LSGM has a tendency to react with NiO, resulting in the formation of the $LaNiO_3$ phase. This reaction leads to the instability of lanthanum gallate-based electrolytes, which in turn causes a significant increase in electronic conductivity and electrode overpotential. To prevent the interdiffusion of La and Ni components between the electrolyte and electrode layers, barrier interlayers such as La_2O_3-doped ceria are utilized. These interlayers effectively block the diffusion of these components and enhance the stability of the electrolyte.

1.2.2 Current challenges

One of the most major challenges associated with CO_2 SOEC is its high operating temperature (>700 °C) for efficient electrochemical conversion. Although the high temperature can greatly accelerate the electrode reaction and lead to a higher current density than that of electrolysis cells using liquid electrolyte, it can also lead to thermal stress, reducing the lifespan of the materials, and increasing the overall cost of the system.

The remarkably stable double bonds in CO_2 also poses the requirement of efficient catalysts to facilitate the electrochemical conversion of CO_2. Specifically, SOEC cathode should possess high catalytic activity for CO_2 electroreduction while maintaining excellent electronic and ionic conductivity, chemical and mechanical stability and proper compatibility with the

electrolyte. Several methods enhancing the electrocatalytic activity of the cathode materials have been developed, such as doping, infiltration, and in situ exsolution.

The CO_2 SOEC operates in a harsh environment with high temperatures, high pressure, and reactive gases. Therefore, the cell degradation is another major challenge for the practical usage of CO_2 SOECs. Some of the common degradation issues for electrodes include agglomeration, carbon deposition, poisoning and decomposition. The state-of-the-art Ni-YSZ cathode could easily be deactivated by re-oxidation or carbon formation in the atmosphere of CO/CO_2, besides the inevitable Ni agglomeration during the charging test due to the thermally induced growth of Ni particles at high temperature.

Reducing electricity consumption is crucial for the widespread implementation of SOEC, as it is the primary cost driver for this technology, based on the assessment of its economic efficiency. Thus, the economic competitiveness of SOEC can be improved by developing high-performance and stable designs, which can achieve a specific current density at a lower overpotential or temperature. This is crucial because such SOECs can help avoid performance degradation and minimize electricity consumption.

1.2.3 Recent developments of cathode materials

For cathodes used in SOEC, it is essential to have high ionic and electronic conductivity, as well as good stability under high-temperature atmospheres containing concentrated CO_2 and steam. Additionally, the cathodes should exhibit excellent catalytic activity, good porosity, and compatibility with electrolyte materials. Typically, cathodes used in SOECs are metal-ceramics (cermet) such as Ni-YSZ, where Ni facilitates electronic transport and YSZ acts as the electrolyte material for ionic diffusion. Alternative cathode materials, like perovskite-typed

MIECs with high catalytic activity, durability and electrical conductivity have been investigated, such as $Sr_2Fe_{1.5}Mo_{0.5}O_{6-\delta}$ (SFM), $(La,Sr)FeO_{3-\delta}$ (LSF), $(La,Sr)TiO_{3-\delta}$ (LST), and $(La,Sr)(Cr,Mn)O_{3-\delta}$ (LSCM). LSCM exhibits good performance with low ASR at 800 °C. For example. Yue et al. conducted a study on the feasibility of using LSCM/GDC as a composite cathode for an electrolysis cell with YSZ as the electrolyte and $La_{0.8}Sr_{0.2}MnO_3$/ScSZ as the anode. The study aimed to determine whether LSCM could serve as the cathode for CO_2 electrolysis and H_2O-CO_2 co-electrolysis at 800 °C. The results showed that when the feed gas was a CO_2/CO mixture (70/30; total flow rate: 20 sccm), the CO production rate exceeded 1.2 μmol/(cm•s) at ~1.9 V with 96% FE. However, LSCM exhibits much lower electrical conductivity in a reducing atmosphere, measuring only 1.5 S/cm in 5% H_2 and insufficient catalytic activity compared to conventional cermet. To address these issues, high electronic conducting phases are often added to LSCM electrodes. Xing et al. developed a Cu-impregnated LSCM cathode and discovered that this composite cathode displayed lower ohmic resistance and better electrochemical performance than the electrolysis cell without Cu impregnation, as evidenced by EIS and I-V curves under the same conditions. For the electrolysis cell using the Cu-impregnated cathode, the maximum current density increased from 1.31 A cm^{-2} with a feed gas of 50% H_2O-50% H_2 to 1.82 A cm^{-2} with a feed gas of 50% H_2O-12.5% H_2-37.5% CO_2 under an applied electrolysis voltage of 1.65 V and a temperature of 800 °C. During a long-term SOEC test, the applied electrolysis voltage slowly increased by only 2% over 50 hours under a constant current density of 0.33 A/cm^2 with a feed mixture of 50% H_2O-25% H_2-25% CO_2 at 800 °C.

One approach to improve electrocatalytic activity is the exsolution of metallic nanoparticles by rationally design of the perovskite ceramic electrodes. Usually, transition metals

which could be easily reduced, such as Fe, Co, Ni, Pd and Ru are chosen and exsolved through reduction with H_2. The exsolved nanoparticles could increase the CO_2 adsorption capability and thus increase the electrolysis current density. Similarly, Co-Fe alloy nanoparticles formed on Co doped SFM electrode shows higher current density of 1.05 A cm^{-2} compared to SFM electrode. Another strategy reported by Lv et al. highlights repeated redox manipulations, which produce uniformly exsolved Ru-Fe alloy nanoparticles from Ru doped SFM. The performance can also be improved by engineering the compositions of the electrode, such as addition of a second phase oxygen-ion conductor like SDC, which is beneficial for the surface reaction and bulk diffusion, usage of a porous YSZ scaffold for infiltration of nanoarchitecture SFM.

Ceria and doped ceria have cubic fluorite phases, which are found to be structurally stable throughout the operating temperature range of SOECs in a mixed CO-CO_2 atmosphere, demonstrating good resistance to carbon deposition. Ceria is a practically pure oxygen-ion conductor in an oxidative environment, but it is MIEC in a reductive environment like the cathode of an SOEC. The partial reduction of Ce^{4+} to Ce^{3+} and rapid conversion of Ce^{3+}/Ce^{4+} make ceria and doped ceria suitable SOEC cathode material. Moreover, the carbon formation on the SDC is suppressed via the Boudouard reaction by the production of carbonate species.

Chapter 2 - Materials and Methods

2.1 Design of high-performance SOCs with a novel hybrid oxygen electrode

2.1.1 Material synthesis and characterization

2.1.1.1 $Pr_{1.39}Ba_{0.14}Sr_{0.53}Co_{1.48}Fe_{0.76}O_{6-\delta}$-$Ba_{0.66}Sr_{0.34}CoO_{3-\delta}$ (PBSCF-b+BSC) electrode material

The PBSCF-b+BSC oxygen electrode material was synthesized using the wet-chemistry method, in which high-purity precursors, $Ba(NO_3)_2$, $Sr(NO_3)_2$, $Co(NO_3)\bullet 6H_2O$, and $Fe(NO_3)_3\bullet 6H_2O$ (Fisher Scientific) were dissolved in deionized water in stoichiometric amounts. Additionally, a specific amount of Pr_6O_{11} (Fisher Scientific) was dissolved in diluted nitric acid and subsequently added into the above solution. Then the complexing and chelating agents, ethylenediaminetetraacetic acid (EDTA) (Fisher Scientific) and citric acid (CA) (Fisher Scientific) were added to above solution in appropriate amounts, with a molar ratio of 2:2:1 (EDTA: CA: total metal ions). After continuous stirring for one hour at room temperature, ammonium hydroxide solution was added into the solution to adjust the pH to ~9. The resulting solution was heated to 300 °C on a hot plate with continuous stirring until a gel was formed. This gel was then dried in an oven at 175 °C overnight, and the resulting black powder was calcined at 650 °C under air for 5 hours, followed by ball-milling in ethanol for 24 hours and drying at 175 °C to obtain the final powder for the oxygen electrode ink. After sintering at 750-770 °C, the calcined powder was crystallized to the PBSCF-b+BSC hybrid electrode material.

2.1.1.2 Previous $PrBa_{0.5}Sr_{0.5}Co_{1.5}Fe_{0.5}O_{6-\delta}$ (PBSCF-a) electrode material

The previous PBSCF-a electrode powder was also synthesized via the wet-chemistry method described above. However, the powder obtained after calcination at 650 °C was later sintered at 900 °C and crystallized to the previous PBSCF-a.

2.1.1.3 Electrical conductivity relaxation (ECR) samples

The synthesis processes for ECR materials, namely, $Pr_{1.39}Ba_{0.14}Sr_{0.53}Co_{1.48}Fe_{0.76}O_{6-\delta}$, $Ba_{0.66}Sr_{0.34}CoO_{3-\delta}$, and previous $PrBa_{0.5}Sr_{0.5}Co_{1.5}Fe_{0.5}O_{6-\delta}$ were the same as the above wet-chemistry method. Briefly, stoichiometric amounts of $Ba(NO_3)_2$, $Sr(NO_3)_2$, and $Co(NO_3)\bullet 6H_2O$ were used as precursors for BSC powder synthesis. The hybrid electrode, PBSCF-b+BSC is formed at 750-770 °C, while the preparation of a dense PBSCF-b+BSC bar requires a sintering temperature higher than 900 °C. Therefore, a PBSCF-b dense bar was fabricated and then coated with BSC slurry.

2.1.1.4 Material slurry preparation

Oxygen electrodes slurries

10 g of PBSCF-b+BSC or previous PBSCF-a powder, 2 g dispersant (20 wt.% solsperse 28000 (Lubrizol) dissolved in α-terpinol), and 1 g binder (5 wt.% V-006 (Heraeus) dissolved in α-terpinol) were mixed and ground by mortar and pestle for 0.5 h to obtain the oxygen electrodes slurries.

BSC slurry for ECR testing

Similarly, appropriate amounts of BSC powder were mixed with dispersant and binder, then ground well by mortar and pestle for preparation of the BSC slurry.

Fuel electrode slurry

The composite powder, which consisted of 40 wt.% yttria-stabilized zirconia (YSZ) (TZ-8Y, Tosoh), 60 wt.% NiO (Sigma Aldrich), and 20 wt.% corn starch (Sigma Aldrich), was mixed with menhaden fish oil, b-98 polyvinyl butyral, polyethylene glycol 400, cyclohexanone, di-n-butyl phthalate, xylenes, and ethanol, and then ball-milled using YSZ beads (diameter = 10 mm) for 24 h to obtain the fuel electrode slurry.

Electrolyte slurry

Similarly, the electrolyte slurry was also prepared by mixing and ball-milling YSZ powder and the above organic materials and ethanol.

2.1.1.5 Structural characterization

The crystal structures of the hybrid electrode and previous PBSCF-a were determined by using X-ray diffraction (XRD) (Rigaku MiniFlex diffractometer) with a Cu K-alpha radiation source operated at 15 mA and 30 kV and a scanning rate of 1 degree per minute. The Rietveld refinement was further performed via the GSAS program to probe detailed crystal structural information of the PBSCF-b+BSC material. The morphological and cross-sectional properties of the single cells were characterized by scanning electron microscopy (SEM, Hitachi/S-3400 N). Transmission electron microscopy (S/TEM, FEI Talos F200X, Thermo Fisher Scientific) operated at 200 kV was employed to obtain the morphological, and structural information about the oxygen electrode materials, with EDX detectors were utilized for chemical composition characterization.

2.1.2 SOC cell manufacturing and testing

2.1.2.1 SOC half-cell manufacturing

The fuel electrode-supported half-cells of YSZ-NiO were fabricated through a tape-casting process. The prepared fuel electrode slurry was first coated on Mylar via tape-casting and then dried in air for 5 h. The single-layer fuel electrode serves as both a functional layer and a support layer. The electrolyte slurry was then cast on the fuel electrode support layer. The resulting two layers were dried in air for 24 h, followed by sintering at 1350 °C for 5 h to fabricate the SOC half-cells.

2.1.2.2 SOC single cell testing with PBSCF-b+BSC oxygen electrode

The hybrid oxygen electrode slurry was first brush-painted on the YSZ electrolyte surface and then dried at 180 °C on a hot plate for 0.5 h. Gold paste was applied on both electrodes and so was a silver grid for current collection. The obtained single cells were directly sealed on an alumina tube with the MO·SCI glass sealant (OL-GL1709P/-45) without pre-sintering the oxygen electrode. The testing station temperature was increased to 765 °C with a heating rate of 4 °C/min, to melt the sealing glass while the PBSCF-b+BSC hybrid electrode was obtained simultaneously. Then the SOC single cell was tested at temperatures ranging from 750 °C to 550 °C. Ambient air (300 sccm) and humidified hydrogen (or propane) with a flow rate of 50 sccm, were fed to the oxygen and fuel electrodes, respectively. To evaluate the fuel cell performance, the hydrogen was flowed through a bubbler at room temperature, while for electrolysis evaluation, a boiler was used instead, to obtain a hydrogen flow with 40% humidity.

Prior to the electrochemical characterization, a mixture of H_2 and Ar gas flow (20 sccm) was fed to reduce the NiO to Ni at the fuel electrode. The electrochemical impedance spectroscopy (EIS) and I-V curve measurements were performed using Gamry Reference series potentiostat/galvanostat/ZRAs, including 1000, 3000 and 5000. EIS data was collected over a frequency range of 10 kHz – 0.1 Hz under open circuit conditions or applied voltage.

2.1.2.3 SOC single cell testing with previous PBSCF-a oxygen electrode

The previous PBSCF-a slurry was brush-painted on the YSZ electrolyte surface and then fired at 900 °C for 2 h to obtain the previous PBSCF-a oxygen electrode. The following single cell testing procedure was the same as mentioned above.

2.1.2.4 Hydrogen production cost calculation

The hydrogen production cost shown in Figure 1B was calculated according to the following equation:

$$Hydrogen\ production\ cost = \frac{V \times j \times 0.001 \times \$0.04/kW \cdot h}{j/(2 \times F \times 3600 \times M_{H_2})} \quad (2.1)$$

Where V is the voltage applied on the SOEC (V), j is the corresponding current density (A cm^{-2}), $\$0.04/kW \cdot h$ represents the unit electricity cost, F is the Faraday constant (96485 s A mol^{-1}), and M_{H_2} is the molecular weight of hydrogen (0.001 kg mol^{-1})

2.1.2.5 Electrical conductivity relaxation (ECR) measurement

ECR testing was utilized to evaluate the surface exchange kinetics of the hybrid electrode and previous PBSCF-a. The previous PBSCF-a powder was first axially pressed at 100 bar for 2 min using a die (diameter = 2 cm), then sintered at 900 °C for 3 h. The resulting dense pellets were cut by a high-precision diamond saw. PBSCF-b+BSC sample was also prepared in a similar manner. $Pr_{1.39}Ba_{0.14}Sr_{0.53}Co_{1.48}Fe_{0.76}O_{6-\delta}$ dense bars were obtained and BSC slurry was then coated on the surface. ECR measurements of these samples were conducted at temperatures ranging from 700 °C to 600 °C. In each measurement, the initial oxygen concentration was set as 2 vol.% (490 sccm Ar + 10 sccm O_2) and a current of 40 mA was applied. After the voltage reached equilibrium, the oxygen concentration was changed to 20 vol.% (400 sccm Ar + 100 sccm O_2) and the voltage response was recorded each time. The resulting data was analyzed using the NETL ECR analysis tool.

2.2 Design of highly efficient electrode with in situ exsolved Ni-Co alloy nanoparticles for CO_2 SOEC

2.2.1 Preparation of electrode materials and cell fabrication

2.2.1.1 Cathode material synthesis

A set of cathode materials, SDC doped with 15-30% Ni-Co (denoted as SDCNiCo15, SDCNiCo20, SDCNiCo25 and SDCNiCo30), where the doping percentages of Ni and Co are equivalent, SDC doped with 25% Ni (SDCNi25), and SDC doped with 25% Co (SDCCo25) were synthesized via the wet-chemistry method. Briefly, high-purity precursors, Sm(NO3)3·6H2O, Ce(NO3)3·6H2O, Ni(NO3)2·6H2O, and Co(NO3)2·6H2O (Fisher Scientific) were dissolved in deionized water in stoichiometric amounts at room temperature. Ethylenediaminetetraacetic acid (EDTA) (Fisher Scientific) and citric acid (CA) (Fisher Scientific) were added to the above solution as complexing and chelating agents in appropriate amounts (EDTA: CA: total metal ions = 2:2:1 (molar ratio)). After continuous stirring for approximately an hour at room temperature, ammonium hydroxide solution (Fisher Scientific) was added to adjust the pH to ~9. Then the solution was heated to 300 °C under continuous stirring until a gel was formed, which was transferred into an oven and dried at 175 °C overnight. The resulting black powder was calcined at 650 °C under air for 5 hours, followed by ball milling in ethanol for 24 hours and drying. At that time, the final powder for preparing the cathode ink was obtained.

2.2.1.2 Cathode ink preparation

Appropriate amounts of the above final powder were mixed with a dispersant solution (20 wt.% solsperse 28000 (Lubrizol) dissolved in α-terpinol), and a binder solution (5 wt.% V-006 (Heraeus) dissolved in α-terpinol), with a weight ratio of 10:2:1. The mixture were ground by mortar and pestle for 0.5 hour to obtain the cathode inks.

2.2.1.3 Electrolyte-supported single cell fabrication

The electrolyte material, $La_{0.80}Sr_{0.20}Ga_{0.80}Mg_{0.20}O_{3-x}$ (LSGM) powder, was purchased from Fuel Cell Materials company. LSGM powder was mixed with menhaden fish oil, b-98 polyvinyl butyral, polyethylene glycol 400, cyclohexanone, di-*n*-butylphthalate, xylenes, and ethanol. Then the mixture was ball milled using YSZ beads (diameter = 10 mm) for 24 hours. The obtained electrolyte slurry was coated on Mylar via tape-casting and then dried in air for 24 hours, followed by sintering at 1400 °C for 5 hours to obtain the electrolyte support half-cells.

The anode material adopted in this study, $Pr_{1.39}Ba_{0.14}Sr_{0.53}Co_{1.48}Fe_{0.76}O_{6-\delta}$-$Ba_{0.66}Sr_{0.34}CoO_{3-\delta}$ (PBSCF-b + BSC), was developed in our previous work [40,41]. And the anode ink was prepared in a similar manner mentioned above.

The cathode ink was first brush-painted on one side of the electrolyte half-cells, and then dried at 180 °C for 0.5 hour. After that, the half-cells were sintered at 1000 °C for 2 hours. Then the anode ink was applied on the other side of the electrolyte half-cells. Gold paste was applied on both electrodes and so was a silver grid for current collection.

2.2.2 Structural and electrochemical Characterization

2.2.2.1 Structural and physicochemical properties characterization

The crystal structures of the cathode materials before and after reduction were determined by X-ray diffraction (XRD) instrument (Rigaku MiniFlex II diffractometer) with a Cu K-α radiation source operated at 15 mA and 30 kV and the scanning rate is 1° per minute. Scanning electron microscopy (SEM) (Hitachi/S-3400 N) was employed to characterize the surface morphology and cross section properties of the SOECs. Transition electron microscopy (TEM)

(FEI Talos F200X) combined with EDX detectors was employed to reveal the crystalline structures and element distributions of the SDC with exsolved metallic phase samples.

H_2-temperature-programmed reduction (H_2-TPR) (ChemBET Pulsar) was carried out to probe the reducibility of samples. 0.1 g of the powder was loaded in a U-shaped quartz tube and pretreated with nitrogen flow (100 sccm) at 140 °C for 0.5 hour. Then the samples were cooled down to room temperature under nitrogen atmosphere, after which the gas was switched to H_2: N_2 = 15%: 85% with a flow rate of 100 sccm, and the TPR test was performed with a heating rate of 10 °C per minute. TG Analysis.

2.2.2.2 Electrochemical characterization for CO_2 electrolysis

The single cells were sealed on alumina tubes with the glass sealant from MO·SCI (OL-GL1709P/-45) and to melt the sealing glass and sinter the anode, the testing station was heated to 765 °C with a heating rate of 4 °C min^{-1}. The operating temperature for cell testing ranged from 750 °C to 600 °C. Before the electrochemical testing, hydrogen was fed to the cathode side with a flow rate of 50 sccm for reduction treatment. To evaluate the SOFC performance in H_2, the hydrogen flow rate was increased to 100 sccm on the fuel electrode side while the air electrode was exposed to ambient air (300 sccm). For CO_2 SOEC evaluation, the anode side was exposed to ambient air, while a mixture of CO/CO_2= 10/90 (flow rate = 100 sccm) was fed to the cathode. The electrochemical measurements were performed via Gamry Reference series potentiostat/galvanostat/ZRAs, including 1000, 3000 and 5000. Electrochemical impedance spectroscopy (EIS) data was collected over a frequency range of 10 kHz to 0.1 Hz under open circuit voltage (OCV) or applied voltage.

2.3 Design of high-performance reversible solid oxide cells for powering electric vehicles, long-term energy storage, and CO_2 conversion

2.3.1 preparation and testing of MS-SOCs

2.3.1.1 Air electrode material synthesis

A previously developed hybrid air electrode material, $Pr_{1.39}Ba_{0.14}Sr_{0.53}Co_{1.48}Fe_{0.76}O_{6-\delta}$+$Ba_{0.66}Sr_{0.34}CoO_{3-\delta}$ (PBSCF-b+BSC), was employed as the air electrode [40]. Briefly, a stoichiometric amount of Pr_6O_{11} (Fisher Scientific) was dissolved in diluted nitric acid and subsequently $Ba(NO_3)_2$, $Sr(NO_3)_2$, $Co(NO_3)$•$6H_2O$, and $Fe(NO_3)_3$•$6H_2O$ (Fisher Scientific) were then dissolved in the above solution. Ethylenediaminetetraacetic acid (EDTA) (Fisher Scientific) and citric acid (CA) (Fisher Scientific), acting as complexing and chelating agents, were then added to the solution in appropriate amounts, with a molar ratio of 2:2:1 (EDTA: CA: total metal ions). Through continuous stirring at room temperature for approximately one hour, ammonium hydroxide solution was added to adjust the pH of the solution to ~9 and a gel was formed after continuous stirring and heating at 300 °C. Afterward, the gel was dried in an oven at 175 °C for 12 hours, yielding a black powder, which was subsequently calcined at 650 °C under air for 5 hours. The obtained powder was ball milled in ethanol for 24 hours, followed by drying at 175 °C to obtain the final powder for preparing the air electrode ink.

2.3.1.2 Air electrode ink preparation

An appropriate amount of PBSCF-b+BSC powder was mixed with dispersant (20 wt.% solsperse 28000 (Lubrizol) dissolved in α-terpinol), and binder (5 wt.% V-006 (Heraeus) dissolved in α-terpinol), with a weight ratio of 10:2:1 and ground by mortar and pestle for 30 minutes to prepare the air electrode ink.

2.3.1.3 Preparation and testing of MS-SOCs

All MS-SOFC single cells tested in this study were produced by Nissan Motor Company. A porous Fe-Cr alloy serves as the metallic anode support, while the anode functional layer is composed of scandium and yttrium co-stabilized zirconia (ScYSZ) and NiO (40 wt. % ScYSZ + 60 wt. % NiO). The electrolyte employed is ScYSZ, with a thickness of approximately 8 μm. A barrier layer of gadolinia doped ceria (GDC), with a thickness of around 1 μm, was applied on the electrolyte.

The air electrode was painted on the electrolyte. Gold paste was employed as the current collector with silver grids applied to both electrodes to enhance the current collection. The cell was sealed onto an alumina tube using a glass sealant (MO SCIL 1709P/-45). The testing station's temperature was progressively raised to 765 °C with 80 vol. % H_2/ 20 vol. % N_2 fed to the anode. The cell was held at 765 °C for 5 minutes to seal the cell while sintering the cathode. Subsequently, the anode underwent further reduction at 750 °C for 30 min with 100 sccm H_2 fed to the anode. Afterwards, the SOEC fuel cell performance was tested at a temperature ranging from 750 °C to 550 °C. The air electrode was exposed to ambient air. In steam electrolysis mode, a mixture of 40 vol. % steam and 60 vol. % hydrogen was fed to the fuel electrode, while the air electrode was exposed to ambient air. The reversible operation under H_2/H_2O was conducted under the same condition with steam electrolysis.

On the other hand, a mixture of CO and CO_2 was fed to the fuel electrode to evaluate the performance under CO/CO_2.The $CO\text{-}CO_2$ gas mixture was flowed through a bubbler to obtain 3% humidity and then fed to the fuel electrode for fuel cell performance evaluation. To assess the impact of CO_2 dilution, the fuel cell was tested in pure CO (3% H_2O) and CO/CO_2 gas mixture (ratio = 50/50), respectively. And for CO_2 electrolysis testing, CO/CO_2 ratio was set as 10/90. The air electrode was exposed to ambient air during the testing.

In this work, electrochemical impedance spectroscopy (EIS) and I-V curves were collected utilizing the Gamry Reference series potentiostat/galvanostat/ZRAs.

2.3.1.4 Structural characterizations

The crystal structure of the PBSCF-b+BSC air electrode was determined by using X-ray diffraction (XRD) (Rigaku MiniFlex diffractometer) with a Cu K-alpha radiation source operated at 15 mA, 30 kV, and a scanning rate of 1 degree per minute. The morphological and cross-sectional properties of the MS-SOCs were characterized using the scanning electron microscope (SEM, Hitachi/S-3400 N).

2.3.2 Calculation for the vehicle power systems comparison

2.3.2.1 Volumetric and gravimetric power densities of RSOC, battery, and internal combustor systems

To evaluate the power system of RSOCEVs in comparison to those of ICEVs and BEVs, we focused on studying light-duty passenger vehicles. We analyzed and compared both the volumetric and gravimetric power densities and energy densities of these three types of power system. The specifics for RSOCEV stacks were derived from the MS-SOC experimental results acquired in this work. The MS-SOC stack comprises repeating units, consisting of two gas diffusion layers (i.e., current collector layers integrated with the gas flow channels), one MS-SOC, and one interconnect layer. Herein, considering the MS-SOCs are mainly composed of metallic anode, the interconnect layer's weight is equivalent to that of the MS-SOC layer. Additionally, the weight of two porous gas diffusion layers accounts for 10% of MS-SOC layer. Additionally, these four layers have identical thickness and volumes. With these assumptions, the stack density can be derived as follows:

$$\rho_{stack} = \frac{(\rho_{single\ cell} \times A \times \frac{t}{4}) \times 210\%}{A \times t} \quad (2.2)$$

Where ρ_{stack} is the density of the stack (g cm^{-3}), $\rho_{single\ cell}$ is the density of the MS-SOC cell layer (g cm^{-3}), A represents the area of each layer (cm^2), and t is the thickness of each unit which contains four layers (cm).

In an ideal scenario, we proceed under the assumption that scaling up from single cells to a stack does not compromise its performance in any way. The volumetric power density of the stack can then be calculated using equation (2):

$$P_{stack\_d} = \frac{P_{single\ cell} \times A}{A \times t} \quad (2.3)$$

Where P_{stack_d} is the volumetric power density of the stack in fuel cell mode (W cm^{-3}), and $P_{single\ cell}$ is the power density of the single cell (W cm^{-2}).

The details regarding the single cell parameters and the subsequent RSOCEV stack are summarized in Table 1.

Table 1. Parameters for the RSOCEV stack derived from the MS-SOC experimental results.

Single MS-SOC density (g cm^{-3})	2.59
Unit thickness (cm)	0.272
Stack density (g cm^{-3})	1.36
Single cell areal power density at 0.75 V, 750 °C (W cm^{-2})	1.28
Stack volumetric power density at 0.75 V, 750 °C (W cm^{-3})	4.71
Single cell areal power density at 0.62 V, 750 °C (W cm^{-2})	1.60

Stack volumetric power density at 0.62 V, 750 °C (W cm^{-3})	5.88

The input parameters for gravimetric and volumetric calculations of three simplified power systems are shown in Table 2. The BEV battery specifications were taken from 2021 Tesla Model S [42]. The hydrogen tank parameters for RSOCEV were borrowed from 2020 Toyota Mirai [43]. We assumed that the RSOCEV power output matches that of BEV to facilitate a straightforward comparison. We then proceed to compute the corresponding stack weight and volume.

$$V_{stack} = \frac{P_{total} \times 1000}{P_{stack\_d} \times 1000} \quad (2.4)$$

Where V_{stack} is the volume of the stack (L), P_{total} represents the total power of the RSOCEV stack (kW).

2.3.2.2 Volumetric and gravimetric energy densities of RSOC, battery, and internal combustor systems

In comparing energy densities, we made the assumption that the maximum energy output of RSOCEV equals that of BEV. Additionally, we considered fuel utilization rates of 90% for RSOCEV and 40% for ICEV [44]. Subsequently, the corresponding weight and volume of hydrogen can be calculated as follows:

$$m_{H_2} = \frac{E}{\mu \times LHV_{H_2}} \quad (2.5)$$

Where m_{H2} is the weight of hydrogen required (kg), E is the total energy output of the stack (kWh), μ is the fuel utilization rate for RSOCEV, and LHV_{H2} is the lower heating value of H_2 (kWh kg^{-1}).

The total energy output of ICEV were calculated as follows:

$$E_{ICEV} = m_{gas} \times LHV_{gas} \times \mu_{ICEV} \quad (2.6)$$

Where E_{ICEV} is the total energy output of ICEV (kWh), m_{gas} is weight of the gasoline (kg), LHV_{gas} is the lower heating value of gasoline (kWh kg^{-1}), and μ_{ICEV} is the fuel utilization rate for ICEV.

Table 2. Parameters for calculating power and energy densities.

<table>
<tr><th colspan="2">ICEV</th><th colspan="2">BEV</th><th colspan="2">RSOCEV</th></tr>
<tr><td rowspan="2">Engine [45]</td><td>100.0 L</td><td rowspan="5">Battery[42]</td><td rowspan="2">400.0 L</td><td>Stack</td><td>63.0 L</td></tr>
<tr><td>200.0 kg</td><td></td><td>109.0 kg</td></tr>
<tr><td rowspan="3">Gas [46]</td><td rowspan="2">60.0 L</td><td rowspan="3">537.0 kg</td><td rowspan="2">Tank [43]</td><td>123.0 L</td></tr>
<tr><td>87.5 kg</td></tr>
<tr><td rowspan="2">35.0 kg</td><td rowspan="2">Hydrogen</td><td>123.0 L</td></tr>
<tr><td>4.9 kg</td></tr>
<tr><td>LHV_{gas} [47]</td><td>12.7 kWh kg^{-1}</td><td colspan="2"></td><td>LHV_{H2} [47]</td><td>33.3 kWh kg^{-1}</td></tr>
<tr><td colspan="6">Power output [42,46]</td></tr>
<tr><td colspan="2">152.0 kW</td><td colspan="2">494.0 kW</td><td colspan="2">494.0 kW</td></tr>
<tr><td colspan="6">Energy output [42]</td></tr>
<tr><td colspan="2">178.0 kWh</td><td colspan="2">98.0 kWh</td><td colspan="2">98.0 kWh</td></tr>
</table>

2.3.2.3 Charging/refueling time of RSOCEVs and comparison with BEVs and ICEVs.

The charging time of RSOCEVs was calculated under the assumptions mentioned above. The equation (6) below follows the parameters set for the RSOCEV stack previously:

$$T = \frac{m_{H_2} * 1000}{i \times \frac{\frac{V_{stack} \times 1000}{t}}{2 \times F} \times M_{H_2} \times 60} \quad (2.7)$$

Where T is the charging time of RSOCEV (min), M_{H2} is the molar mass of H_2 (g mol^{-1}), F is the Faraday constant (96485 C mol^{-1}), and i is the areal current density of single cell at 1.3 V and 750 °C (2.0 A cm^{-2}).

Table 3. Parameters for comparing the charging/refueling time of ICEVs, BEVs, and RSOCEVs

Vehicles with different power systems	Charging/refueling time (min)
ICEV [48]	3
BEV [42]	30
RSOCEV	12

2.3.2.4 Fuel economy comparison of these three types of vehicles

Fuel economy is of great interest to consumers. However, when comparing gasoline-powered vehicles with their electric counterparts, various factors must be taken into consideration, including local electricity and gasoline prices. To address this, the merit of kWh per 100 miles was introduced by the EPA, offering a more direct comparison. The total mileage of ICEV is calculated as follows:

$$M_{T\_ICEV} = MPG \times G \tag{2.8}$$

Where M_{T_ICEV} is the total mileage of ICEV (miles), MPG is the miles per gallon, which is 32, and G is the fuel capacity of the ICEV, which is 15.8 gallon [46].

And the total mileage of SOCEVs is estimated in the following way:

$$M_{T\_RSOCEV} = M_{T\_BEV} \times \frac{\eta_{RSOCEV}}{\eta_{BEV}} = \frac{M_{T\_BEV}}{\eta_{BEV}} \times \left(\frac{\Delta G}{\Delta H_{HHV}} \times \frac{V}{E} \times \frac{1}{\lambda}\right) \tag{2.9}$$

Where M_{T_RSOCEV} is the total mileage of RSOCEV (miles), M_{T_BEV} is the total mileage of BEV (446 miles [42]), η_{RSOCEV} is the fuel-to-electricity efficiency of RSOCEV, η_{BEV} is the fuel-to-electricity efficiency of BEV (~90% [49]), ΔG is the change in the Gibbs free energy of hydrogen oxidation (-237.1 kJ mol^{-1}), ΔH_{HHV} is the higher-heating value reaction enthalpy change of

hydrogen oxidation (-285.8 kJ mol^{-1}), V is the terminal voltage of the single cell in FC mode (V), E is the reversible voltage (V), and λ is 1.1, assuming fuel utilization rate is ~90% [50].

The calculated kWh per 100 miles values for these three types of vehicles are shown in Table 4 below.

Table 4. Calculated kWh per 100 miles of ICEVs, BEVs, and RSOCEVs

Vehicles with different power systems	kWh/100 miles
ICEV	35.2
BEV	22.0
RSOCEV	28.2

2.3.2.5 Energy efficiency (EE) and electric power consumption (EPC) of CO_2 MS-SOECs

For the electrochemical reduction of CO_2 to CO, EE is defined as

$$EE = \frac{\Delta H_{CO,LHV} \times n_{CO,produced} \times 1000}{P_{d.c.}} = \frac{\Delta H_{CO,LHV} \times \frac{FE \times i}{n \times F} \times 1000}{i \times V} \times 100\% \quad (2.10)$$

Where $\Delta H_{CO,LHV}$ is the LHV reaction enthalpy for CO_2 electrolysis (kJ mol^{-1}), $n_{CO,produced}$ is the CO production rate (mol s^{-1}), and $P_{d.c.}$ is the external power applied (W). FE is the Faradaic efficiency of CO_2 MS-SOECs, which is 100%. i is the applied current density (A cm^{-2}), while V is the corresponding voltage.

EPC quantifies the amount of electric energy required to produce 1 kg of CO gas. EPC is defined as

$$EPC = \frac{E \times n \times F}{(FE) \times m_m} \quad (2.11)$$

Where E is the cell voltage, n stands for the quantity of transferred electrons (n=2), F is Faraday's constant, FE denotes Faradaic efficiency which is 100%. m_m represents the molar mass of the produced CO [51].

Chapter 3 - Boosting the performance of reversible solid oxide electrochemical cells with a novel hybrid oxygen electrode, $Pr_{1.39}Ba_{0.14}Sr_{0.53}Co_{1.48}Fe_{0.76}O_{6-\delta}$-$Ba_{0.66}Sr_{0.34}CoO_{3-\delta}$

3.1 Hybrid oxygen electrode enables improved performance in both fuel cell and electrolysis modes

Hybrid oxygen electrodes have been widely developed to enhance SOEC performance for power generation and hydrogen production [39,52–55]. Despite the outstanding results that have been achieved, the performance, especially the energy efficiency in steam electrolysis mode, should be further enhanced to achieve the U.S. Department of Energy (DOE) renewable hydrogen production cost goal of <$1 kg^{-1} [56], while increasing the hydrogen production rate per active area. Therefore, we have developed a new hybrid oxygen electrode, PBSCF-b+BSC, via the in-situ formation process, which simplifies the oxygen electrode fabrication process and improves the electrocatalytic activity. Figure 4 schematically displays this hybrid electrode, which is composed of the PBSCF-b phase and a minor BSC phase that is dispersed on the PBSCF-b phase. First, the PBSCF-b phase has an improved bulk oxygen-ion diffusion coefficient. Additionally, the BSC phase exhibits a much higher surface oxygen exchange coefficient. Therefore, this composite electrode leads to synergistic effects, which improve the ORR and OER activity.

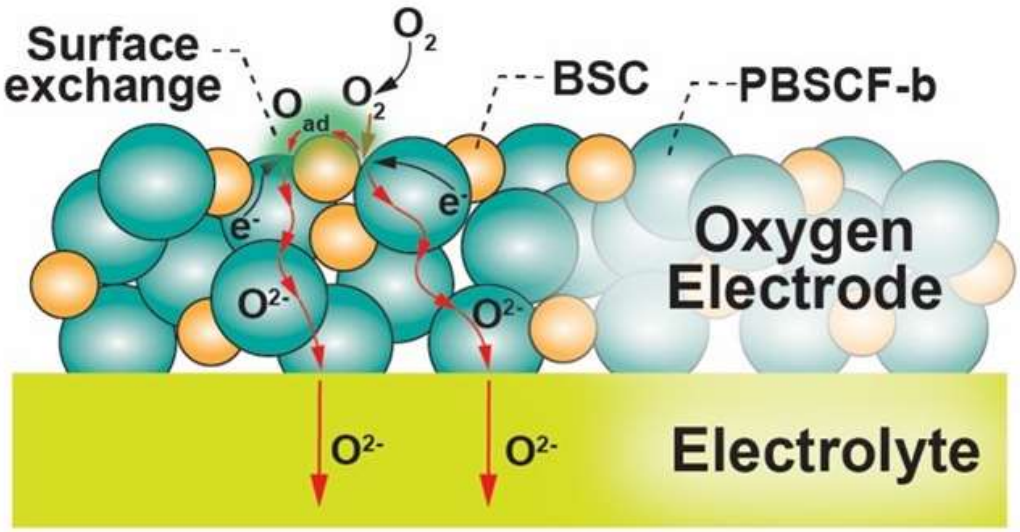

Figure 3. Schematic illustration of the SOEC with the newly developed hybrid electrode in fuel cell mode, which displays the oxygen reduction reaction.

As shown in Figures 5-7, the YSZ-based SOECs equipped with this new hybrid electrode achieve remarkable performance for both hydrogen production and power generation (Table A2) [11,12,16,28,29,31,57–64]. First, as displayed in Figure 5, the SOECs simultaneously attain high hydrogen production rate, while achieving lower hydrogen production cost than SOECs reported in literature (see Materials and Methods). At 750 °C and 1.3 V, our SOECs obtain a current density of 4.4 A cm^{-2}, which represents the highest performance among all YSZ-based SOECs (Figure 6). Furthermore, our SOECs also realize exceptional fuel cell performance using hydrogen and propane as the fuel (Figure 7). These promising results have emphasized that PBSCF-b+BSC is a high-performing oxygen electrode for SOECs.

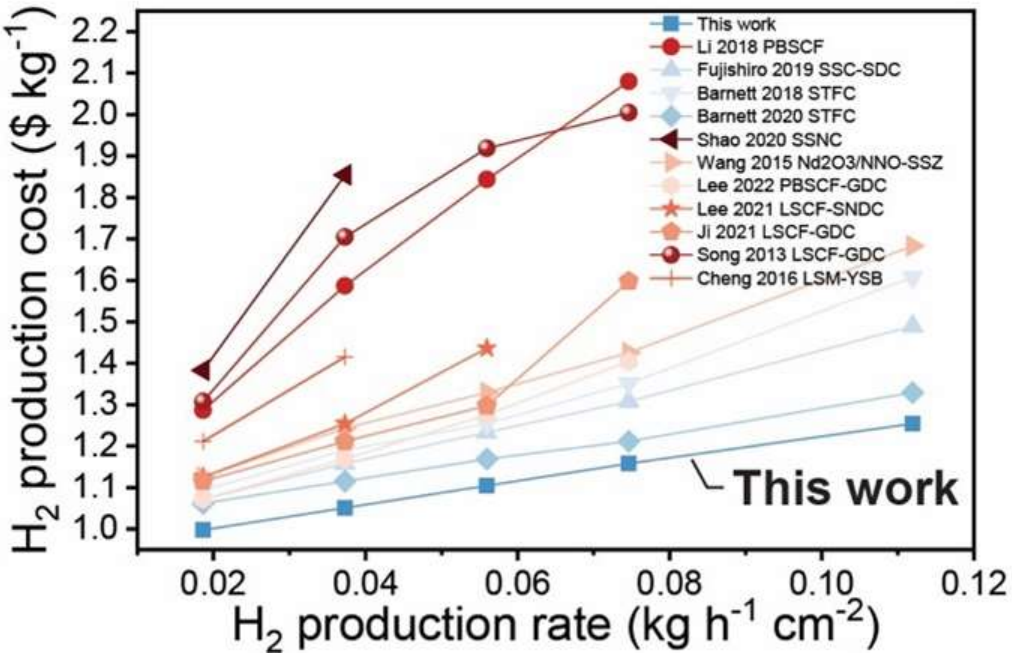

Figure 4. The H_2 production cost as a function of H_2 production rate achieved in this work and reported in literature results [12,14–16,59,61,65–70].

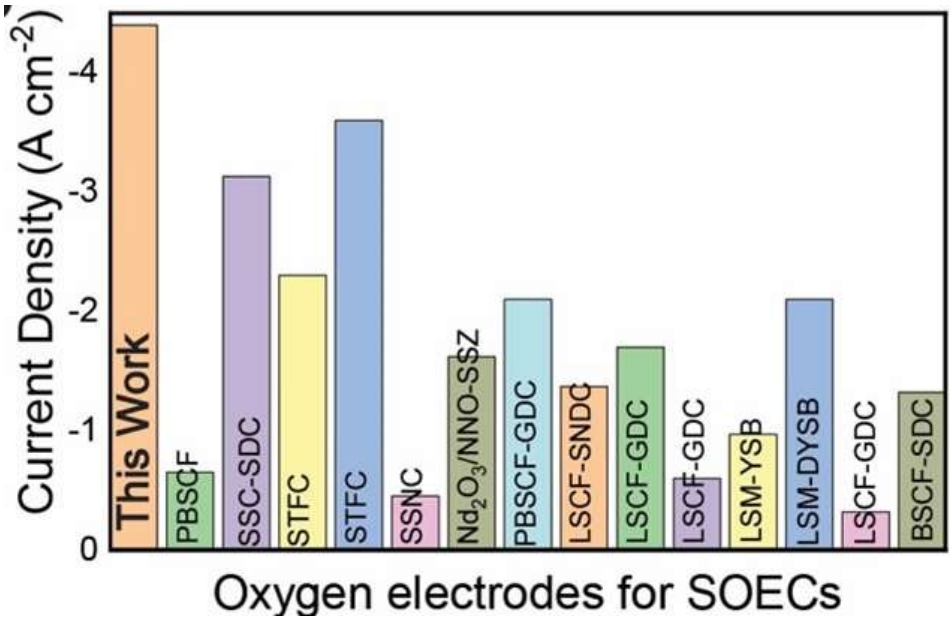

Figure 5. Performance comparison of YSZ-based SOECs in steam electrolysis mode, which indicates our SOECs equipped with the hybrid oxygen electrode achieve unprecedented performance (Table A1).

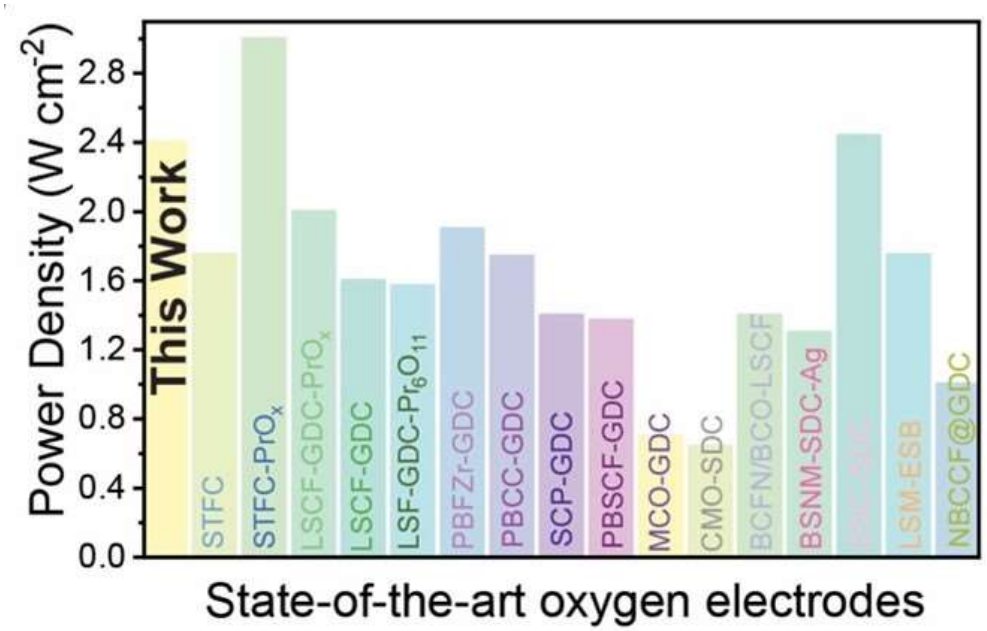

Figure 6. Comparison of peak power densities of our YSZ based SOEC in fuel cell mode with literature results (Table A2).

3.2 Structural properties of the in-situ formed hybrid electrode

The hybrid electrode was synthesized via the wet-chemistry method, which has been widely used for synthesizing SOEC electrode materials [14,71–73]. In brief, a stoichiometric amount of the precursors (Pr_6O_{11}, $Ba(NO_3)_2$, $Sr(NO_3)_2$, $Co(NO_3)_2 \cdot 6H_2O$, and $Fe(NO_3)_3 \cdot 9H_2O$) was mixed with DI water, chelating agents (citric acid and ethylenediaminetetraacetic acid), and ammonium hydroxide solution, which was then stirred and heated at 300 °C for 5-10 hours, leading to the production of a gel. The gel was dried at 175 °C overnight and then calcined at 650 °C for 5 h to achieve highly porous black powder, which was subsequently calcined at 750-770 °C to obtain the hybrid electrode. Additionally, we synthesized the previous single-phase PBSCF-a as the baseline material (see Materials and Methods).

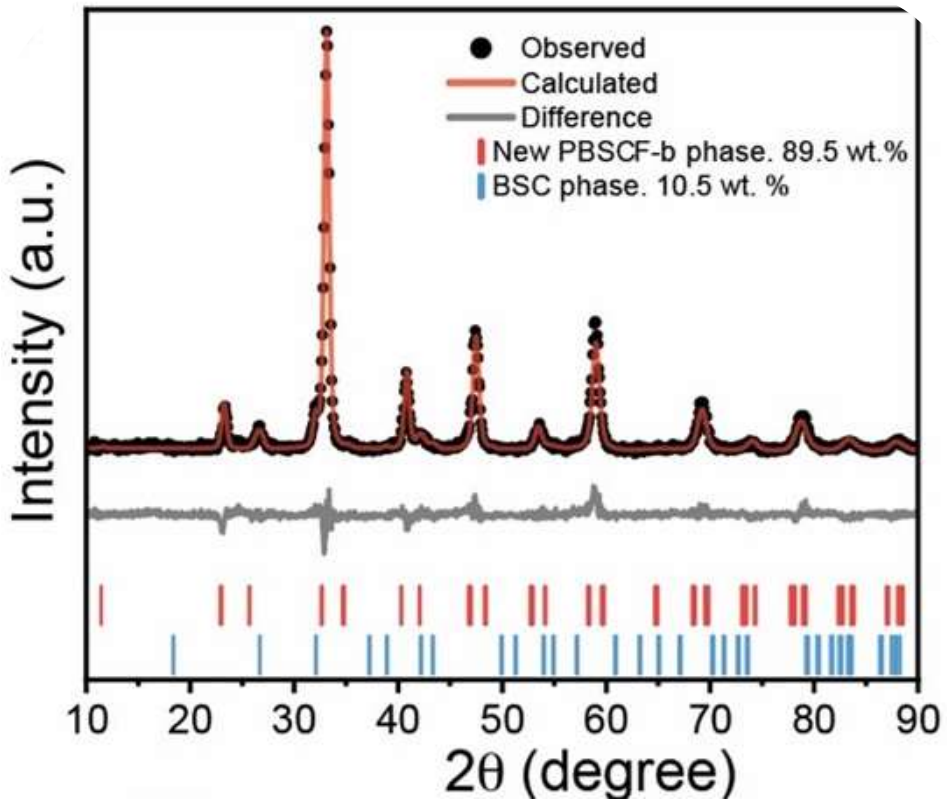

Figure 7. The XRD pattern and Rietveld refinement of as-synthesized hybrid electrode.

Figure 8 displays the XRD pattern of the in-situ formed hybrid electrode, which confirms that this new composite electrode is composed of a new PBSCF-b phase (tetragonal, P4/mmm) and a BSC phase (hexagonal, P63/mmc). The following TEM-EDX results were used to quantitively determine the exact stoichiometries for both phases ($Pr_{1.39}Ba_{0.14}Sr_{0.53}Co_{1.48}Fe_{0.76}O_{6-\delta}$ and $Ba_{0.66}Sr_{0.34}CoO_{3-\delta}$), which were used as the input to perform the Rietveld refinement. As shown in Figure 8 and Table A3, it has been identified that the hybrid electrode consists of 89.5 wt. % PBSCF-b phase and 10.5 wt. % BSC phase. Additionally, the refinement achieves a Chi value of 1.978, and both wRp and Rp values remain below 15%, indicating the refinement is reliable and the chemical stoichiometries determined by TEM-EDX are consistent with the refinement results. On the other hand, as shown in Figure A1, the previous PBSCF-a is a single phase (orthorhombic, Pmmm).

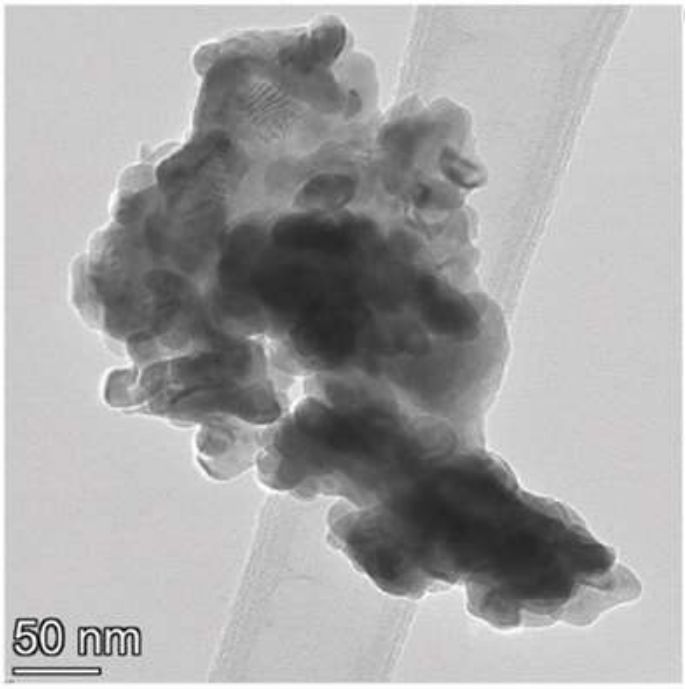

Figure 8. Bright-field TEM image of the hybrid electrode.

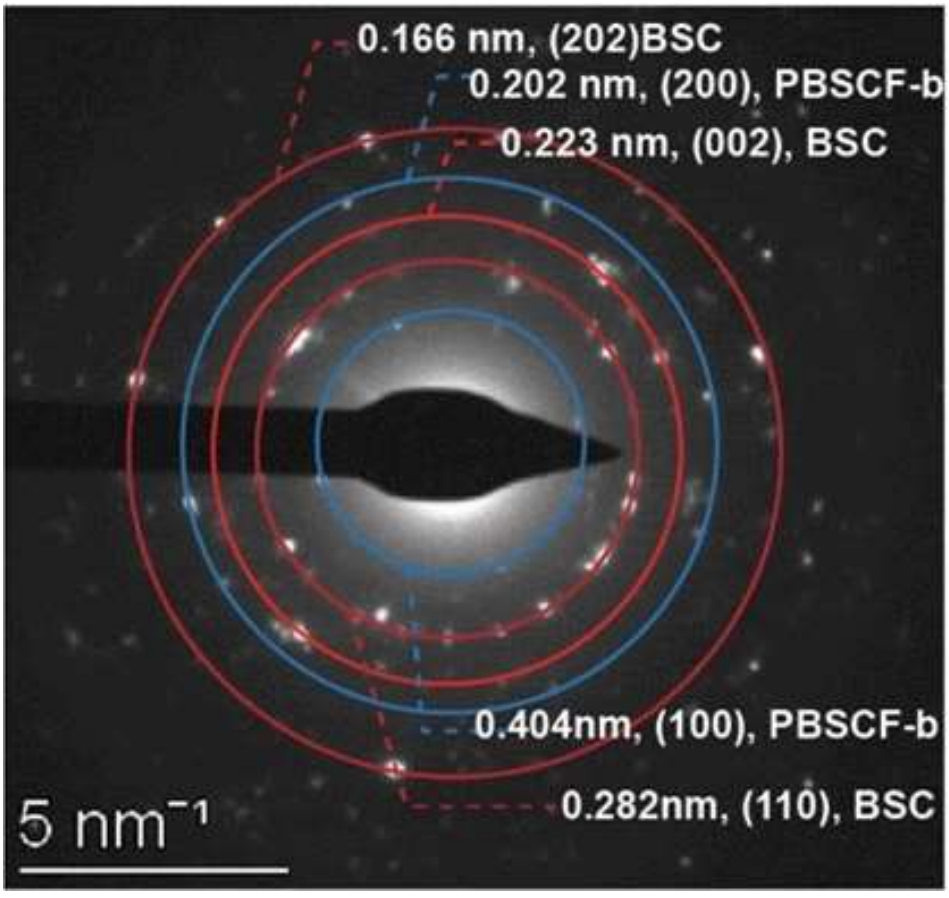

Figure 9. The SAED patterns collected from the area shown in Figure 9.

Transmission electron microscopy (TEM), energy dispersive X-ray spectroscopy (EDX), and selected area electron diffraction (SAED) were performed to better study the microstructure, crystal structure, and chemical compositions of this new hybrid electrode. The hybrid electrode powder displays a microstructure of nanosized particles with a particle size of ~50 nm (Figure 9). The SAED patterns as shown in Figure 10 further validate that this hybrid electrode is composed of the BSC phase and a PBSCF-b phase. The diameter of each ring corresponds to the interplanar distance (d-spacing) of crystal planes present in this electrode. The d-spacing values of 0.166 nm, 0.223 nm, and 0.282 nm correspond to (202), (002), and (110) planes of BSC, respectively. The d-spacing values of 0.202 nm, 0.404 nm, and 0.273 nm corresponding to (200), (100), and (102) planes of the PBSCF-b phase (Figure A2). These results are consistent with the high-resolution TEM (HR-TEM) images shown in Figure 12 and the XRD refinement results (Table A3).

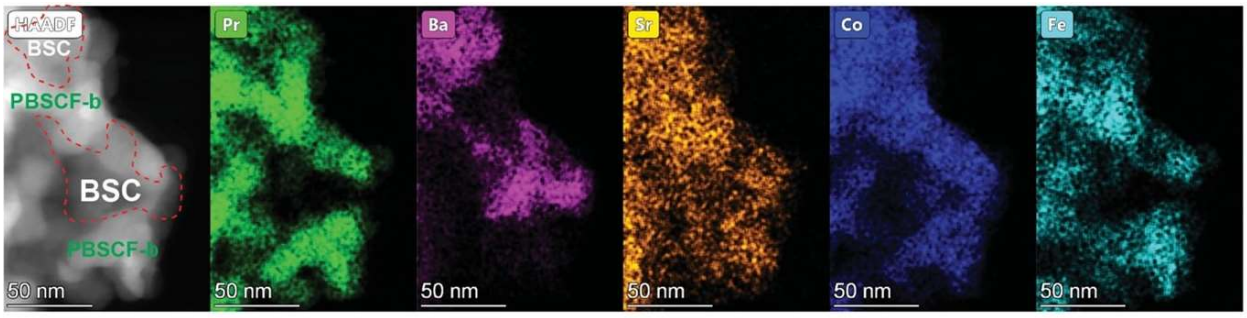

Figure 10. HAADF-STEM image and corresponding EDX elemental mapping images of the hybrid electrode.

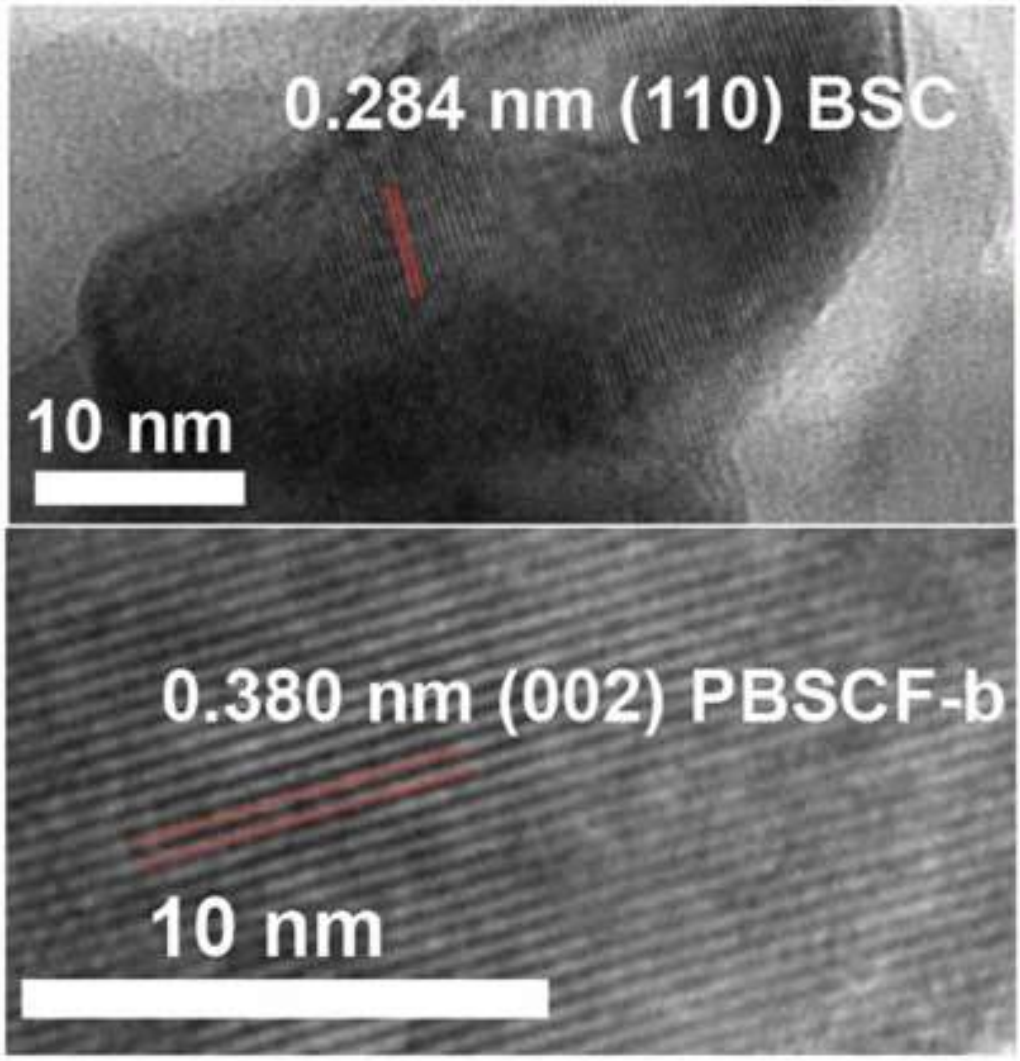

Figure 11. HR-TEM images of PBSCF-b phase and BSC phase.

Additionally, S/TEM-EDX images and spectra were collected to quantitively determine the stoichiometries of both phases presented in the hybrid electrode. The EDX mapping images shown in Figure 11 clearly show that the hybrid electrode consists of one Ba-rich phase and one Pr-rich phase, which correspond to the BSC and PBSCF-b, respectively. The detailed analysis of the EDX spectrum shown in Figure 14 determines the stoichiometry of the BSC phase as $Ba_{0.66}Sr_{0.34}CoO_{3-\delta}$, while that of the new PBSCF-b phase is $Pr_{1.39}Ba_{0.14}Sr_{0.53}Co_{1.48}Fe_{0.76}O_{6-\delta}$. The presence of both phases is further substantiated by the additional mapping images depicted in Figure A3 and A4. As mentioned above, these stoichiometries were used to perform the XRD refinement with valid results, indicating that the stoichiometries are correct.

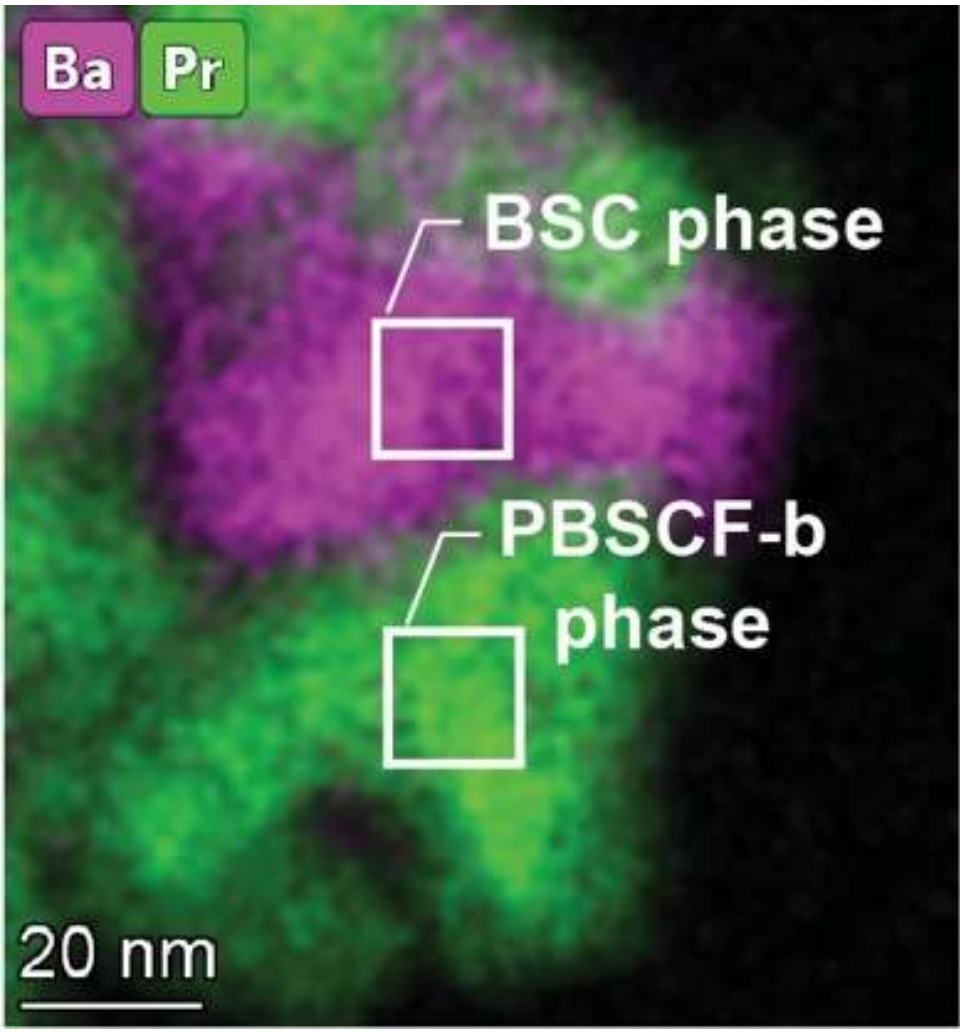

Figure 12. Overlay chemical mapping image with both Ba and Pr elements, which shows the Ba-rich area (magenta) is BSC and the Pr-rich area (green) is the PBSCF-b phase.

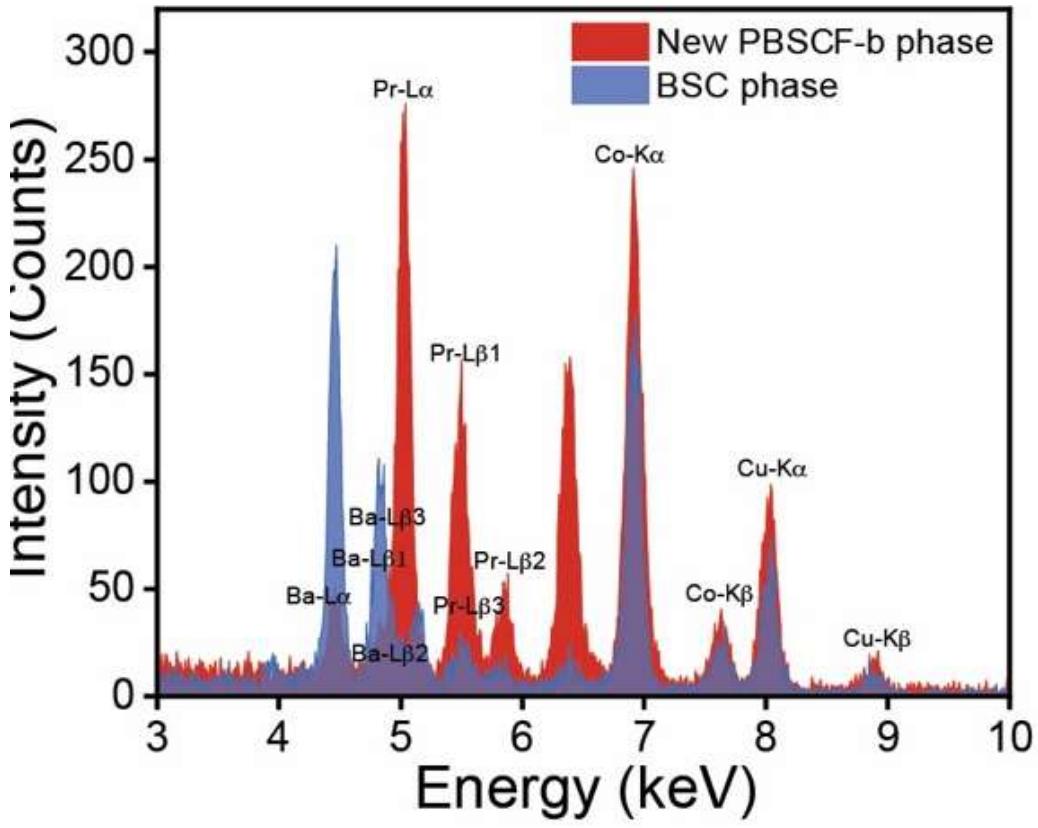

Figure 13. EDX spectra of the BSC phase and PBSCF-b phase (see the marked boxes in Fig 2F), which were used to quantify the stoichiometries of these two phases.

3.3 Hybrid oxygen electrode enhances surface oxygen exchange coefficient and bulk oxygen-ion diffusion coefficient, leading to improved electrochemical performance.

We hypothesized that the two phases in the hybrid electrode can synergize to achieve improved electrochemical properties, such as faster surface oxygen exchange and bulk oxygen-ion diffusion kinetics. Therefore, electrical conductivity relaxation (ECR) was performed, and subsequent analysis using the NETL-developed software [74] was conducted to determine the surface oxygen exchange coefficient (k_{chem}) and bulk oxygen-ion diffusion coefficient (D_{chem}) (Figure A5, A6). Figure 15 compares the k_{chem} of this new hybrid electrode and previous PBSCF-a, indicating that the hybrid electrode significantly accelerates the surface oxygen exchange kinetics. For example, at 700 °C, the k_{chem} of the hybrid electrode is 1.6×10^{-4} cm s^{-1}, which is 45% higher than that of previous PBSCF-a (1.1×10^{-4} cm s^{-1}). Additionally, the corresponding activation energy of the hybrid electrode (87.1 kJ mol^{-1}) is much lower than the previous PBSCF-a (123.9 kJ mol^{-1}), indicating that the surface oxygen exchange process exhibits lower energy barrier, which is essential for achieving high ORR and OER activity at reduced operating temperatures. Furthermore, Figure 16 shows that the D_{chem} of the hybrid electrode is also higher than that of previous PBSCF-a. Moreover, the corresponding activation energy of the hybrid electrode is also lower than that of previous PBSCF-a. These results imply that the hybrid electrode can be employed to build SOECs operating at reduced operating temperatures.

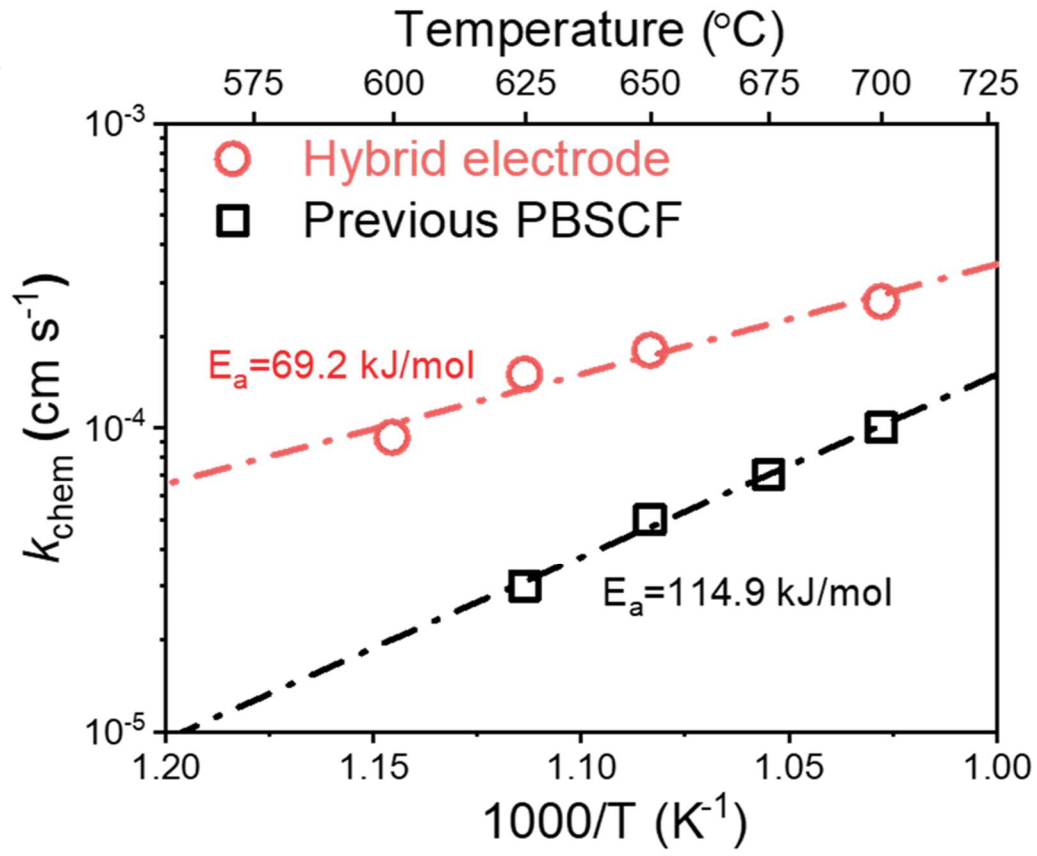

Figure 14. surface oxygen exchange coefficients (k_{chem}) for the hybrid electrode and previous PBSCF-a.

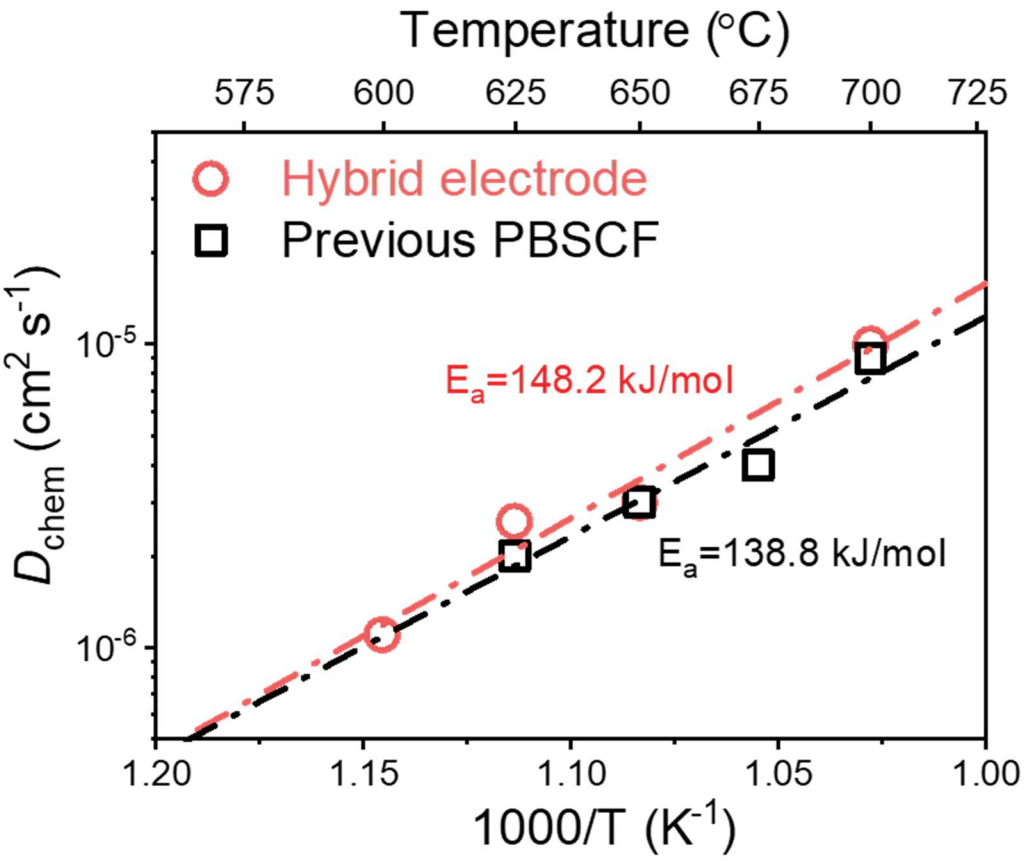

Figure 15. bulk oxygen-ion diffusion coefficient (D_{chem}) for the hybrid electrode and previous PBSCF-a.

We also measured and compared the area-specific electrode polarization resistance (ASR_p) and ohmic resistance (ASR_{ohm}) of SOECs with the hybrid electrode and the previous PBSCF-a electrode. As shown in Figure 17, the new hybrid electrode leads to a much lower ASR_p than the previous PBSCF-a electrode, affirming the conclusion that the hybrid electrode can achieve improved electrocatalytic activity. Furthermore, the Arrhenius plots of ASR_p as a function of operating temperature show that the hybrid electrode exhibits a lower activation energy (42.0 kJ mol^{-1}) than that of the previous electrode (44.8 kJ mol^{-1}), which is consistent with the k_{chem} and D_{chem} results. On the other hand, employing the new hybrid electrode does not obviously affect the ASR_{ohm} (Figure 18), indicating that the hybrid electrode does not lead to any deleterious chemical reactions between the electrode and oxygen electrode, suggesting that the new hybrid electrode is chemically compatible with the electrolyte.

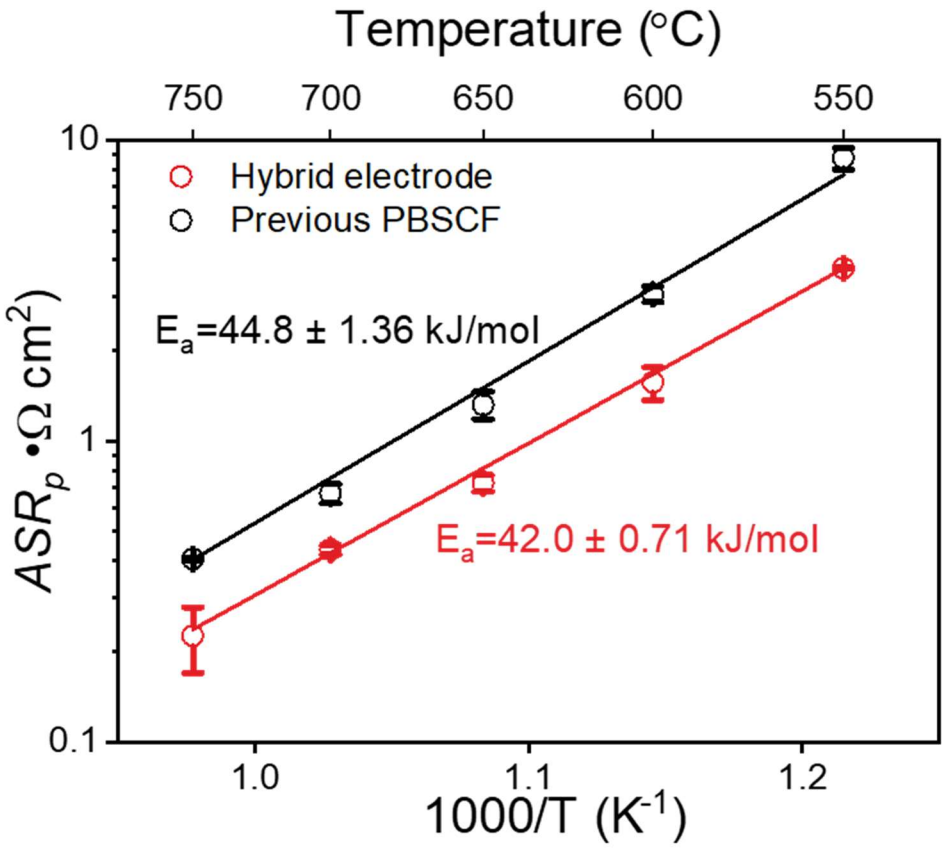

Figure 16. Area-specific electrode polarization resistance (ASR_p) of SOECs equipped with the hybrid electrode and the previous PBSCF-a electrode, which were measured under OCV conditions.

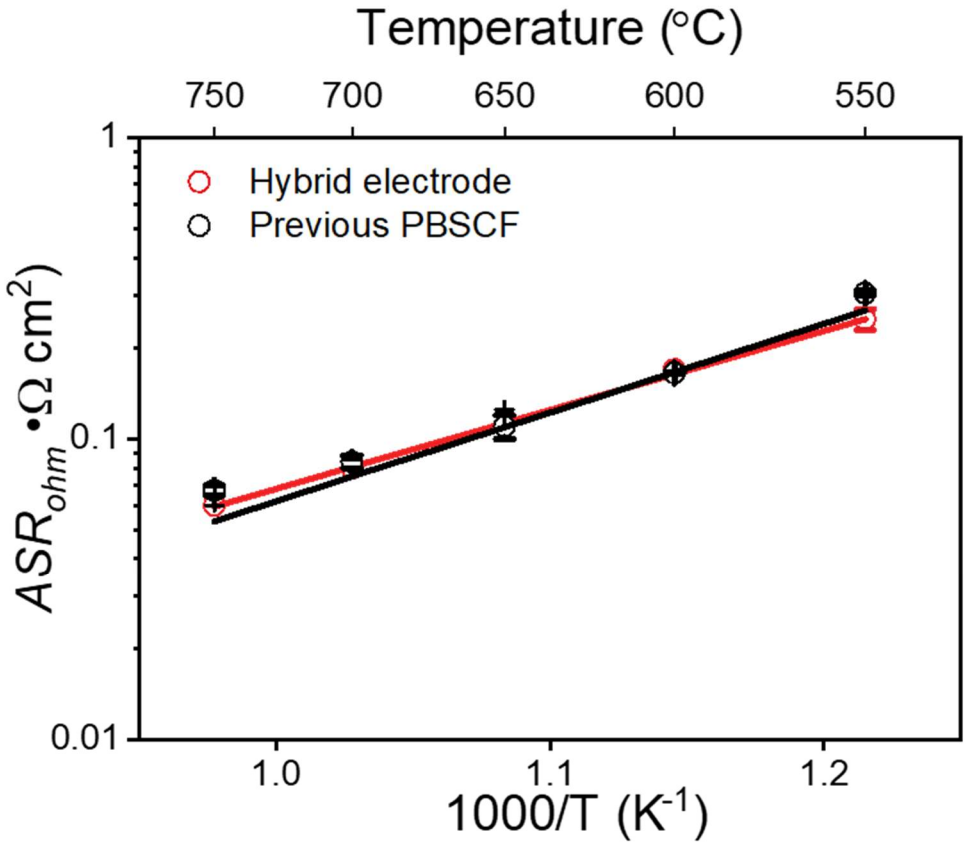

Figure 17. Area-specific ohmic resistance (ASR_{ohm}) of SOECs equipped with the hybrid electrode and the previous PBSCF-a electrode, which were measured under OCV conditions.

To gain an in-depth understanding of why the hybrid electrode leads to improved electrochemical performance, the distribution of relaxation time (DRT) analysis of EIS spectra was performed. The DRT analysis is a convenient and potent method for distinguishing the resistance ascribed to different processes occurring at the electrodes. To transform EIS data into the time domain, the DRT software developed by Ciucci et al. was used [75], and a Gaussian distribution was employed. Representative EIS spectra at 700 °C and 0.8 V and corresponding DRT analysis results are presented in Figures 19 and 20. Each DRT analysis plot consists of five distinct peaks, which are denoted as P1- P5, starting from the high frequency. In general, the processes associated with P4 and P5 correspond to mass transfer processes, including the gas diffusion within the pores of both the oxygen electrode and the fuel electrode, and the transport of ionic/electronic defects within the porous solid electrodes [71,76]. The process associated with P3 is likely to be the hydrogen oxidation reaction occurring at the hydrogen electrode (i.e., fuel electrode) [8,77]. The process represented by P2 is deemed as the key step because the integrated area of each peak represents the resistance of the process, and P2 shows the highest resistance [6,57,76]. This process can be ascribed to the surface oxygen exchange process, including oxygen adsorption, dissociation, and surface transport, which is also the main difference between the hybrid electrode and previous PBSCF-a. The process represented by P1 is widely accepted to be the charge transfer process across the electrode/electrolyte interface [71,78].

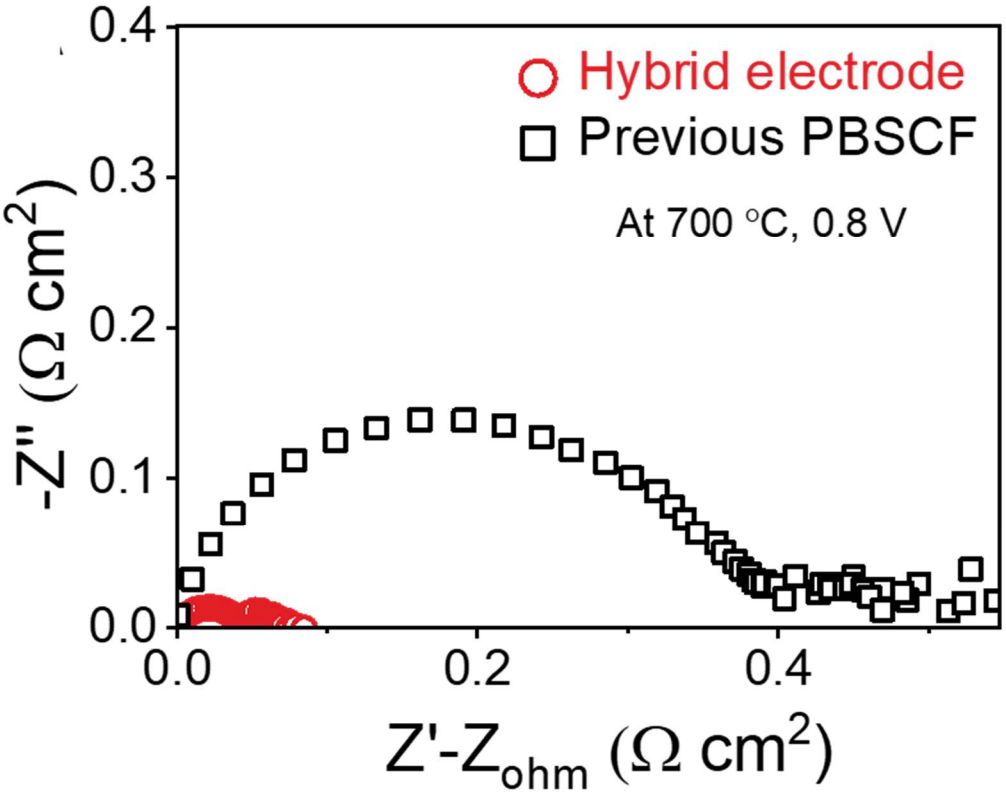

Figure 18. Representative EIS comparison at 700 °C under 0.8 V.

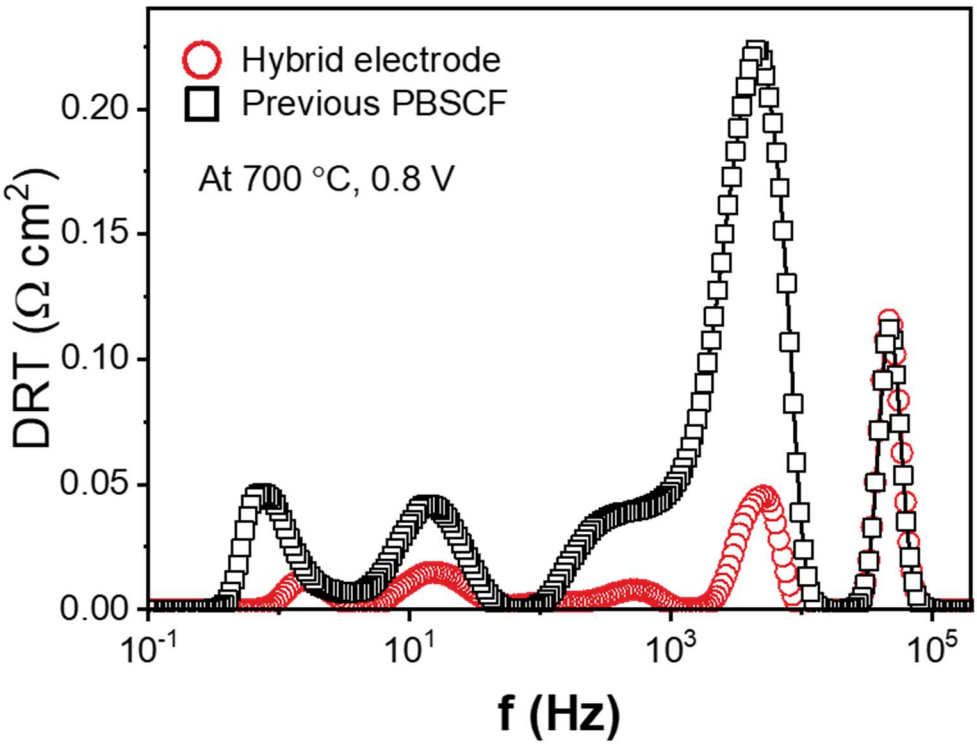

Figure 19. DRT analysis of EIS data shown in Figure 19.

As shown in Figure 20, employing the hybrid oxygen electrode primarily reduces the resistance corresponding to the surface oxygen exchange (P2), which further confirms that the hybrid oxygen electrode can significantly facilitate the surface oxygen exchange. This new electrode does not affect the electrolyte/electrode interfacial charge transfer, which is consistent with the results shown in Figure 22, where the new electrode does not affect ASR_{ohm}. Figure 20 also indicates that the new hybrid electrode slightly reduces the resistance ascribed to the mass transport which could be due to its relatively high porosity as the hybrid electrode was sintered at a lower temperature than the previous PBSCF-a.

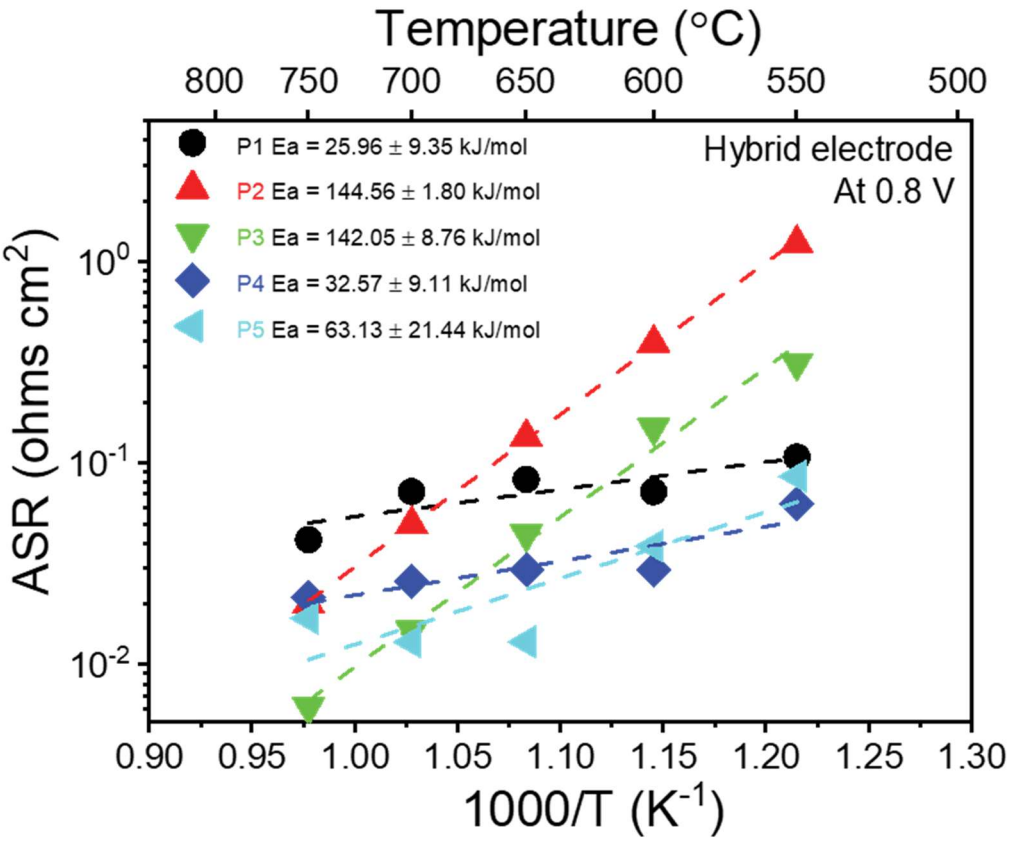

Figure 20. Temperature dependence of the partial polarization resistances of the electrode reactions of SOFCs with hybrid electrodes at 0.8 V.

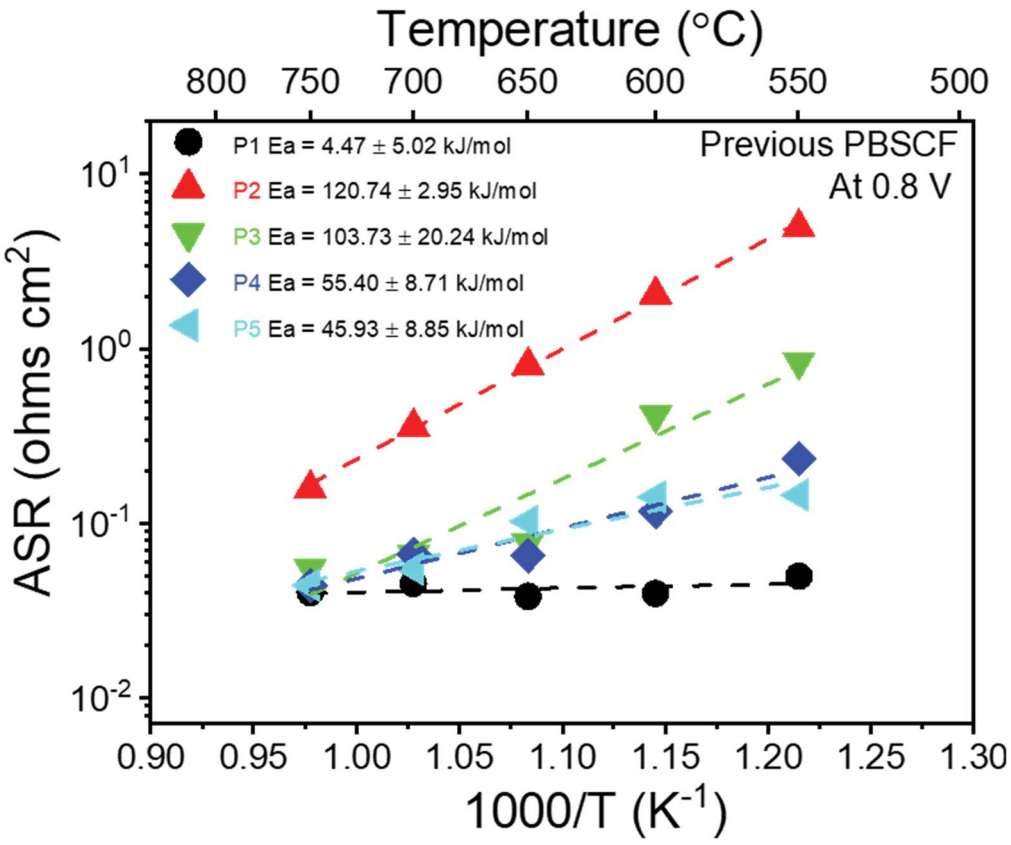

Figure 21. Temperature dependence of the partial polarization resistances of the electrode reactions of SOFCs with previous PBSCF-a electrodes at 0.8 V.

After analyzing the DRT peaks, the temperature dependences of the area-specific resistances of each peak were plotted for both the hybrid electrode and the previous PBSCF-a. The resistance of the P2 process, which is associated with the surface oxygen exchange and oxygen ion diffusion processes, has the highest activation energy for both electrode materials. The process that corresponds to P2 mainly contributes to the polarization resistance at relatively low operating temperatures, and this is particularly evident for the previous PBSCF-a. On the other hand, the resistance of the charge transfer at the interface (P1) has a much weaker temperature dependency, which is in good agreement with literature studies [79,80]. For the hybrid electrode, the P1 process is the major contribution in the higher temperature range. However, due to its much lower activation energy, its influence on the total resistance decreases as the temperature decreases. The temperature dependence of the resistance of the P3 process, which is associated with the hydrogen electrode, is strong for both electrode materials, with an activation energy of 142.05 kJ mol^{-1} for the hybrid electrode and 103.73 kJ mol^{-1} for previous PBSCF-a. Compared to other processes, the resistances associated with P4 and P5 are less significant, as the processes associated with P4 and P5 are related to gas diffusion [81].

3.4 SOECs equipped with the hybrid oxygen electrode achieve outstanding fuel cell performance.

To assess the SOEC performance in fuel cell mode, a set of SOECs equipped with both the hybrid oxygen electrode and the previous PBSCF-a electrode were tested. Figure A7 shows the lab-scale SOECs employed to evaluate the oxygen electrodes. The oxygen electrode effective area is 0.5 cm^2. As detailed in the Materials and Methods, the SOECs were manufactured via co-tape casting, producing SOEC half cells that were highly reproducible, highly uniform, and

defect-free, and had dense electrolytes with a thickness of ~8 μm (Figure A8), which is essential for fairly investigating different oxygen electrode materials.

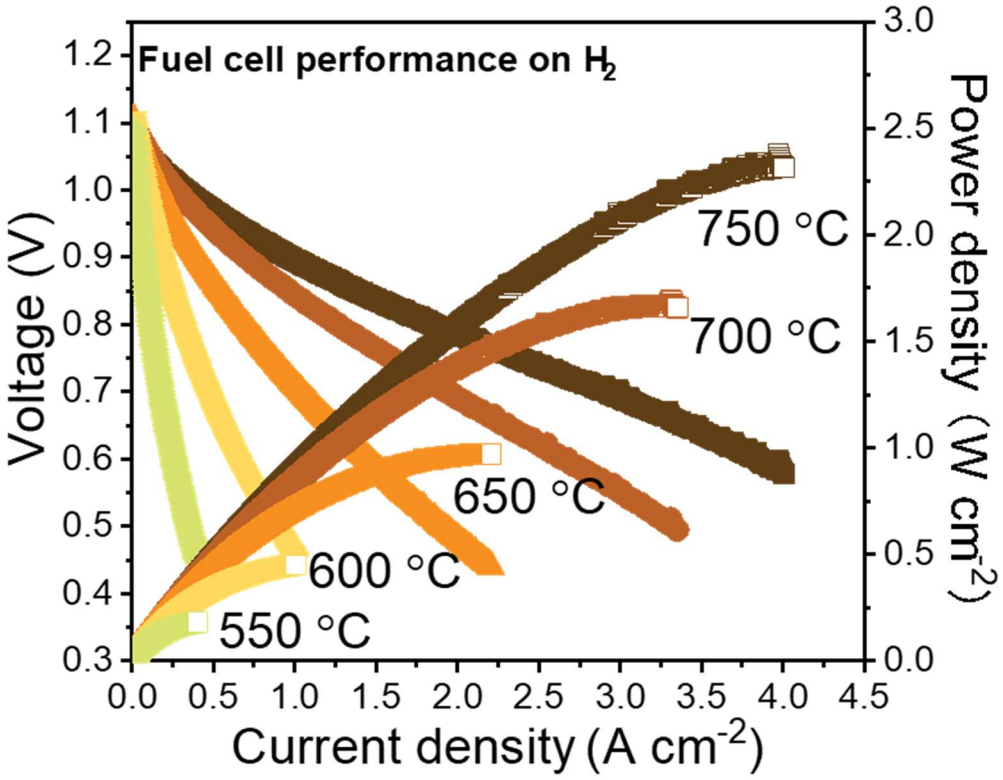

Figure 22. I-V and I-P curves of the SOECs with the hybrid oxygen electrode at different operating temperatures. H_2 is fed to the fuel electrode as fuel.

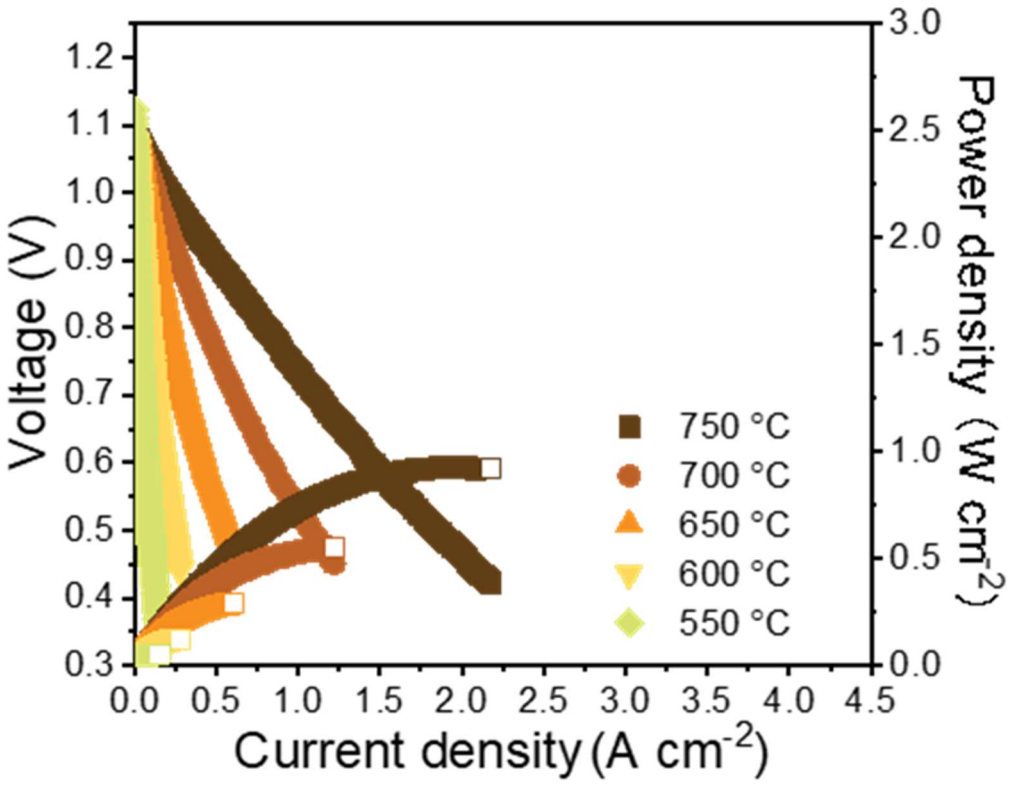

Figure 23. I-V and I-P curves of the SOECs with the previous PBSCF-a oxygen electrode at different operating temperatures. H_2 is fed to the fuel electrode as fuel.

Figure 23-28 summarizes the fuel cell performance under various conditions. All SOECs tested in this work show an OCV of ~1.1 V at 750 °C, which is close to the theoretical value, indicating that there is no gas leakage and that the performance evaluation is valid. Figure 23 shows that the SOEC with the hybrid oxygen electrode attains peak power densities of 2.4, 1.6, 0.9, 0.4, and 0.2 W cm^{-2} at 750 °C, 700 °C, 650 °C, 600 °C and 550 °C, respectively. The peak power densities achieved with the hybrid electrode are 2-4 times as high as that achieved with the previous PBSCF-a oxygen electrode (Figure 24-26). The demonstrated improvement in fuel cell performance can be investigated by conducting EIS, with representative EIS spectra shown in Figures 25. Notably, the ASR_p was observed to be much lower using the hybrid oxygen electrode compared to the previous PBSCF-a. Furthermore, the excellent fuel cell performance

was also demonstrated using C_3H_8 as the fuel. As shown in Figure 27, peak power densities of 2.5, 1.6, 0.9, 0.5, and 0.25 W cm^{-2} were demonstrated at 750 °C, 700 °C, 650 °C, 600 °C, and 550 °C, respectively. Figure 28 indicates the direct-C_3H_8 SOECs demonstrated in this work represent the world record performance.

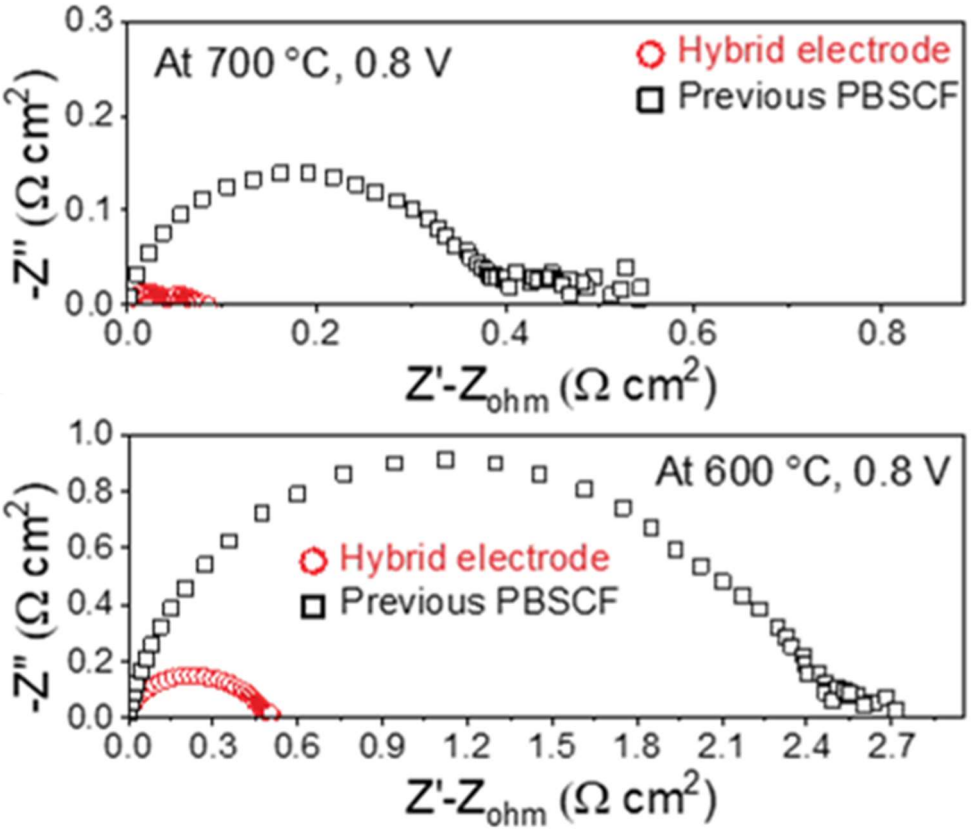

Figure 24. EIS spectra of the SOECs with two electrodes, which were collected at 0.8V, at temperatures of 700 °C and 600 °C, respectively.

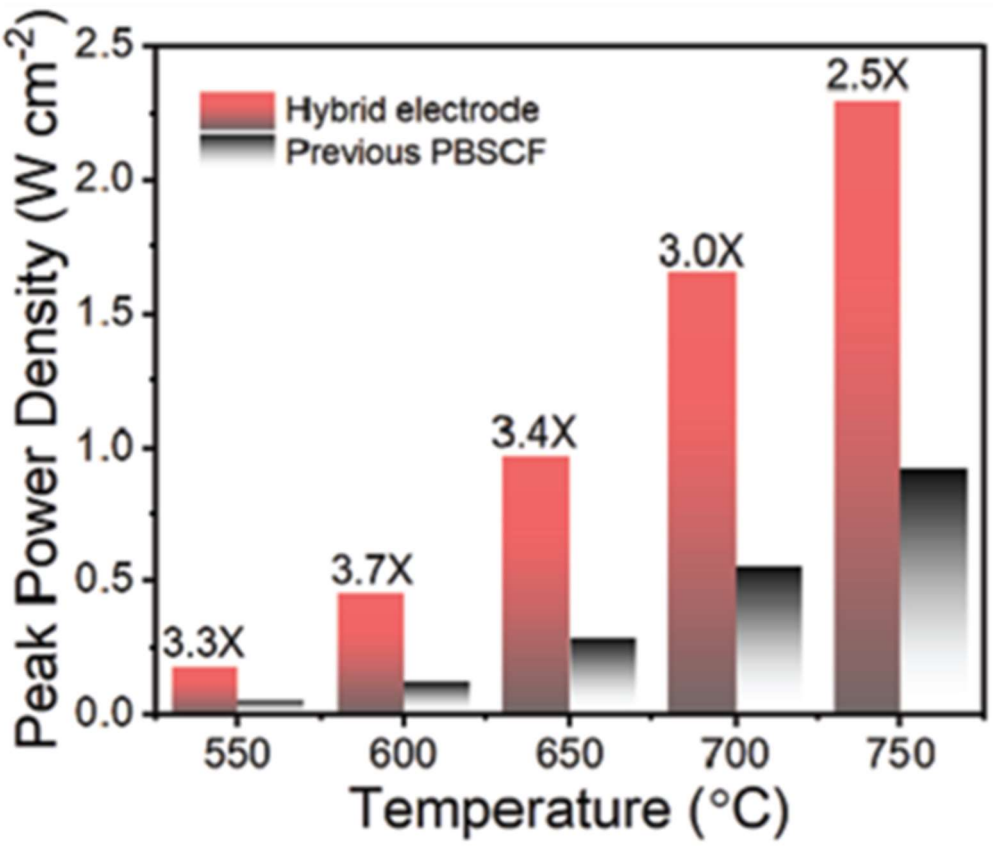

Figure 25. Comparison of the SOEC peak power densities achieved with the hybrid oxygen electrode and previously developed PBSCF-a electrode.

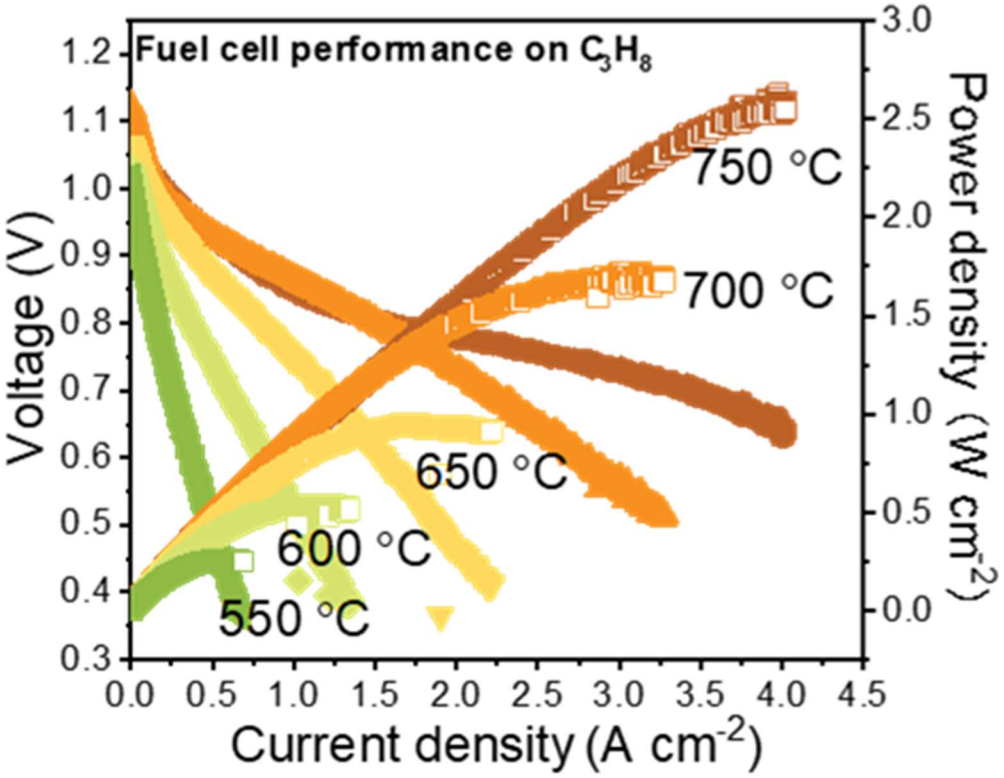

Figure 26. I-V and I-P curves of the SOEC with the hybrid oxygen electrode. Humidified C_3H_8 was fed to the fuel electrode as fuel.

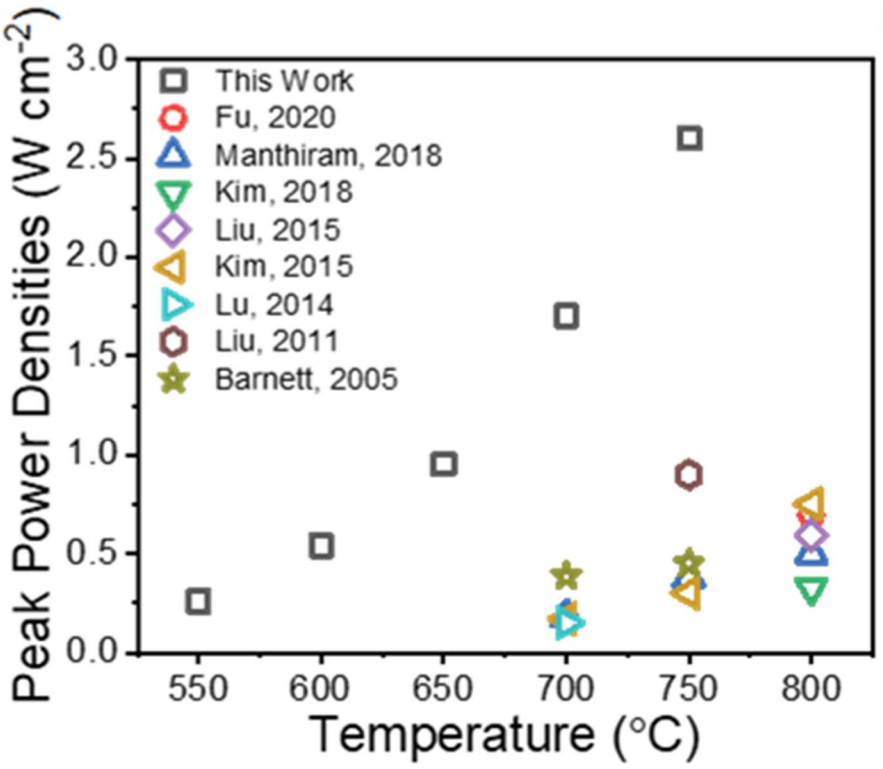

Figure 27. Comparison of our direct-C_3H_8 SOEC with literature results (Table A4).

3.5 Durability in fuel cell mode at intermediate operating temperatures

The durability of SOECs is crucial for reliable power generation. Li et al. has demonstrated SOECs equipped with PBSCF-a oxygen electrode, which achieves reversible and durable operation at a current density of 0.4 A cm^{-2} for 24 h [82]. In this work, we have conducted short-term stability testing of our SOEC in fuel cell mode with both H_2 and C_3H_8 fed to the fuel electrode (Figure 29-31). With humidified H_2 fed to the fuel electrode as the fuel, the SOEC achieves durable operation with negligible degradation at a current density of 0.8 A cm^{-2} and temperature of 650 °C (Figure 29). Additionally, the SOEC is durable at 550 °C, which validates the durability of our hybrid oxygen electrode at an intermediate operating temperature (Figure 30). Moreover, we also demonstrated its potential for utilizing alternative fuels (e.g., C_3H_8) for durable power generation, which is shown in Figure 31. The degradation rates are summarized in Table A7. Overall, the short-term stability testing conducted on SOECs with the hybrid electrode demonstrate its potential for durable power generation using multiple fuel streams.

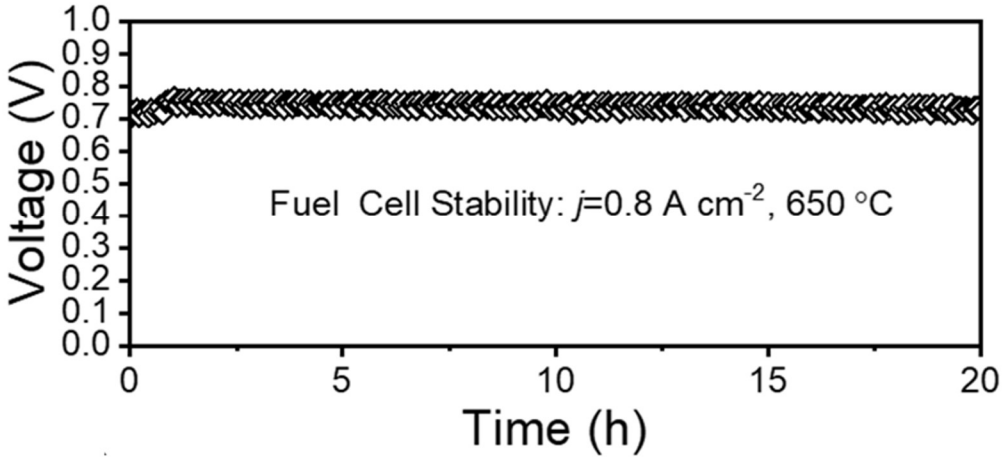

Figure 28. Durability testing of the SOEC equipped with the hybrid oxygen electrode in fuel cell mode at a current density of 0.8 A cm^{-2} and temperature of 650 °C with 3% humidified H_2 fed to the fuel electrode.

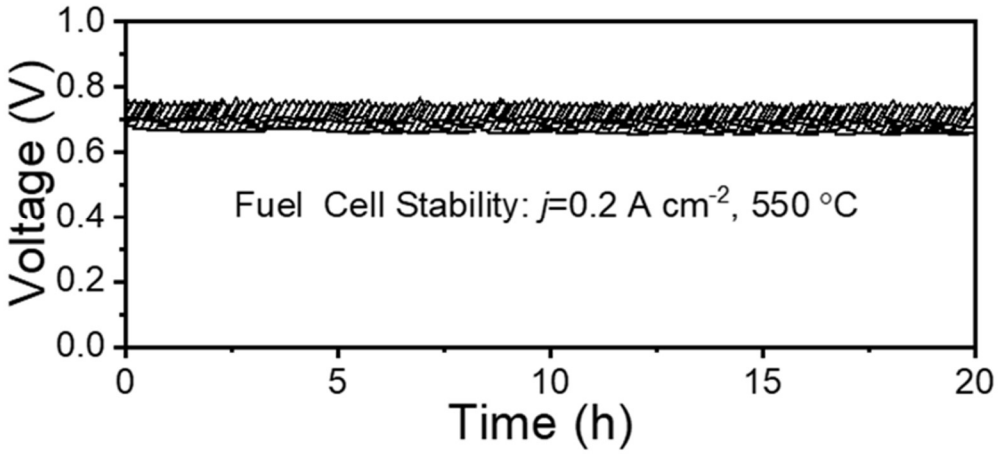

Figure 29. Durability testing of the SOEC equipped with the hybrid oxygen electrode in fuel cell mode at a current density of 0.2 A cm^{-2} and temperature of 550 °C with 3% humidified H_2 fed to the fuel electrode 0.2 A cm^{-2}.

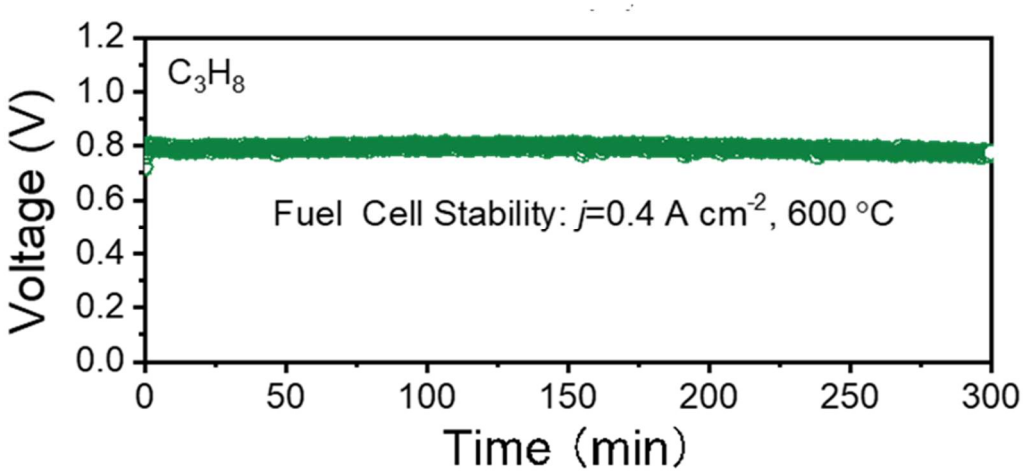

Figure 30. Durability testing of the SOEC equipped with the hybrid oxygen electrode in fuel cell mode at a current density of 0.4 A cm^{-2} and temperature of 600 °C with 3% humidified C_3H_8 fed to the fuel electrode.

3.6 SOECs equipped with the hybrid oxygen electrode attain a current density of 4.4 A cm^{-2} at 1.3 V and 750 °C, and good durability during the accelerated stability testing

Our SOECs equipped with the hybrid oxygen electrode also attain exceptional performance in steam electrolysis mode. Figure 32 shows the I-V curves of the SOEC in steam electrolysis mode at 550-750 °C. At 750 °C, a current density of 4.4 A cm^{-2} was achieved at 1.3 V, which is higher than the previously reported SOECs (Figure 10). Additionally, the SOECs demonstrated in this work also result in a cell-level H_2 production cost of 0.997 \$ kg^{-1} at a H_2 production rate of 0.0187 kg h^{-1} cm^{-2}, which represents the state of the art among of YSZ-based SOECs (Figure 9).

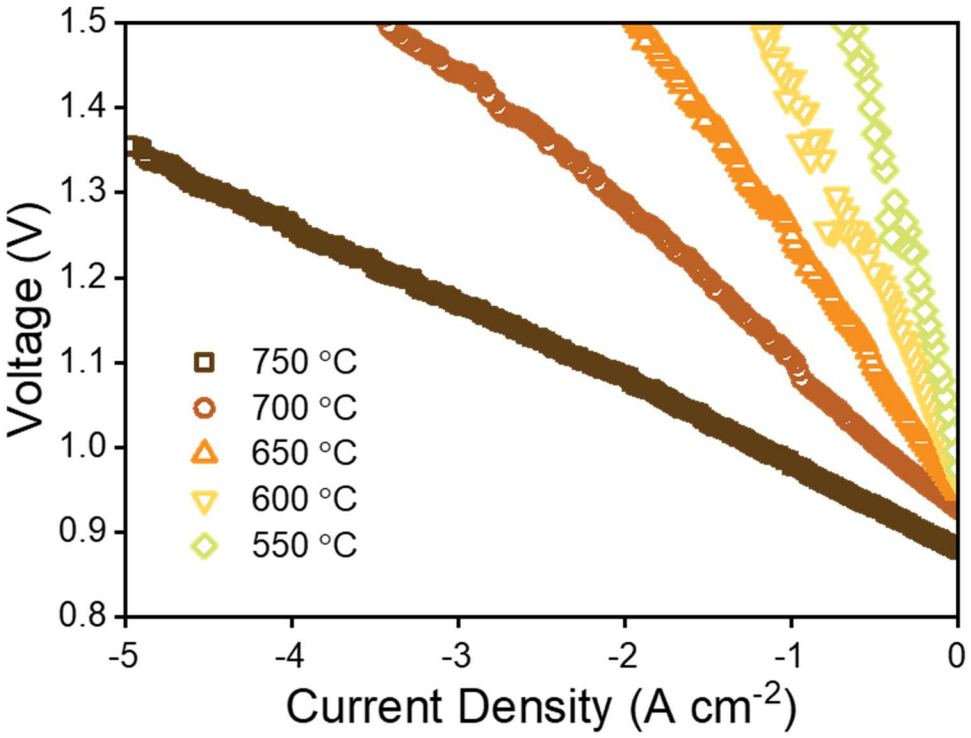

Figure 31. *I-V* curves of one representative SOEC with the hybrid oxygen electrode at different operating temperatures in steam electrolysis mode with 40% steam.

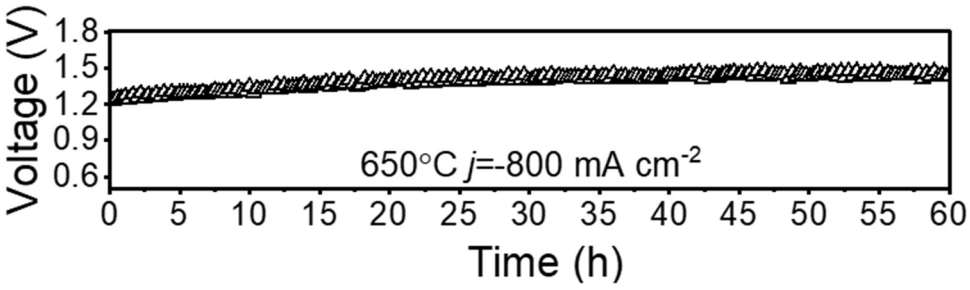

Figure 32. Durability testing of the SOEC at a current density of 0.8 A cm^{-2} and temperature of 650 °C in steam electrolysis mode with 40% steam.

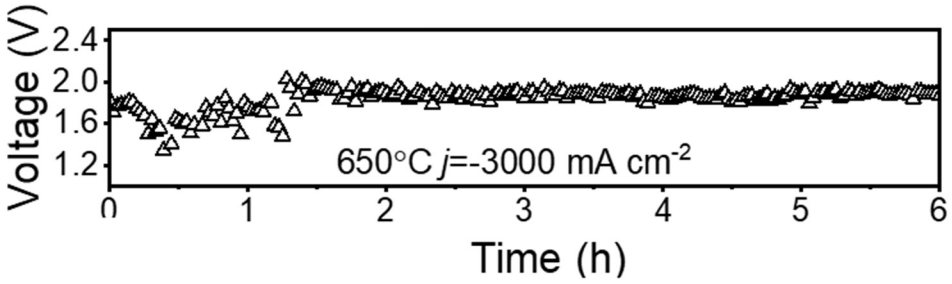

Figure 33. Accelerated stability testing of the SOEC at a high current density of 3.0 A cm^{-2} and temperature of 650 °C in steam electrolysis mode with 40% steam.

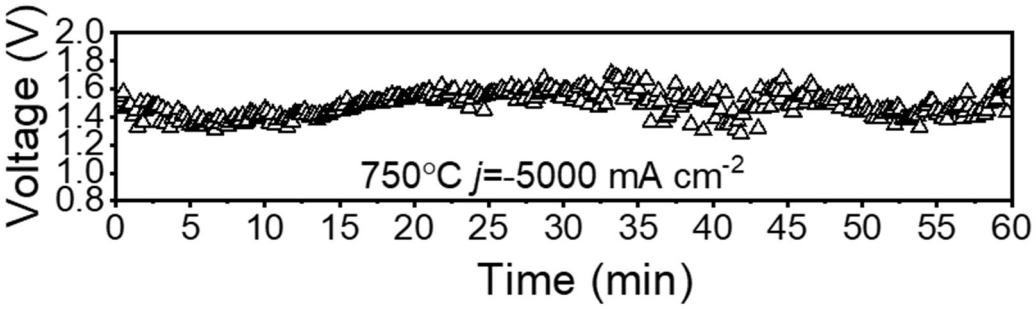

Figure 34. Accelerated stability testing of the SOEC at a high current density of 5.0 A cm^{-2} and temperature of 750 °C in steam electrolysis mode with 40% steam.

To validate the stability of employing these SOECs for reliable H_2 production, short-term stability was initially tested at 650 °C with a current density of 0.8 A cm^{-2}. The SOEC displays a minor degradation at the early stages and stable operation for the remaining 40 hours. To accelerate the evaluation of SOEC stability, we operated our SOECs under an extremely high

current density. For example, as shown in Figure 34, at 650 °C and a current density of 3.0 A cm^{-2}, the SOEC does not show degradation upon the accelerated stability testing. The second accelerated stability test was performed at 750 °C and a current density of 5.0 A cm^{-2}, which also indicates the SOECs equipped with the new hybrid electrode are stable (Figure 35). The degradation rates are summarized in Table A7, ranging from 3 mV h^{-1} to 4 mV min^{-1}, which are not eligible. Post-mortem characterizations were performed to evaluate the structural stability of SOECs. The SEM images shown in Figure A9 do not show any cracking or electrolyte-electrode delamination, implying the SOEC structure is robust under the harsh testing conditions.

3.7 Conclusion

In this work, we have successfully demonstrated a new hybrid oxygen electrode, which is composed of $Pr_{1.39}Ba_{0.14}Sr_{0.53}Co_{1.48}Fe_{0.76}O_{6-\delta}$ and $Ba_{0.66}Sr_{0.34}CoO_{3-\delta}$. This hybrid electrode significantly improves the surface oxygen exchange and bulk oxygen-ion diffusion coefficients, enhancing both oxygen reduction reaction and oxygen evolution reaction kinetics. Extensive characterization and analysis were performed to study this new electrode. The YSZ-based SOECs equipped with this novel hybrid electrode attain unprecedented performance for both power generation in fuel cell mode and green hydrogen production in steam electrolysis mode. At 750 °C, a peak power density of 2.4 W cm^{-2} was achieved using H_2 as the fuel. With propane fed to the fuel electrode, a peak power density of 2.6 W cm^{-2} was attained, representing the record in this field. In steam electrolysis mode, a current density of 4.4 A cm^{-2} was demonstrated at 1.3 V and 750 °C, which outperforms all previously reported YSZ-based SOECs. This achievement leads to a cell-level hydrogen production cost of 0.997 \$ kg^{-1} at a H_2 production rate of 0.0187 kg h^{-1} cm^{-2}, which approaches the DOE H_2 production cost target (<\$1 kg^{-1}).

Additionally, accelerated stability testing was performed in steam electrolysis mode under extremely high current densities (5.0 A cm^{-2}), validating the stability of the SOECs equipped with the newly developed hybrid electrode are stable. These promising results highlight that the PBSCF-b+BSC hybrid electrode could serve as the next-generation oxygen electrode of high-performance SOECs.

Chapter 4 - Tuning the *in situ* exsolution of Ni-Co alloy nanoparticles on doped ceria for improved performance in CO_2 electrolysis

4.1 Introduction to CO_2 SOECs

When it comes to CO_2 emissions, there is a consensus that it is a serious challenge due to the steady increase of fossil fuels usage and the resultant impact on climate change. To address this and establish a sustainable ecosystem, considerable emphasis has been placed on renewable energy sources as a viable alternative to meet global energy demands [39]. Nonetheless, their intermittent nature necessitates the storage of harvested energy in the form of chemicals, such as CO, an industrial gas with a wide range of applications. When driven by solar or wind power, the electrochemical reduction of CO_2 to CO process can combine the conversion of environmental CO_2 and the storage and utilization of sustainable energy.

Numerous electrochemical technologies have been proposed for CO_2 reduction, with low-temperature electrolysis and SOECs emerging as two primary areas of focus [83]. A commonly known constraint with low-temperature CO_2 electrolysis conducted in aqueous solutions is the low solubility of CO_2 (33 mM at 1 atm and 25 °C) [51,84]. In contrast, SOECs that operate at elevated temperature (600-800 °C) have garnered attention for their near-unit Faradaic efficiency, high energy densities and bifunctionality, enabling them to operate interchangeably between SOFCs and SOECs.

Most studies in the field of SOECs naturally center on the cathode, where the rate-limiting steps take place [85–89]. Among the most widely employed cathodes in SOECs, nickel/yttria stabilized zirconia (Ni/YSZ) possesses exceptional electronic and ionic

conductivity, exhibits high electrocatalytic performance towards CO_2 reduction and is cost efficient. However, it suffers from issues like unstable redox behavior and nickel coarsening during operation. Various alternative materials, including perovskite materials such as $Sr_2Fe_{1.5}Mo_{0.5}O_{6-\delta}$, $La_{0.75}Sr_{0.25}Cr_{0.5}Mn_{0.5}O_{3-\delta}$, and $La_{0.2}Sr_{0.8}TiO_{3+\delta}$ [83,90–96], have been proposed which demonstrated resistance towards carbon deposition and redox stability during CO_2 reduction. Nonetheless, the electrochemical performance of these cathodes needs to be further improved for practical applications. Ceria-based oxides represent another class of very promising cathode materials for CO_2 SOEC, attributed to their stable cubic fluorite structure, and mixed ionic and electronic conductivity in a CO-CO_2 atmosphere [97–100]. Moreover, it has been demonstrated by Skafte et al. [101] using operando ambient-pressure X-ray photoelectron spectroscopy (APXPS) that in a surface reverse Boudouard reaction, the abundant carbonates on ceria could react with transiently deposited carbon, preventing carbon build-up.

The electrochemical reduction of CO_2 to CO can be expressed in equation (4.1) when ceria-based oxides are involved [102,103]:

$$CO_{2(g)} + V_O^{\bullet\bullet} + 2Ce'_{Ce} \leftrightarrow CO_{(g)} + O_O^X + 2Ce_{Ce}^X \tag{4.1}$$

where Ce'_{Ce} represents the Ce^{3+} cations and $Ce^{\times}_{Ce}$ represents the Ce^{4+} cations. And some in-depth studies have been done to probe the mechanism of this reaction and the rate-limiting steps [103–105]. Feng et al. [103] used operando APXPS to analyze the correlation between the concentration of surface Ce^{3+}, the carbonate intermediate coverage and the cathodic overpotential, and proposed that the process where the surface Ce^{3+} localized electrons are transferred per carbonate formation is likely the rate-limiting step. Another investigation conducted by Zhao et al. [104] also explored the vital role of surface Ce^{3+} localized electrons and oxygen vacancies. Instead of conceptually dividing the surface reaction into two single-electron

transfer steps which was adopted by Feng et al. [103], Zhao et al. [104] proposed a model wherein the CO_2 splitting mechanism involves CO_2 activation over surface defects followed by the charge transfer process, and the latter was found to be rate-limiting.

The in situ exsolution approach of metallic nanoparticles, achieved through doping of transition metals such as Ni, Co, Fe followed by a reduction treatment, has been widely employed by many researchers to enhance the electrocatalytic capabilities of cathode material [106–109]. In this process, catalytically active metal nanoparticles and oxygen vacancies are generated simultaneously, both of which have been recognized by many as the key factors for CO_2 reduction [101,110–112]. In a reducing atmosphere, ferrate double perovskites have the tendency towards compositional transformation which leads to decrease of its ionic conductivity, while ceria materials hold the cubic fluorite structure stably in a wide range of conditions [102,106,113]. Jiang et al. [99] recently found Fe-exsolved ceria to be a highly efficient cathode for CO_2 SOEC. With Fe partially reduced, exsolved Fe^0 nanoparticles are anchored on the ceria surface and a fair amount of oxidant Fe stays in the ceria lattice. Furthermore, Ye et al. [114] used density functional theory (DFT) methods to study the effects of Fe exsolution, and found that Fe-O-Ce facilitates the formation of Ce^{3+}-Ce^{4+} and the CO_2 dissociation and CO desorption barriers are lowered in the presence of Fe-exsolved ceria.

Herein, we report a cathode material where in situ exsolved Ni-Co alloy nanoparticles on SDC surface greatly improved the performance of SOECs. The doping ratio of Ni-Co was optimized between 15% to 30% and its effect on physicochemical properties and electrochemical performance was systemically studied. Furthermore, we found that the synergetic effect of Ni-Co alloy plays a vital role in enhancing the performance of our SOECs when compared to single metallic dopant, i.e., Ni or Co. Equipped with the optimized cathode material, SDC doped with

25% Ni-Co (SDCNiCo25), a superior current density of 2.7 A cm^{-2} was achieved at 750 °C, 1.5 V.

4.2 Structural characteristics of SDCNiCo15-30, SDCNi, and SDCCo

To investigate the impact of varying Ni and Co doping percentages on the chemical and physical characteristics, as well as the electrochemical performance of our catalysts, a series of SDCNiCo samples was synthesized, encompassing doping percentage ranging from 15% to 30%. The detailed procedural steps are outlined in the methods section above. Figure 36 shows XRD patterns of the as-prepared SDCNiCo15-30 powder and the powder after reduction treatment under 15% H_2/Ar at 650 °C for 2 h. Irrespective of the doping percentages, all samples exhibited consistent patterns, with one phase corresponding to the cubic fluorite SDC [115], and the other to cubic $NiCoO_2$ [116]. Similarly, the samples after reduction also displayed consistent patterns, attributable to the SDC phase and NiCo alloy.

Catalysts with a monometallic doping design were also synthesized to gain a better understanding of the synergistic effects of Ni and Co, as detailed in the experimental section. And as illustrated in Figure 37, the XRD patterns of SDCNiCo25. SDCNi25 and SDCCo25 before and after reduction exhibit similar trends. The SDC phase remained stable under reducing conditions [117,118], while $NiCoO_2$, NiO, and Co_3O_4 were reduced to metallic phases respectively.

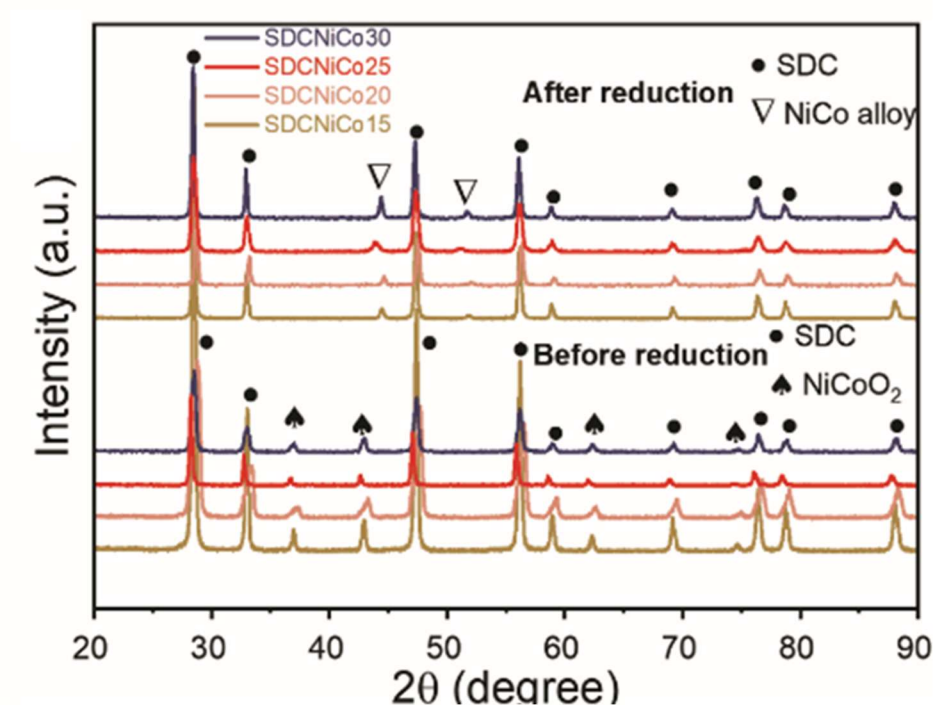

Figure 35. XRD patterns of SDCNiCo15-30 before and after reduction treatment under 15% H_2/Ar at 650 °C for 2 h.

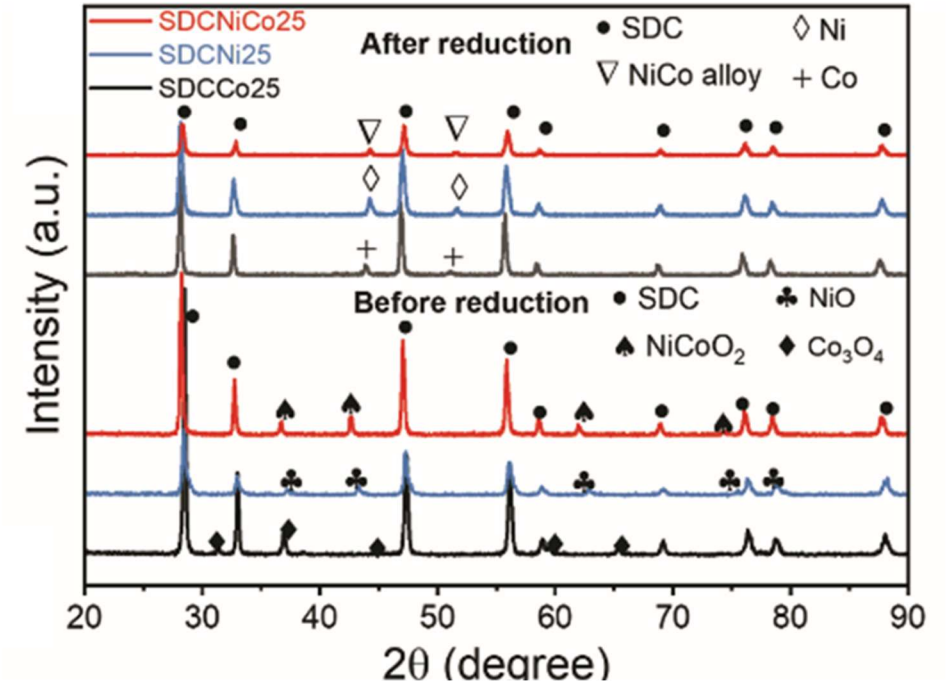

Figure 36. XRD patterns of SDCNiCo25, SDCNi, and SDCCo before and after reduction treatment under 15% H_2/Ar at 650 °C for 2 h.

To further verify the presence of NiCo alloy in the SDCNiCo25 sample and characterize the structure and composition of the hybrid catalyst, high resolution TEM (HR-TEM) was employed, as shown in Figure 39. The results revealed that the lattice spacing of the support is 0.312 nm, corresponding to the (111) plane of SDC. In contrast, the lattice space of the metallic phases is 0.197 nm, indexed to the (111) plane of the NiCo alloy. Additionally, Figure 38 presents EDX analysis, confirming the highly identical distribution of Ni and Co elements. Furthermore, a quantitative analysis of the elemental ratios of NiCo alloy was carried out, as shown in Figure 40, indicating that the average weight ratio of Ni and Co is roughly equal.

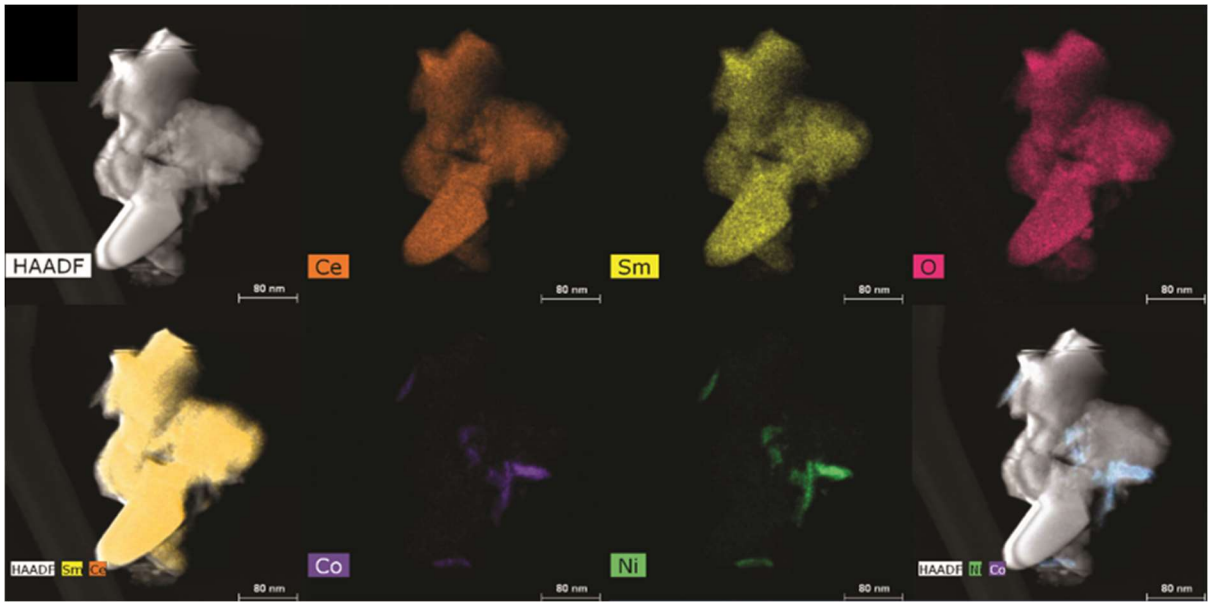

Figure 37. TEM image and elemental maps of SDCNiCo25 sample after reduction.

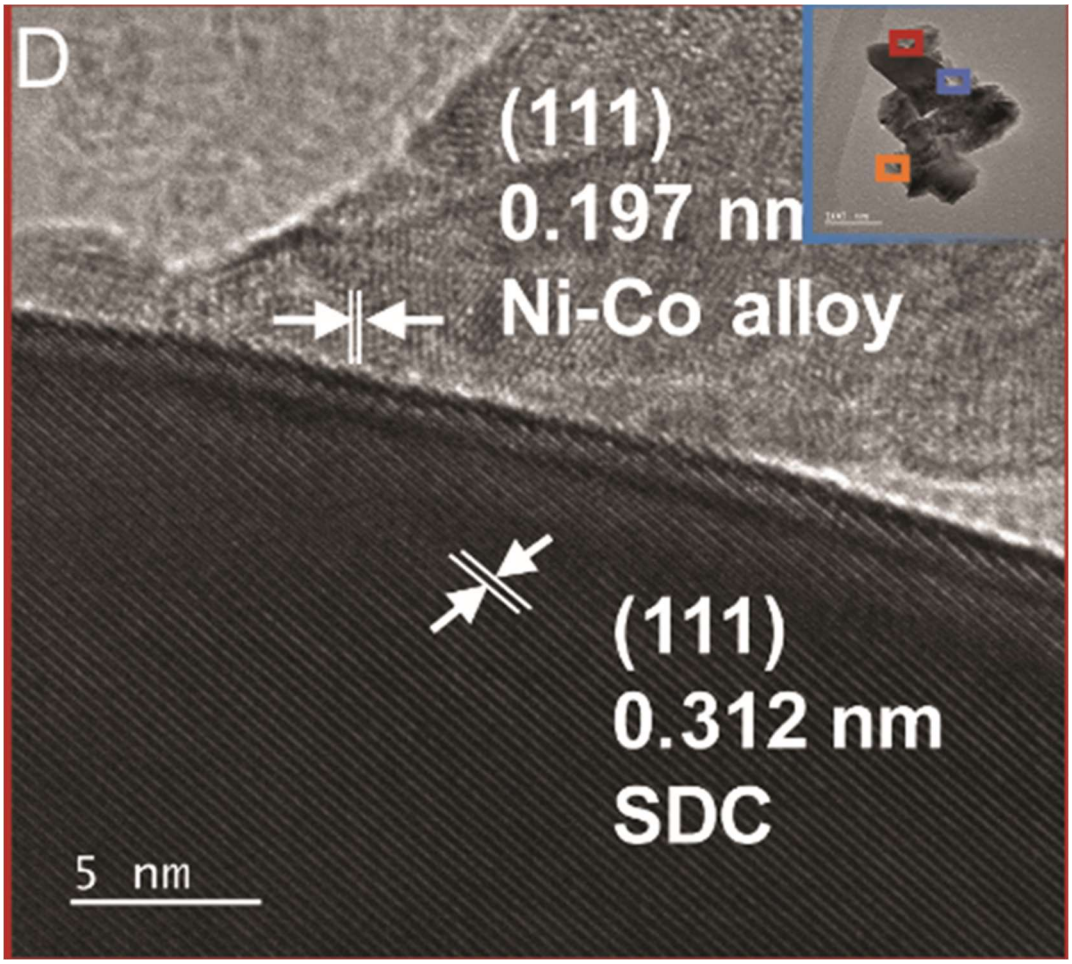

Figure 38. HR-TEM images of SDCNiCo25 sample after reduction.

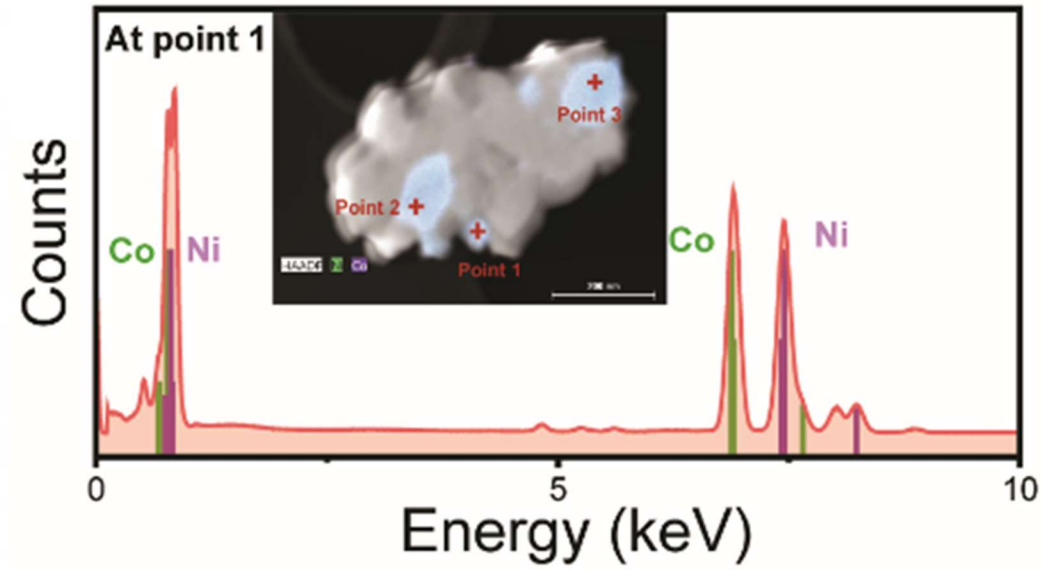

Element	Point 1 [wt. %]	Point 2 [wt. %]	Point 3 [wt. %]	Average [wt. %]
Co	51.4	48.0	48.6	49.3
Ni	48.6	52.0	51.4	50.7

Figure 39. Quantitative analysis of the elemental ratios of three points where the NiCo alloy presents.

TPR profiles of the SDCNiCo15-30 samples are shown in Figure 41. All four samples share the same features of two peaks from around 420 °C to 580 °C, which could be attributed to the reduction of Ni^{2+} and Co^{2+} in $NiCoO_2$ [119]. As expected, the peak areas tended to increase with an increasing metallic doping percentage, while the peak positions remained consistent.

And the reducible properties of SDCNiCo25, SDCNi25, and SDCCo25 were also investigated, shown in Figure 42. There were two well-defined reduction peaks in SDCNi25, which correspond to stepwise reduction of NiO to metallic Ni. The peak around 415 °C represents the reduction of NiO with a smaller particle size and the one around 507 °C represents the same process but for bigger particle size [120,121]. In contrast, the reduction of SDCCo only yielded one peak, corresponding to the reduction of Co_3O_4 to metallic Co.

The adsorption behaviors of SDCNiCo25, SDCNi25, and SDCCo25 were also investigated since it is of importance to the CO_2 reduction reaction occurring on the surface of electrode materials. As shown in Figure 43, the desorption behavior begins at 100 °C, associated with the physical desorption of CO_2 due to the weak van der Waals forces [113,122]. The CO_2 desorption at the higher temperature range (425-750 °C) is ascribed to moderately and strongly bonded species. Since a larger desorption area and an increased desorption temperature indicate stronger adsorption ability of CO_2 [108,123,124], the adsorption capability of SDCNiCo25 is superior when compared to its monometallic doped counterparts.

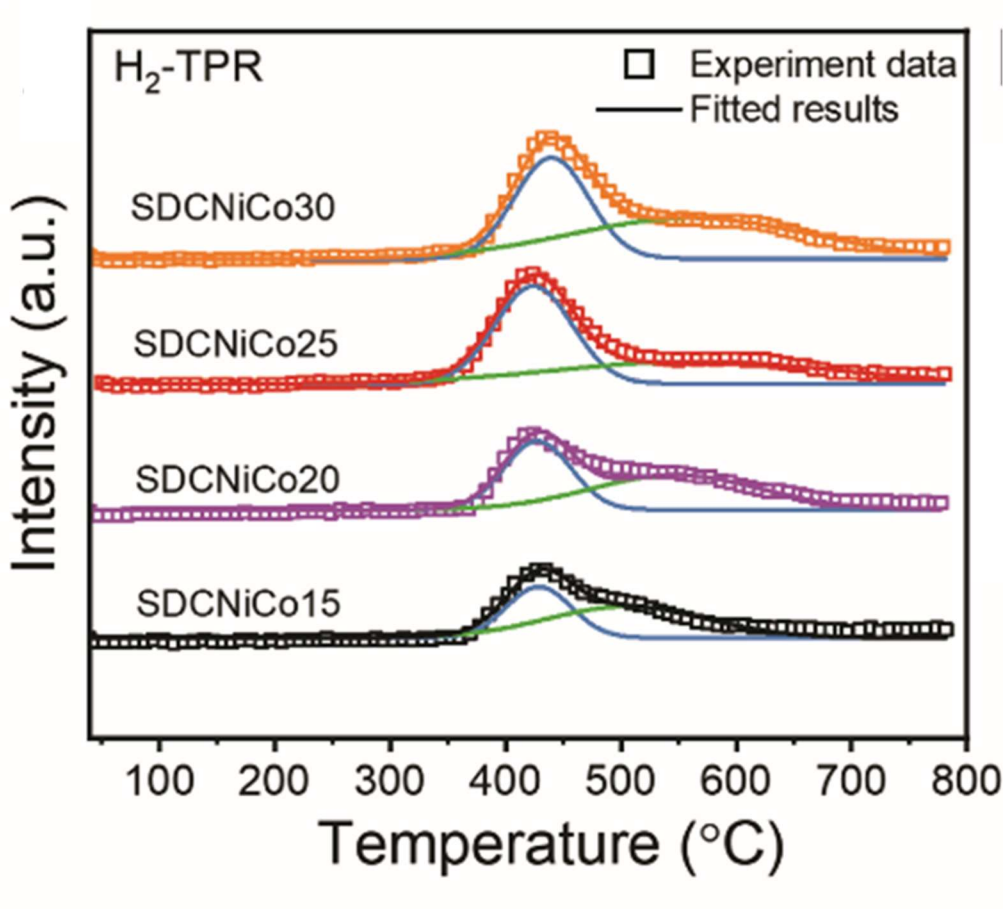

Figure 40. H_2-TPR curves of the SDCNiCo15-30 samples.

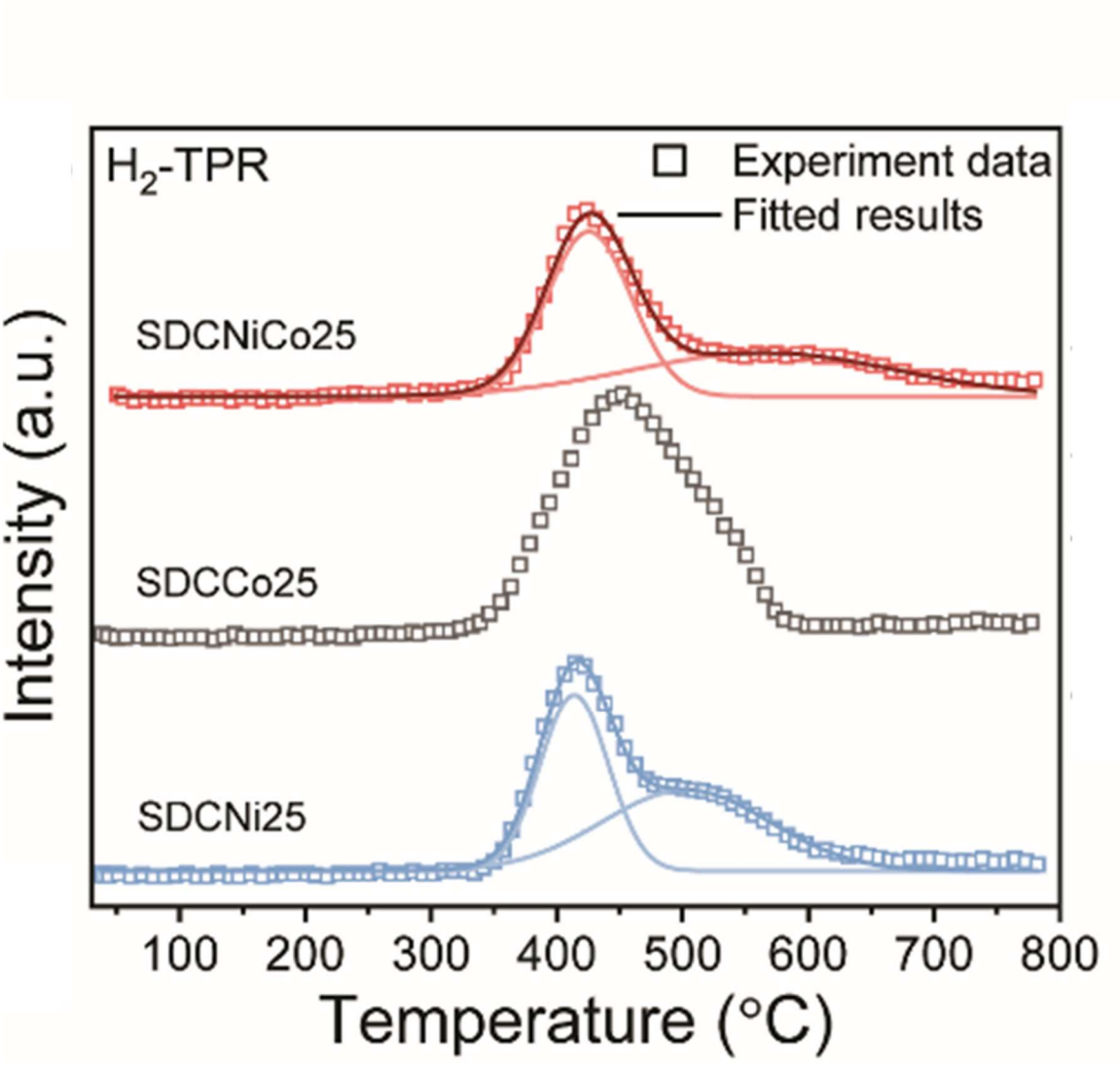

Figure 41. H_2-TPR curves of the SDCNiCo25, SDCNi, and SDCCo samples.

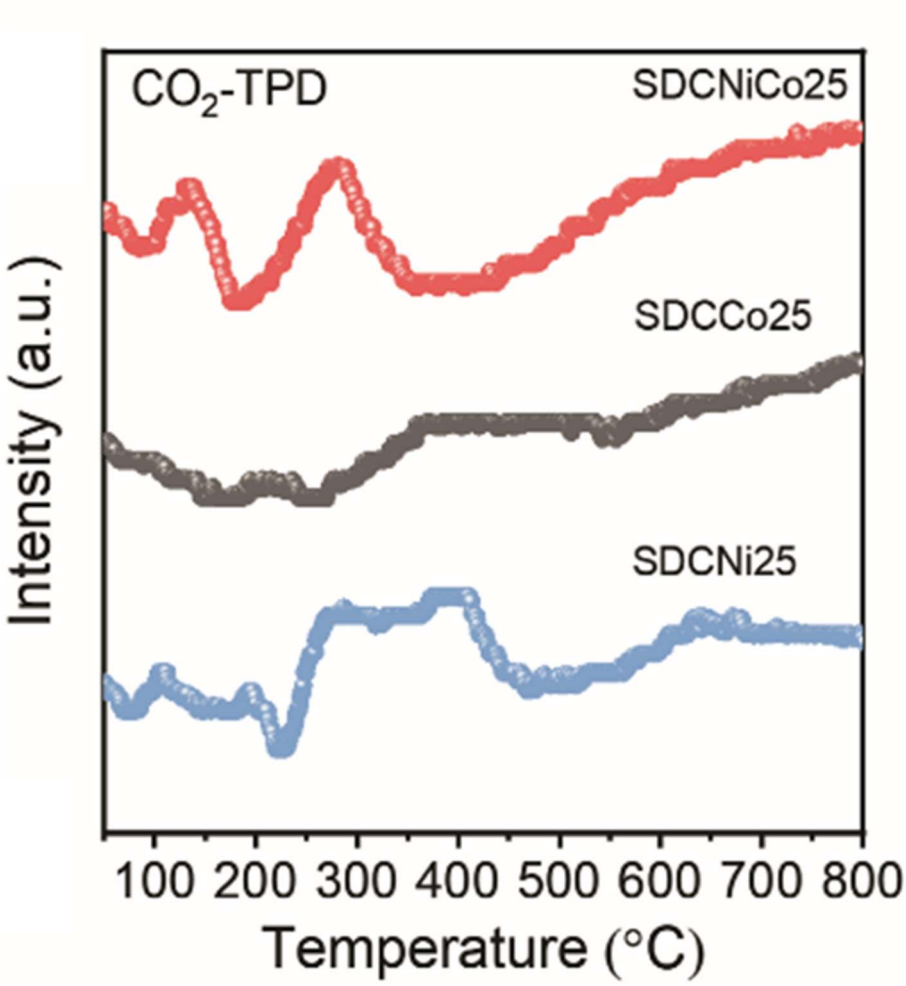

Figure 42. CO_2-TPD curves of the SDCNiCo25, SDCNi, and SDCCo samples.

4.3 Tuning the Ni and Co doping percentage to achieve superior electrochemical performance.

For the assessment of electrochemical performance, we fabricated LSGM electrolyte supported single cells with the configuration of fuel electrode|LSGM|PBSCF-BSC. The fuel electrodes, featuring in situ exsolved alloy, were prepared through reduction treatment with hydrogen gas at 750 °C for 15 minutes prior to the testing.

Figure 44 illustrates the current-voltage (I-V) curves of SOECs with four different fuel electrodes (SDCNiCo15-30) at applied voltages of 0.8 to 1.6 V at 750 °C. The SOEC equipped with SDCNiCo25 fuel electrode exhibited higher current densities compared to those with SDCNiCo15, SDCNiCo20, or SDCNiCo30. Particularly, at higher applied voltage (> 1.4 V), evident mass transport limitations were observed during the charging process for SDCNiCo15, and SDCNiCo20. The CO_2 reduction reactions (CO_2RR) in the fuel electrodes during SOEC operation involve several sub-processes [106,107,125]: (1) adsorption and diffusion of CO_2 molecules onto the active sites located on the surface of fuel electrodes, (2) the surface reaction kinetics leading to CO and O^{2-} production, and (3) charge transfer from the fuel electrode bulk through the interface of electrode and electrolyte. In the case of SDCNiCo15 and SDCNiCo20, poor CO_2 adsorption led to the starvation of reactants on the active sites at >1.4 V, resulting in compromised electrochemical performance. As shown in Figure B1 and B2, this phenomenon became more pronounced with increasing operating temperatures from 650 °C to 750 °C, consistent with the CO_2 TPD results. Conversely, fuel electrodes with higher Ni and Co doping percentages, namely, SDCNiCo25 and SDCNiCo30, did not exhibit evident mass transport limitations.

Electrolysis current densities at the thermoneutral potential (~1.5 V) for CO_2 SOEC were compared across temperatures from 750 °C to 650 °C (Figure 45). SDCNiCo25 demonstrated the highest current densities among the four electrode materials, measuring 2.70, 1.34, and 0.46 A cm^{-2} at 750 °C, 700 °C and 650 °C, respectively. At 750 °C, it was 385% higher than that of SDCNiCo15.

To further comprehend the impact of doping percentage on CO_2RR performance, EIS data were collected under OCV conditions from 750 °C to 650 °C. Results for SDCNiCo15, SDCNiCo20, and SDCNiCo30 are presented in Figure B2-B4. The intercept of the semicircle in high frequency represented the ohmic area specific resistance (ASR_o), while the polarization area specific resistance (ASR_p) was the difference between the two intercepts of high and low frequency. The ohmic resistance values were similar across cells due to identical electrolytes and air electrodes. For instance, ASR_o varies from 0.11 to 0.24 Ω cm^2, while ASR_p varies from 0.14 to 0.61 Ω cm^2 at 750 °C. Given the much smaller variance in ASR_o (0.13 Ω cm^2) compared to ASR_p (0.47 Ω cm^2), we can infer that the difference in polarization resistances is the major contributor. In Figure 46, ASR_o is subtracted for a more direct comparison of polarization resistances under OCV conditions.

Figure 47 presents the Arrhenius plots of polarization resistances for the four electrode materials as a function of inverse temperature. The results indicate that SDCNiCo25 material exhibited significantly enhanced CO_2RR activity compared to the other three at all measured temperatures. For instance, at 750 °C, ASR_p of the SDCNiCo25 (0.14 Ω cm^2) in CO_2/CO = 90/10 was ~240%-430% lower than those of SDCNiCo15, SDCNiCo20, and SDCNiCo30.

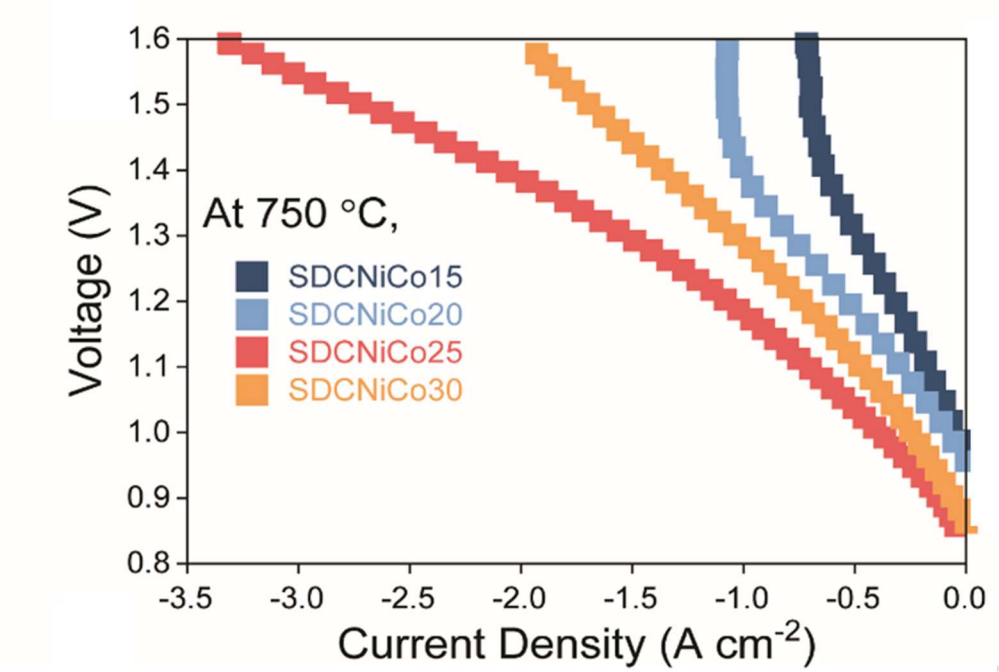

Figure 43. I-V curves of SDCNiCo15-30 at 750 °C.

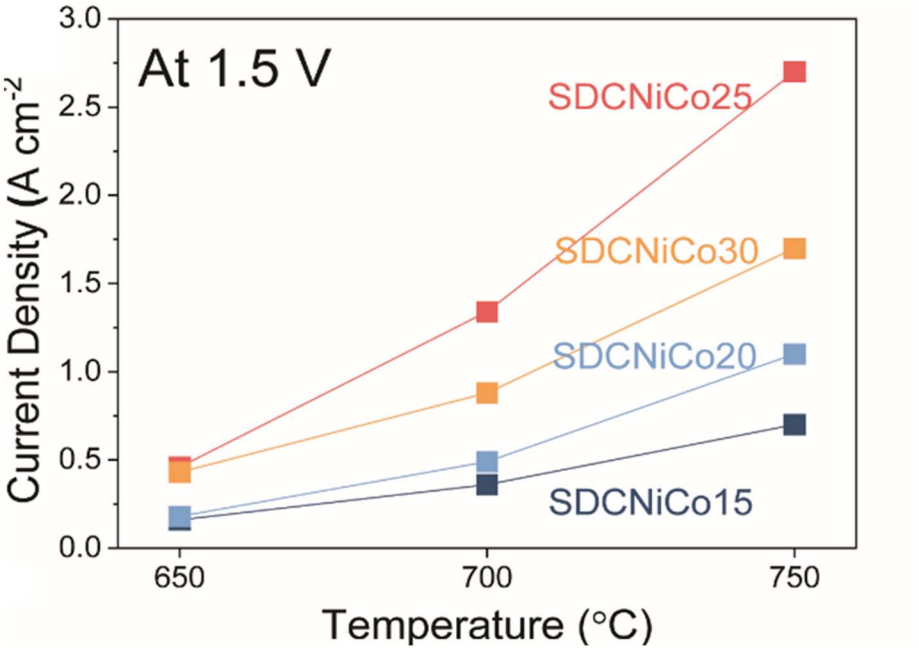

Figure 44. Current densities of SDCNiCo15-30 at 1.5 V, 750-650 °C.

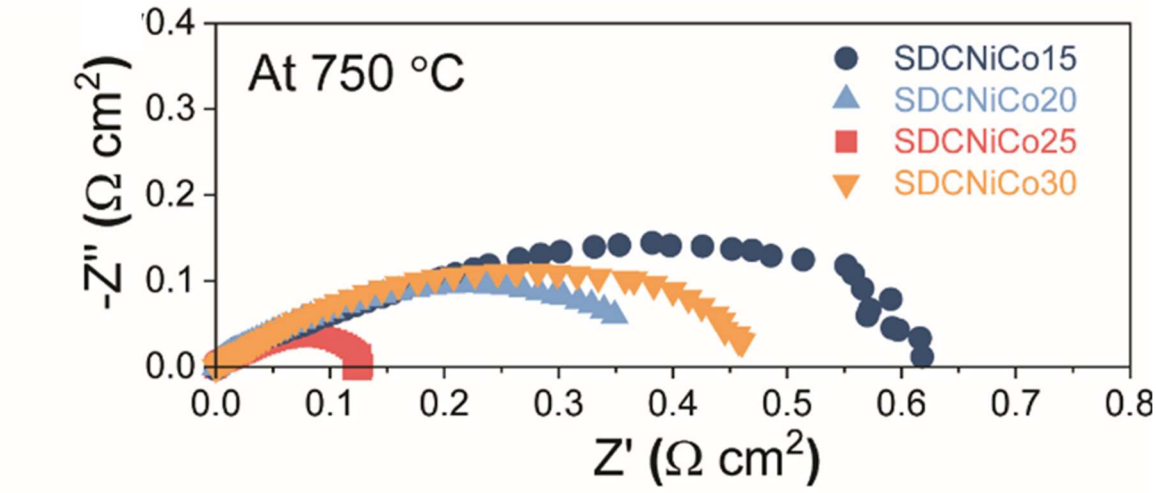

Figure 45. Nyquist plots at 750 °C, OCV condition, with ASR_o subtracted.

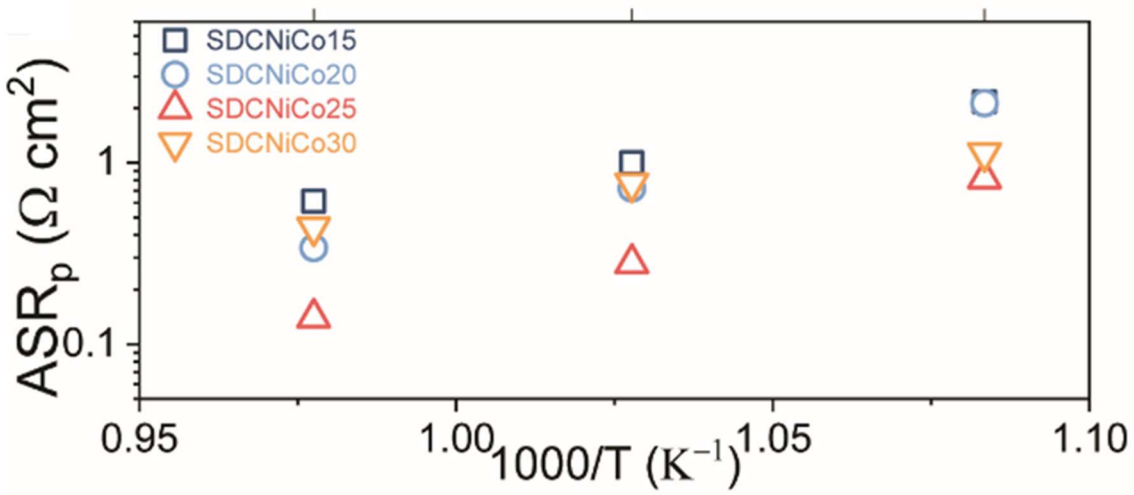

Figure 46. Arrhenius plots for ASR_p of SDCNiCo15-30.

4.4 Synergistic effects of NiCo alloy on CO_2RR activity enhancement.

After confirming the existence of NiCo alloy in SDCNiCo25, we further demonstrated the synergistic effect the Ni and Co in the composite electrode on CO_2RR activity by comparison of SOECs with SDCNiCo25, SDCNi25, SDCCo25. Figure 48 and 49 evidently present that the SDCNiCo25 shows better electrocatalytic activity than the SDCNi25 or SDCCo25 for SOEC. Like SDCNiCo15 and SDCNiCo20, SDCCo also experienced mass transfer limitation when working potential reached 1.4 V, and it can also be attributed to the poor adsorption ability of CO_2, as demonstrated in CO_2-TPD. Furthermore, the change in the slope of I-V curves for SDCNiCo25 is more significant with increasing cell voltage, corresponding to the decreasing polarization resistance at higher potentials which contribute to the higher performance at higher applied voltage.

In Figure 50, the Arrhenius plots of polarization resistances at 1.5 V were presented for the three electrode materials. It is obvious that the activation energy for SDCNiCo25 is higher than that of SDCNi25 or SCDCo25, which may put it in disadvantage when operating at lower temperatures. But it also leads to superior performance at intermediate temperature range.

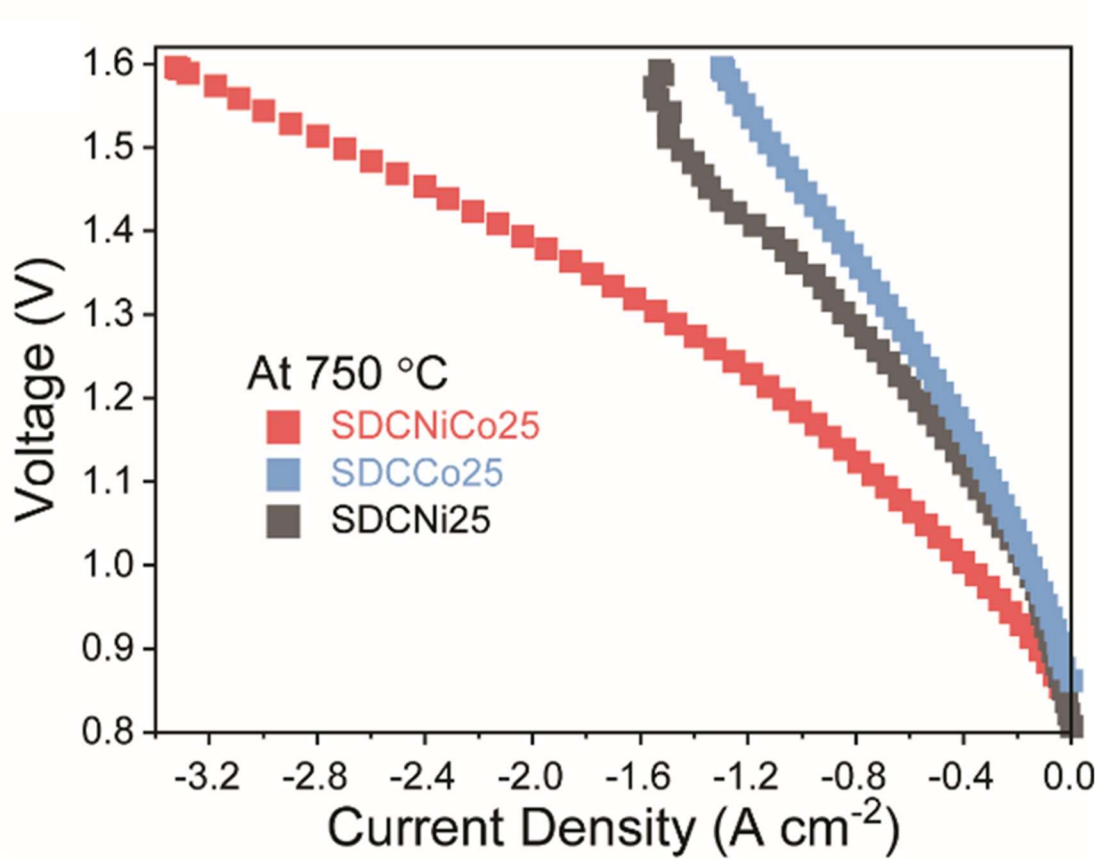

Figure 47. I-V curves of SDCNiCo25, SDCNi25, and SDCCo25 at 750 °C.

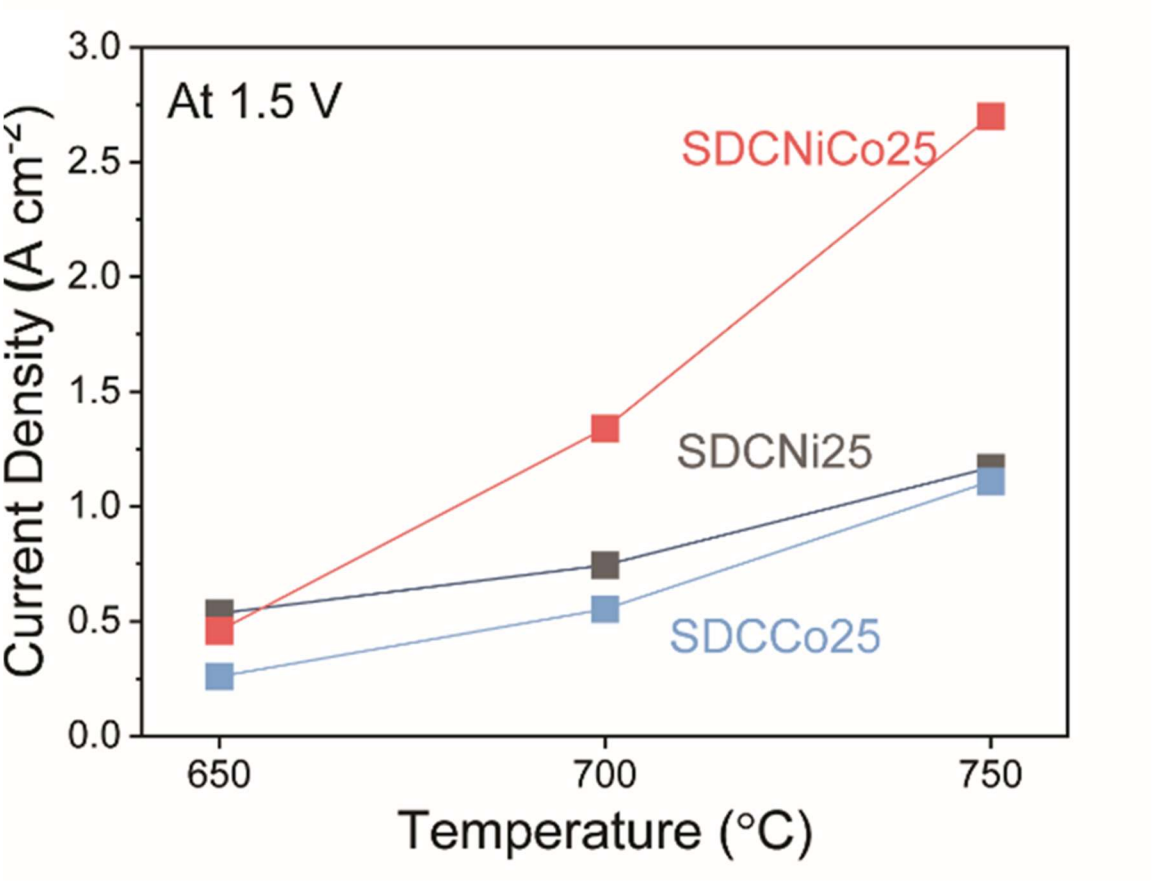

Figure 48. Current densities of SDCNiCo25, SDCNi25, and SDCCo25 at 1.5 V, 750-650 °C.

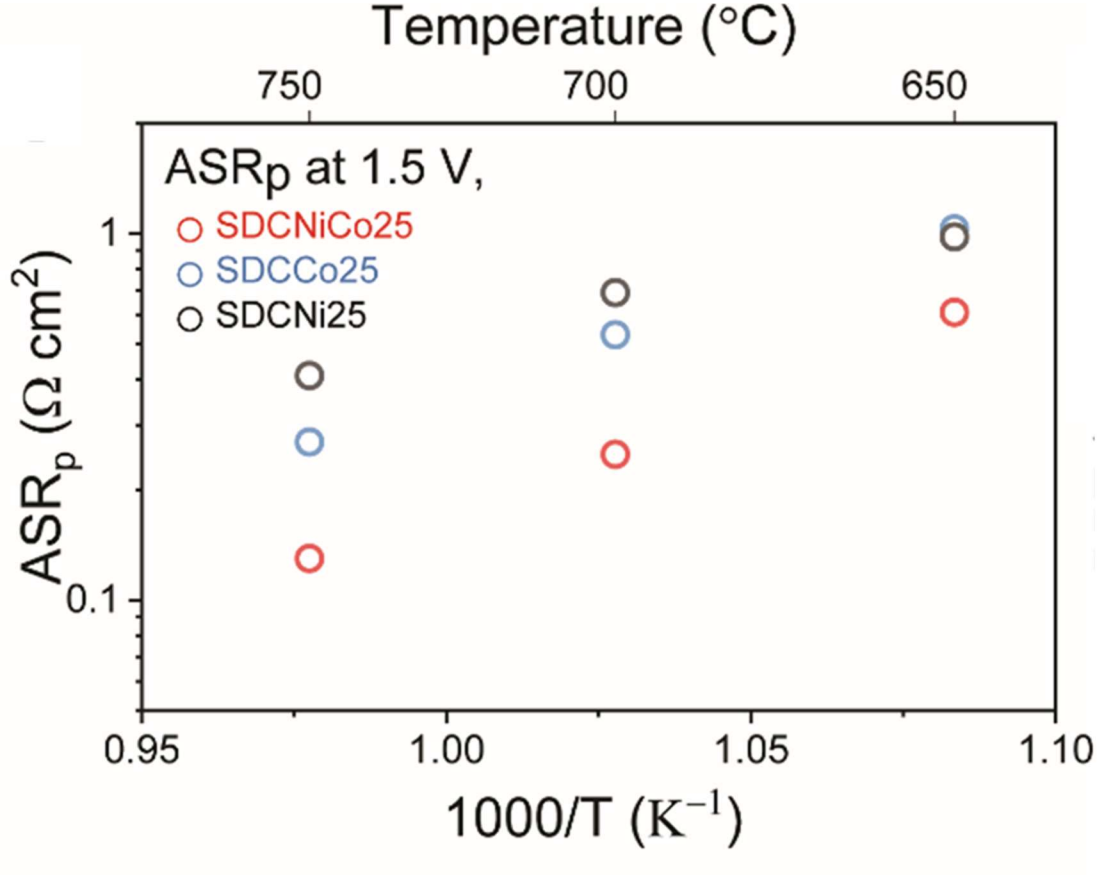

Figure 49. Arrhenius plots for ASR_p at 1.5 V at 750 °C, 1.5 V of SDCNiCo25, SDCNi25, and SDCCo25.

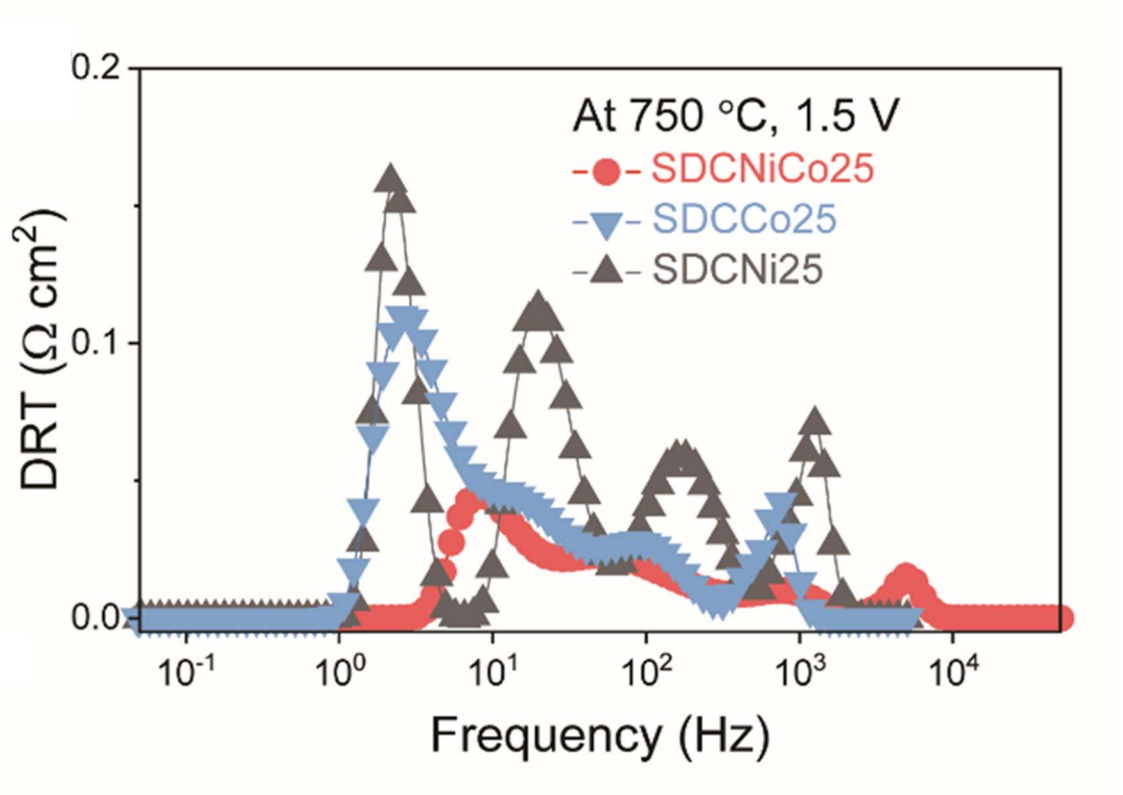

Figure 50. DRT plots at 750 °C, 1.5 V of SDCNiCo25, SDCNi25, and SDCCo25.

To better understand the electrocatalytic effects of NiCo alloy, we employed the distribution function of relaxation times (DRT) analysis which could help distinguish the elementary electrode processes in Nyquist plots. As shown in Figure 51, four response peaks, labeled P1, P2, P3, and P4 can correspond to different electrode processes. And with the integral area of each characteristic peak corresponding to the resistance value, peaks with bigger areas represent sub-processes with higher resistance. Based on the Adler-Lane-Steele model and literature reported in recent years, P4 is related to the electrochemical surface reactions, P3 is attributed to the CO_2 adsorption process on the fuel electrode surface, P2 is ascribed to the oxygen ion transfer process in the electrodes, and P1 is attributed to the oxygen ion transportation process across the electrode-electrolyte interface. It is obvious that the process related to P4 is the rate-limiting step, and NiCo alloy accelerates this process dramatically according to the decreased peak area. As for P3, SDCNi25 exhibits the largest area out of these three materials, which is in good agreement with the CO_2-TPD results, which suggests that SDCNi25 possesses poor CO_2 adsorption ability.

4.5 Electrochemical performance of SDCNiCo25 in CO_2 SOEC and H_2 SOFC.

Figure 52 shows the temperature dependent performance of electrolyte-supported single cell with the SDCNiCo25 composite electrode with dry hydrogen and ambient air supplied to fuel electrode and air electrode, respectively. The OCVs were 1.23, 1.25, and 1.26 V, at 750 °C, 700 °C, and 650 °C, respectively. These values are close to the theoretical values calculated from the Nernst equation, suggesting that sealing was airtight and no gas leakage was present during the testing. Compared to the cell performance of SDCNi25 and SDCCo25 presented in Figure B4 and B5, the PPDs experienced improvement with SDCNiCo25 electrode. The PPDs were 1.53, 1.00, 0.63 W cm^{-2}, at 750 °C, 700 °C, and 650 °C, respectively for SDCNiCo25, which is ~128%-233% higher than those of SDCNi25. Furthermore, the cell performance is among the highest when compared to other LSGM electrolyte-supported SOFCs developed in recent years.

As shown in Figure 53, the I-V curves and Nyquist plots of the SOEC with SDCNiCo25 electrode under CO_2/CO = 90/10 present enhanced electrochemical performance. At thermoneutral voltage and 750 °C, the ASR_o and ASR_p was just 0.09 and 0.13 Ω cm^2. The corresponding current density, 2.7 A cm^{-2}, is much higher than those of SOECs with other fuel electrodes under similar operating conditions. The excellent performance is originated from both the ceria-based fluorite structure which promotes formation of oxygen vacancies, and the electrocatalytic activity of NiCo alloy and its boost on the adsorption/dissociation of CO_2 reactants.

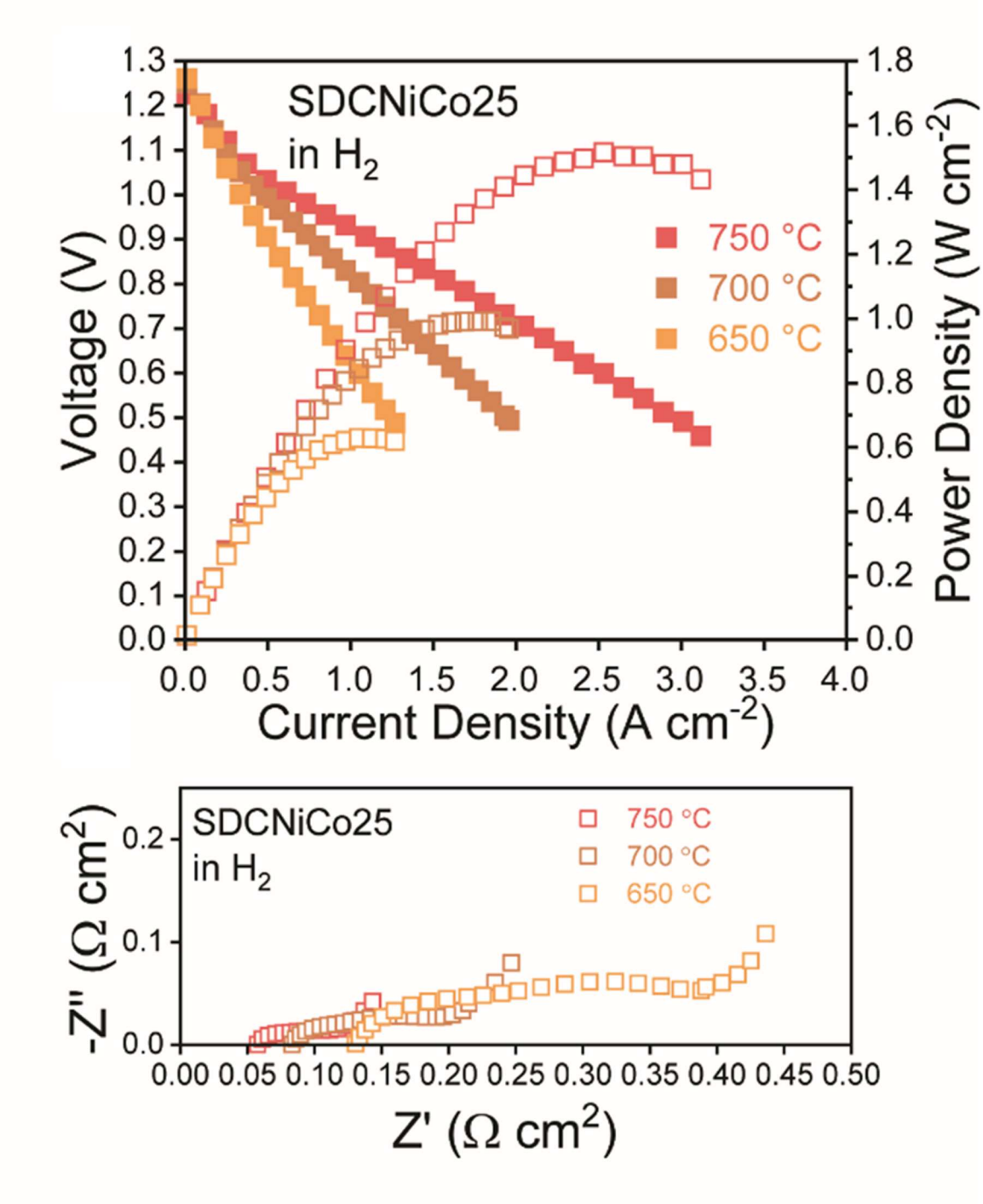

Figure 51. I-V-P curves and corresponding Nyquist plots under OCV of SDCNiCo25 in dry hydrogen under SOFC mode.

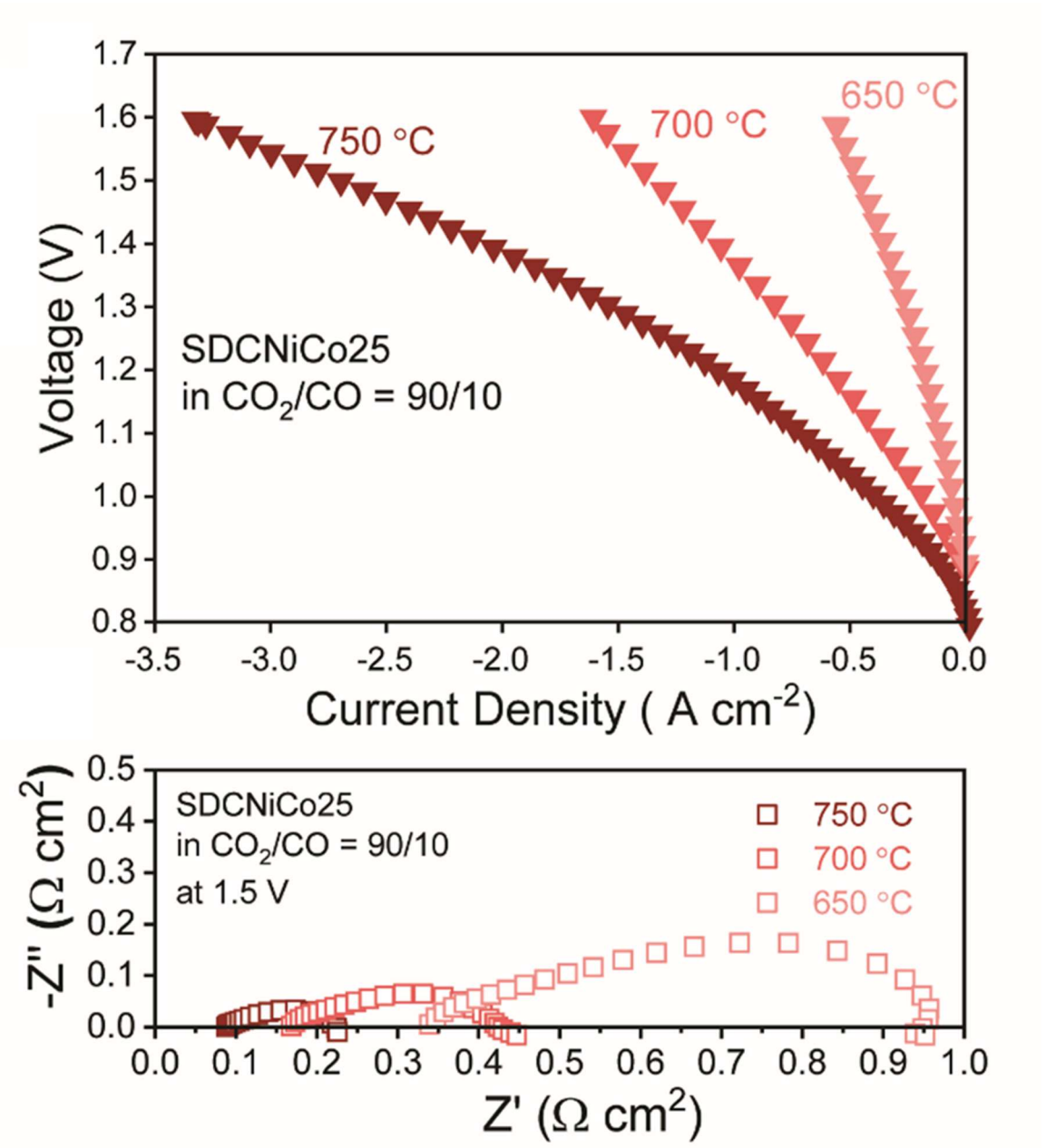

Figure 52. I-V curves and corresponding Nyquist plots at 1.5 V of SDCNiCo25 in CO_2/CO = 90/10 under SOEC mode.

4.6 Conclusion

In this study, a series of dope ceria based and Ni and/or Co doped hybrid materials were fabricated via reduction treatment and in situ exsolution process. Electrochemical characterizations were performed using LSGM electrolyte-supported SOECs, and the single cell with SDCNiCo25 electrode yielded an excellent current density of 2.7 A cm^{-2} at 1.5 V, 750 °C. This was achieved through fine-tuning the Ni and Co doping percentages for optimized electrochemical activity towards CO_2RR. After the structure and properties of SDCNiCo25 being systemically characterized and confirmation of existence of NiCo alloy, the synergistic effects of Ni and Co were studied via comparison with SDCNi25 and SDCCo25. Thus, the Ni and Co co-doping method could be an effective approach to greatly enhance the CO_2RR process and lower the operating temperature of CO_2 SOEC.

Chapter 5 - High-performance reversible solid oxide cells for powering electric vehicles, long-term energy storage, and CO_2 conversion

5.1 Metal-supported solid oxide cells

Fossil fuels currently fulfill the majority of the worldwide power requirements and consequently emit substantial amounts of greenhouse gases into the atmosphere. To mitigate the most severe impact of climate change and transition towards a low-carbon society, an imperative exists to increase the utilization of renewable energy sources [39,51,126]. Notably, wind and solar possess abundant potentials to satisfactorily meet the energy demand of our society, but their intermittent nature requires a redesign of efficient energy conversion and storage systems [127,128]. As per the International Energy Agency's report [129,130], approximately 24% of global emissions stem from the transportation sector. Thus, a substantial positive effect can be attained through the advancement of vehicles powered by alternative fuels, such as green hydrogen, sustainable methane, or bioethanol.

In addition to CO_2 emissions, there is also significant cause for worry regarding public health due to pollutants like nitrogen oxides, sulfur oxides, and particulate matters originating from conventional ICEVs. In this regard, BEVs have gained widespread acceptance since the beginning of the previous decade and are currently recognized as the primary route towards achieving decarbonization goals [131]. Nevertheless, battery technology faces some hurdles, including inadequate energy density for long-distance transportation, prolonged charging time, as well as the bulkiness and weight of batteries [132,133]. Solid oxide fuel cells (SOFCs) offer some alternative benefits for powering automobiles due to their superior efficiency when juxtaposed

with combustion engines, fast refueling, silent operation, and relative tolerance towards fuel impurities. Moreover, their high energy density is beneficial, especially for long-distance transportation [25]. Additionally, SOFCs offer fuel flexibility as another advantage.

Metal-supported SOFCs (MS-SOFCs) not only exhibit the aforementioned advantages, but they also possess distinct benefits arising from their steel anode support, including rapid startup capability and exceptional mechanical durability, rendering them an attractive choice for integration into vehicular systems. AVL developed a SOFC auxiliary power unit (APU) which was installed on a Volvo truck to power comfort functions during vehicle standstill [134]. The APU provided about 3 kW of electrical power at 30% electrical efficiency. Ceres Power developed MS-SOFCs exhibiting elevated thermal conductivity and robust mechanical stability, endowing them with the capability to withstand rapid start-up cycles. Stacks comprised of these cells have demonstrated impressive start-up cycles, clocking in at under 10 minutes, and sustaining over 2500 thermal cycles [135]. For the application of SOFCs in the mobile sector, there are still challenges to tackle, such as power density, lifetime and degradation, and fuel flexibility, among others [129,136,137].

Hydrogen production has been successfully showcased through the utilization of metal supported solid oxide electrolysis cells (MS-SOECs) under various conditions [138,139]. Tucker et al.[140] reported a study where they employed $La_{0.6}Sr_{0.4}Co_{0.2}Fe_{0.8}O_3$-$Sm_{0.2}Ce_{0.8}O_3$ (LSCF-SDC) as the air electrode and Ni-SDC as the fuel electrode yielding a current density of 0.6 A cm^{-2} at 1.4 V, 700 °C. Upon post-mortem analysis, two primary degradation modes were identified: Cr poisoning on the air electrode and fuel electrode coarsening; oxidation of the metal support and localized accumulation of nickel. To address these challenges, the researchers applied coatings within the porous stainless metal to mitigate Cr migration. Through the application of

electrophoretic deposition of a $CuMn_{1.8}O_4$ coating, they demonstrated improved initial performance and long-term stability of MS-SOEC [141].

Despite extensive achievements having been made in either fuel cell mode or electrolysis mode, there is limited studies of employing MS-SOCs to achieve reversible operation. RSOCs can function either as SOFCs, converting chemical fuels into electrical energy, or as SOECs, utilizing electricity to generate valuable chemicals. This innovation offers the advantage of circumventing energy losses resulting from the transmission of excess electricity over long distances, and it effectively tackles the challenges posed by peak shaving on microgrids powered by intermittent and discontinuous energy sources [61,142]. Furthermore, there is no investigation using reversible MS-SOCs for vehicular applications. But such progress may be of great interests to policy makers, manufacturers, and common users interested in MS-SOCs technologies, thus our work could help accelerate the progress and enhance the outlook for MS-SOC applications in transportation and other areas.

On the other hand, RSOC systems also have the potential to employ CO_2 as an energy storage medium, facilitating both power-to-gas and gas-to-power conversion [126,143]. Numerous researchers have delved into the realm of CO_2 SOECs, driven by the objectives of enhancing performance, bolstering operational reliability, and lowering cost. The CO_2 electroreduction reaction (CO_2RR) takes place at the fuel electrode, which has been identified as the rate-limiting step. Consequently, mixed oxygen ionic and electronic conductors have been subject to extensive investigation as potential fuel electrodes for the CO_2 electrolyzers [95,144,145]. Fu et al. [146] constructed double perovskite/Ruddlesden-Popper perovskite (DP/RP-P) composites with Fe-Cu nanoparticles for efficient CO_2 conversion. Button cells with the composite perovskites demonstrated a current density towards CO_2 electrolysis as high as 1.7 A cm^{-2} at 800 °C and 1.4

V. Lv et al. [147] proposed a repeated redox manipulations strategy to promote exsolution of Ru-Fe alloy nanoparticles on $Sr_2Fe_{1.4}Ru_{0.1}Mo_{0.5}O_{6-\delta}$ perovskite by enriching the active Ru underneath the bulk surface, leading to enhanced SOEC performance and stability. CO_2 SOECs bring about superior outcomes in terms of energetic efficiency, electric power consumption, and conversion efficiency [148]. Nonetheless, there are limited reports of MS-SOCs for both CO_2 conversion and using CO to generate power in fuel cell mode [138,149,150], which could potentially stem from factors such as the redox instability experienced on the fuel electrode, possible carbon deposition and the tendency for nickel coarsening.

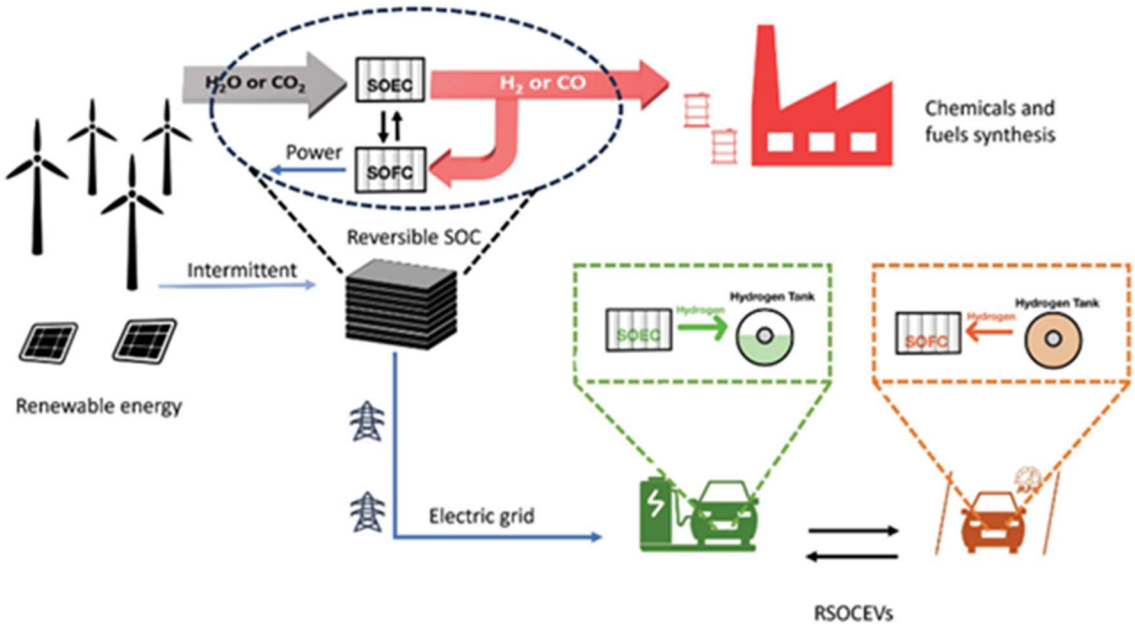

Figure 53. Schematic illustration of the future energy system that relies heavily on RSOC technology. Illustration of RSOCs incorporated into the renewable energy system and further integration with RSOCEV technologies.

In this work, as displayed in Figure 54, RSOCs were first analyzed for their application to power electric vehicles, then compared with ICEVs and BEVs in terms of merits such as power densities and energy densities, which led to discussion on the advantages and prospects of RSOCEVs. Our H_2-H_2O RSOCs have demonstrated remarkable electrochemical performance in both fuel cell and electrolysis modes. In fuel cell mode, a peak power density of 1.6 W cm^{-2} at 750 °C was achieved, and in the electrolysis mode, a current density of 2.0 A cm^{-2} at 1.3 V and 750 °C was attained. Notably, these cells exhibited durable reversible operations across a wide range of conditions. Compared to the BEVs, it has been identified that RSOCs can power vehicles with higher volumetric and gravimetric power densities and energy densities, as well as shorter charging/refueling time. Additionally, a world record current density of 3.4 A cm^{-2} at 1.5 V and 750 °C was attained in CO_2 electrolysis. Furthermore, we gauged the efficiency of CO_2 splitting using RSOCs, providing valuable insights to guide energy storage strategies and efforts aimed at mitigating CO_2 emissions. RSOC technology holds the potential to play a pivotal role in the future energy landscape, contributing to power electric vehicles and the reduction of CO_2 emissions.

5.2 Reversible MS-SOC performance in H_2-H_2O

The electrochemical performance of the reversible cells in H_2-H_2O was thoroughly investigated. Figure 55 displays the typical current-voltage (I-V) curves of the single cells with a ratio of H_2/H_2O being 97/3 for fuel cell assessment and 60/40 for electrolysis analysis. The fuel cell PPDs are 1.6 W cm^{-2}, 1.0 W cm^{-2}, 0.6 W cm^{-2}, 0.3 W cm^{-2} at 750 °C, 700 °C, 650 °C, and 600 °C, respectively, representing remarkable performance among other reversible SOCs (Table C1). The outstanding performance can be attributed to the superior conductivity of the ScYSZ

electrolyte, along with the exceptional electrochemical activity of the PBSCF-b+BSC hybrid air electrode that exhibits both high oxygen reduction reaction and oxygen evolution reaction activities [40]. Figure 56 demonstrates the electrochemical impedance spectroscopy (EIS) results of MS-SOC under OCV condition, which reveals the ohmic area-specific resistance (ASR_{Ω}) and electrode polarization area-specific resistance (ASR_p). As shown in Table C2, our MS-SOCs exhibit much lower ASR_p values than previously reported results, further affirming our PBSCF-b+BSC air electrode is highly active.

The MS-SOCs also show exception performance in steam electrolysis mode for hydrogen production. As shown in Figure 55, at an applied voltage of 1.3 V, a current density of -2.0 A cm^{-2}, -1.5 A cm^{-2}, -0.86 A cm^{-2}, -0.43 A cm^{-2} is achieved at an operating temperature of 750 °C, 700 °C, 650 °C, and 600 °C, respectively. Our results showcase a superior performance when compared to other MS-SOECs operating under similar conditions, as reported in the literature (Table C3).

We proceeded to assess the round-trip (electricity-to-hydrogen-to-electricity) efficiency within the context of RSOCEV. We have identified a high round-trip efficiency could be achieved by operating the RSOCs under certain conditions. In specific, we can run the electrolyzer at a relatively high current density to reduce the charging time in electrolysis cell (EC) mode, followed by operate the fuel cell at a relatively low current density to achieve a long period of discharging in FC mode [50]. This operational characteristic aligns perfectly with the requirements of RSOCEV for commercial applications, where charging times must be restricted to less than 15 minutes, and a relatively low and resilient power output allows the vehicle to cover long distances, spanning hundreds of miles.

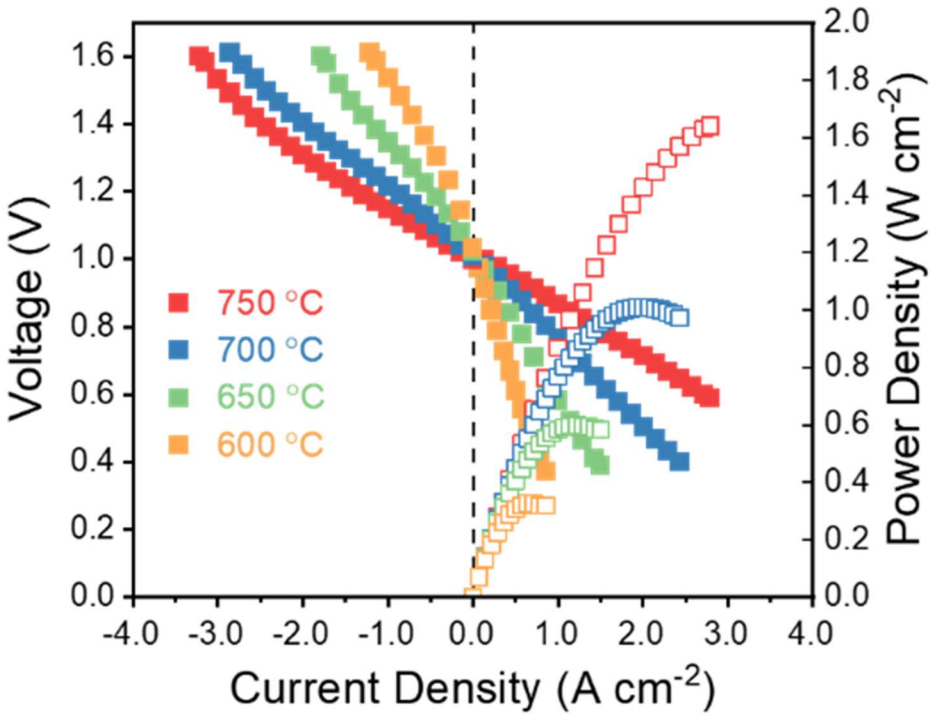

Figure 54. I-V curves in EC mode and I-V-P curves in FC mode at different operating temperatures. H_2O/H_2 = 40/60, and H_2O/H_2 = 3/97 gas mixture were fed to the fuel electrode for EC and FC testing, respectively.

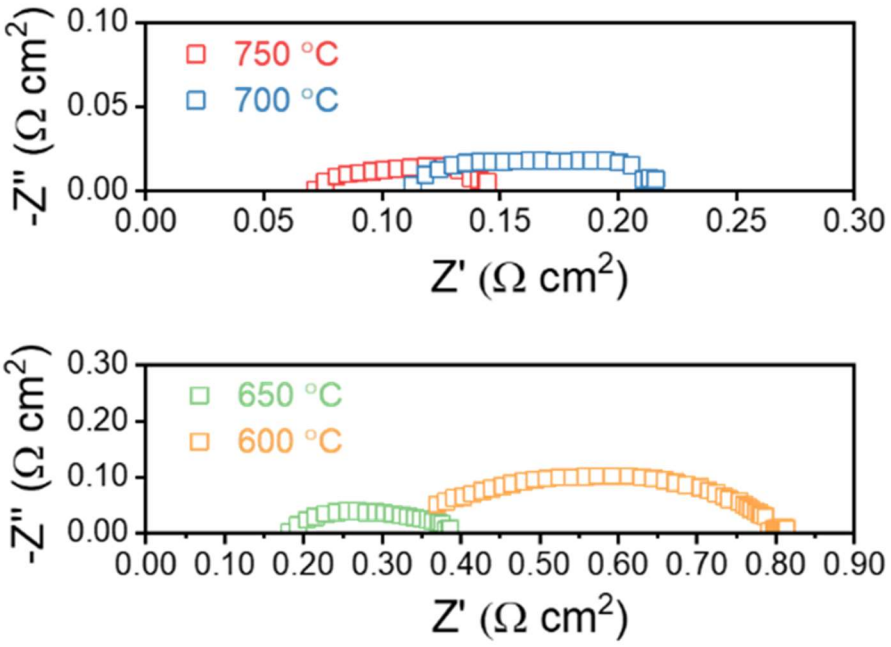

Figure 55. EIS spectra collected under OCV condition in 3% humidified H_2.

Utilizing the parameters detailed in Tables 1 and 2, we can operate the MS-SOC in EC mode as an applied voltage of 1.3 V per cell for 12 minutes. We subsequently evaluated the round-trip efficiency of the RSOCEV based on our reversible MS-SOC results shown in Figure 55. To determine the running time (i.e., discharging time) in FC mode, we set the fuel cell stack output power is 40 kW. As illustrated in Figure 57, the round-trip efficiency of reversible MS-SOC ranges from 69.1% to 64.7% across a wide range operating temperature. With decreasing the operating temperature, the corresponding current densities at 1.3 V decrease as well, resulting in reduced total electrical energy input and a shorter running time at 40 kW. When the stack is charged at 750 °C or 700 °C for merely 12 minutes, the RSOCEV can operate continuously for more than 3 hours at a satisfactory average speed. However, if the charging temperature is lower, a 12-minute charge may not provide sufficient energy for an extended journey. Therefore, the operating temperature should also be controlled and optimized to achieve high round-trip efficiency and extended running, while ensuring the durability.

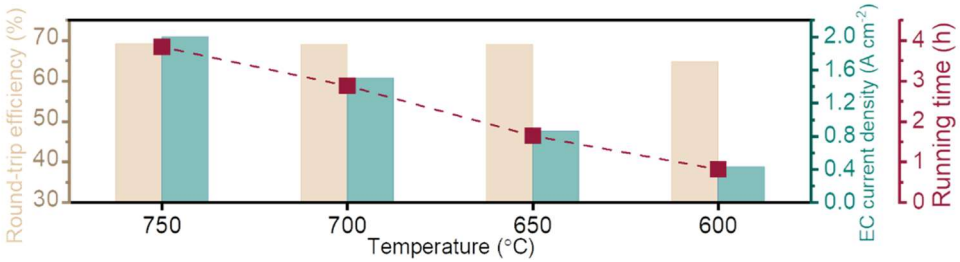

Figure 56. Round-trip efficiency at different operating temperatures and the corresponding charging current densities and running time of the RSOCEV. The charging time is set at 12 minutes, the charging voltage for single cell at 1.3 V, and the average power output of RSOCEV at 40 kW across the operating temperature range.

5.2 Stability and reversible operation of MS-SOCs

Moreover, the reversible MS-SOFCs demonstrate remarkable reversible operation and stability. As shown in Figure 58, with feeding 60 vol. % H_2 and 40 vol. % H_2O to the fuel electrode and air electrode exposed to the ambient air, the MS-SOCs can attain durable and reversible operation. Following the similar operating principles as established for the ideal RSOCEVs, we run the reversible MS-SOCs at a high current density for a short period in EC mode. On the other hand, in FC mode, the MS-SOC is operated at a low current density for a relatively long discharging time. Figure 3B shows the reversible MS-SOCs exhibit minimal degradation after 54 cycles of reversible operation over a period of 160 hours, implying the reversible MS-SOCs could be employed to power vehicles or function as long-term chemical energy storage devices.

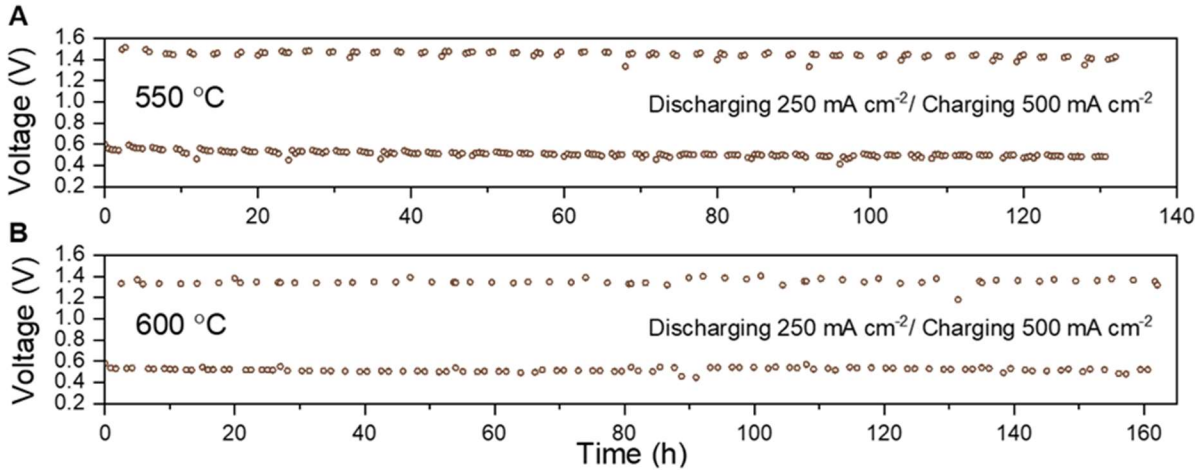

Figure 57. Reversible MS-SOC operation with feeding 60 vol. % H2 and 40 vol. % H2O to the fuel electrode and air electrode exposed to the ambient air. (A) Discharging at a current density of 250 mA cm-2 for 2 hours and charging at a current density of 500 mA cm-2 for 1 hour in each cycle. The operating temperature is 550 °C. (B) Discharging at a current density of 250 mA cm-2 for 2 hours and charging at a current density of 500 mA cm-2 for 1 hour in each cycle. The operating temperature is 600 °C.

5.3 Employing reversible MS-SOCs to power vehicles

While BEVs hold great promise in reducing CO_2 emissions and contributing to a sustainable energy future, they still face significant challenges, notably regarding insufficient energy density and extended charging times. As an alternative, hydrogen-fueled fuel cell vehicles have been developed, offering quiet operation, environmental friendliness, and performance and range on par with their gasoline-powered counterparts. However, the substantial requirements for hydrogen storage and distribution, which come at a considerable cost and efficiency trade-off, have hindered their widespread adoption. Hence, we have explored an alternative approach in which hydrogen fuel is produced on the vehicles by charging and operating the reversible MS-SOCs in EC mode (Figure 54). After charging, the reversible MS-SOCs will function as fuel cells to generate electricity and power the vehicles.

With the experimental results shown in section 5.2-5.3, we have designed and analyzed an ideal vehicle that are powered with RSOCs. To compare RSOCEVs with BEVs and ICEVs, we have determined the power densities, energy densities, refueling/charging times, and fuel economy – all of which are pivotal criteria for both decision-makers and drivers.

Both high gravimetric and volumetric power densities are essential for reducing the weight of the vehicles and maximizing the cargo spaces. As shown in Figures 59A and 59B, it is evident that the gravimetric and volumetric power densities of RSOCEVs significantly surpass those of ICEVs and BEVs. This outcome aligns with expectation due to the inherent difference in power delivery mechanisms between these vehicle types. Notably, ICEVs exhibit the lowest power densities, primarily stemming from their reliance on the gradual buildup of torque as engines revolutions increase. In contrast, electric vehicles are capable of instantaneously delivering maximum torque from the outset. Moreover, electric motors are highly efficient in

converting electrical energy while ICEVs are plagued by energy losses incurred through heat dissipation, mechanical vibrations, and other mechanical inefficiencies, diminishing their effective power output. Furthermore, in contrast to the bulky and heavy battery that BEV carries, both the metal-supported RSOCEV stack, which is more compact and the hydrogen tank, made of carbon fiber-reinforced plastic, contribute to the superior power densities of RSOCEV [43]. Therefore, powering the vehicles with reversible MS-SOCs can reduce the vehicle weight, while offering more storage holds.

While hydrogen possesses a commendable gravimetric specific energy, its volumetric energy density presents a challenge, highlighting the ongoing need for advancements in hydrogen compression technologies. Nevertheless, it's noteworthy that the trends in comparing gravimetric and volumetric energy densities exhibit notable similarities (Figures 59C and 59D). As previously discussed, BEVs necessitate substantial volume and weight for accommodating their batteries, thereby resulting in relatively low energy densities. Nonetheless, BEVs continue to hold considerable appeal due to their numerous advantages, particularly their efficiency. ICEVs achieve unparalleled energy densities, especially in terms of its volumetric specifics, which is mainly due to the high energy density of liquid gasoline.

Additionally, we conducted an analysis and comparison of the refueling/charging durations for these three types of vehicles under the fair assumption that the energy output of RSOCEVs matches that of BEVs. The results are illustrated in Figure 59E. It is evident that ICEVs boast the shortest refueling times, a characteristic that is unlikely to face any challenges in the foreseeable future, which underscores the inherent advantage of ICEVs in terms of refueling speed. On the other hand, RSOCEVs exhibits a significant advantage over BEVs with regard to charging time, requiring only one-third of the time needed compared to their battery-

driven counterparts. This demonstrates the potential of RSOCEVs for enhancing overall time efficiency.

Furthermore, we analyzed the fuel economy of these three types of vehicles, with detailed calculation in the Methods section. Conventionally, miles per gallon (mpg) is the benchmark for assessing fuel efficiency and cost. However, it is not suitable when electric vehicles are involved and the EPA quantifies energy consumption and efficiency in relation to the number of kWh needed to power a vehicle over a distance of 100 miles instead. As shown in Figure 59F, BEVs require the lowest energy input to run 100 miles, mainly due to their superior efficiency delivering electricity to the motor. When comparing RSOCEVs and ICEVs, the former is ~25% more efficient than the latter.

While RSOCs hold promise for applications in powering electric vehicles, the technology is still in its early stage of development, pending technology validation in lab-scale setting, and further demonstration in industrially relevant environments. In addition to the key merits discussed above, other factors should also be emphasized for its further application, including degradation and lifetime, fuel flexibility, and cost.

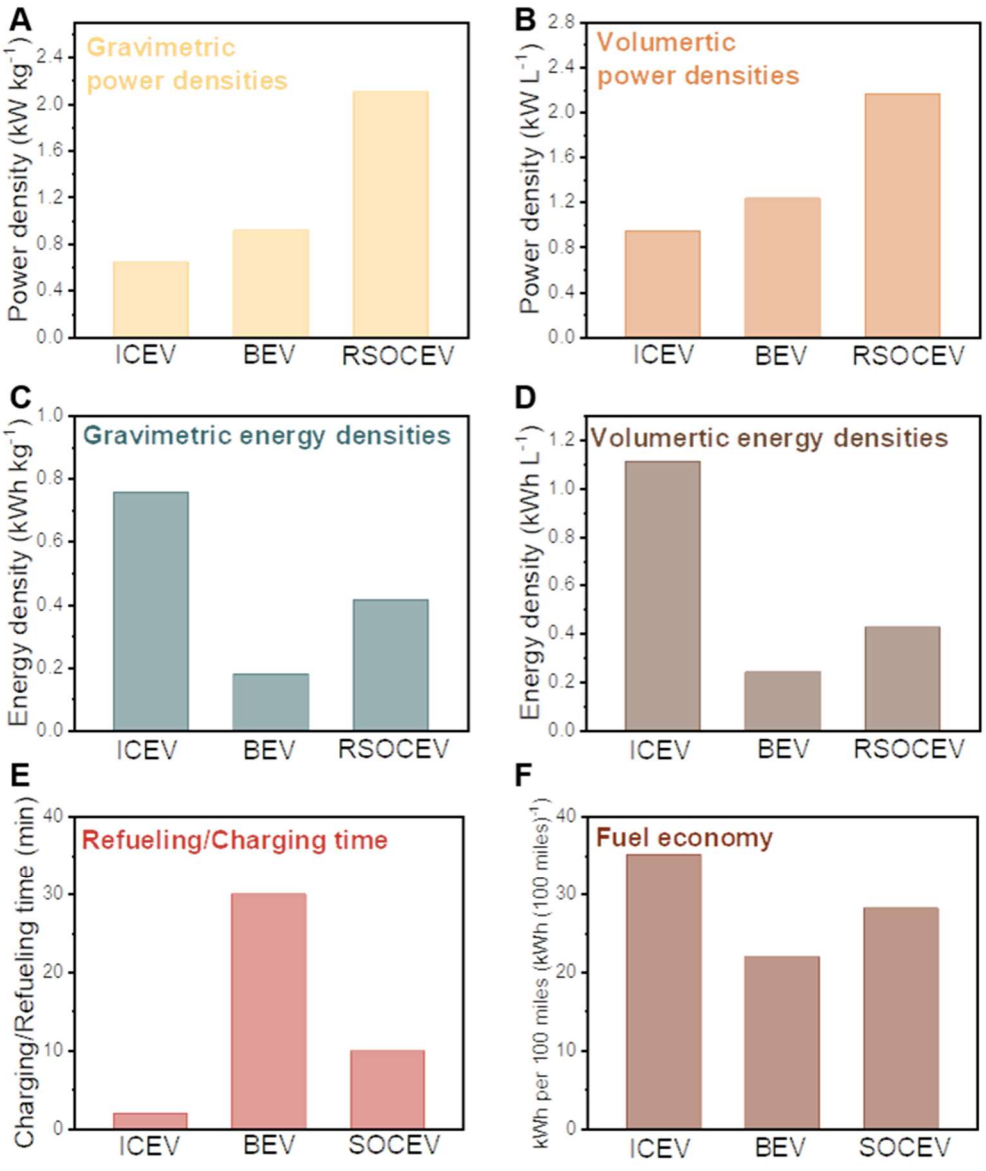

Figure 58 Comparison between ICEV, BEV and RSOCEV. (A) Gravimetric power densities. (B) Volumetric power densities. (C) Gravimetric energy densities. (D) Volumetric energy densities. (E) Refueling/Charging time. (F) Fuel economy.

5.4 Reversible MS-SOC operation in CO-CO_2

One compelling characteristic of SOCs is their capability to operate in reversible modes, accommodating either H_2-H_2O or CO-CO_2 as the gas mixture fed to the fuel electrode. Herein, CO_2 electrolysis performance was evaluated within a temperature range of 600-750 °C, with the fuel electrode being supplied with 100 sccm of 10 vol. % CO + 90 vol. % CO_2 gas mixture while the air electrode was exposed to ambient air.

The thermoneutral voltage for CO_2 electrolysis, approximately 1.5 V, corresponds to the point at which the Joule heat generated due to internal resistance equals the heat required for the CO_2 reduction reaction. Operating at this voltage is ideally preferable because it entails no additional energy input in the form of heat, and no surplus energy is wasted unless using a higher voltage. Consequently, the current density achieved at 1.5 V serves as a common indicator of electrolysis cell performance. As shown in Figure 60, a current density of -3.4 A cm^{-2}, -2.9 A cm^{-2}, -2.2 A cm^{-2}, and -1.3 A cm^{-2} is attained at 750 °C, 700 °C, 650 °C, and 600 °C, respectively. Such performances are so superior when compared to the existing literature results, with the additional advantage of significantly lower operating temperatures that are crucial to circumvent the degradation issue and reduce the electricity consumption [32,94,99,109,124,144,145,151–156]. The EIS analysis offers valuable insights into the exceptional performance observed. As shown in Figure 61, the point of intersection of the EIS at high frequencies along the real-axis signifies the ASR_{Ω}, which is primarily a result of ionic transport resistance within the electrolyte. Meanwhile, the difference between the high-frequency and low-frequency intercepts corresponds to the ASR_p. Compared to ASRo and ASRp values under similar conditions in the literature, our cell demonstrated much lower values resulting in the superior performance (Table C4).

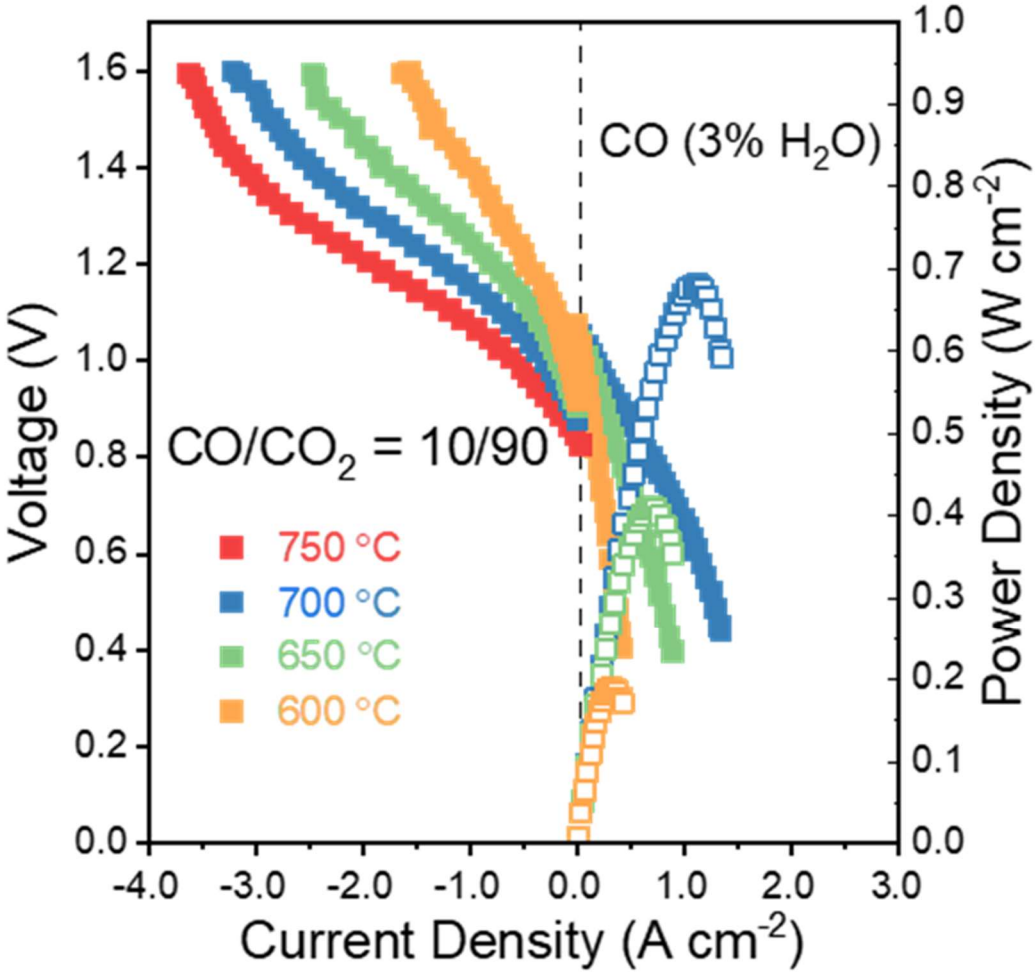

Figure 59. I-V curves in EC mode and I-V-P curves in FC mode at different operating temperatures. CO/CO_2 = 10/90, and CO/H_2O= 97/3 gas mixture were fed to the fuel electrode for EC and FC testing, respectively.

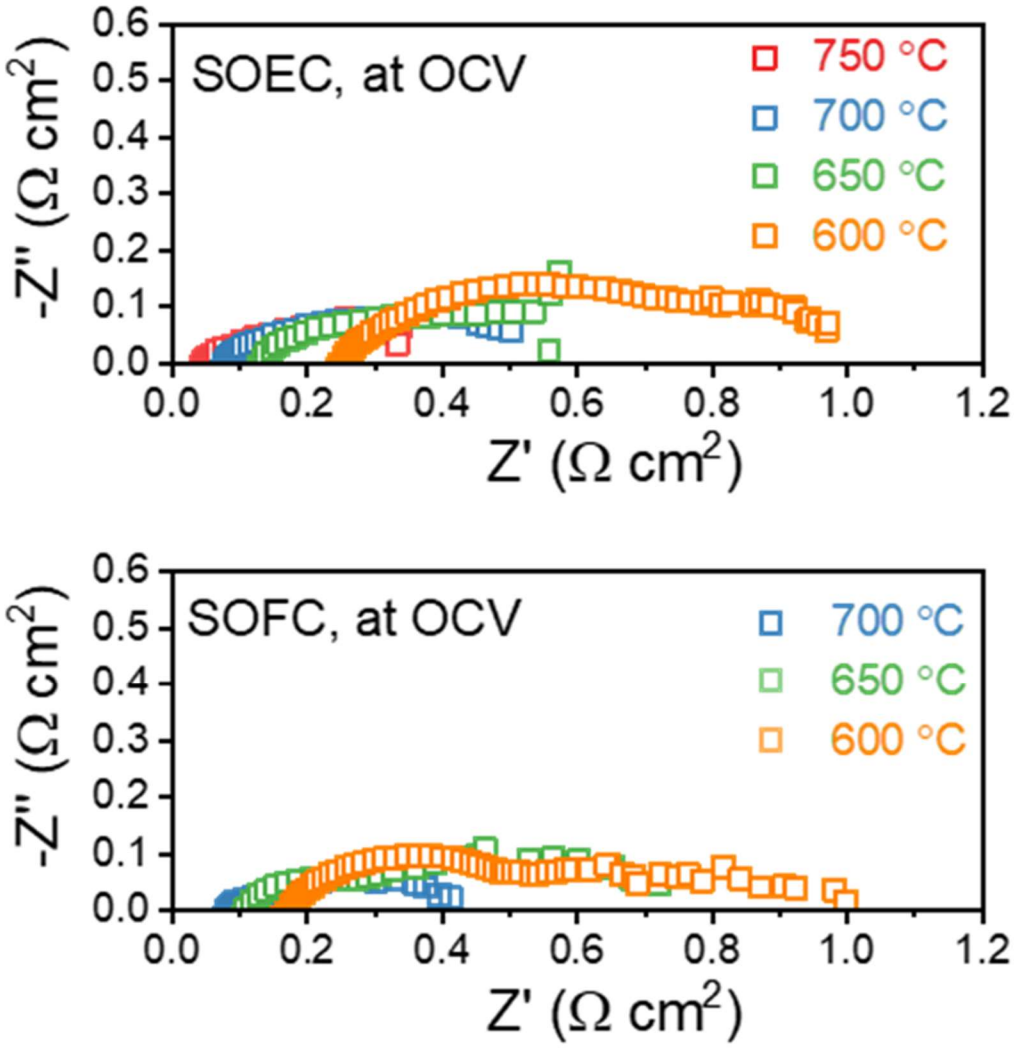

Figure 60. SOEC EIS spectra collected under OCV condition in CO/CO_2 = 10/90, and SOFC EIS spectra collected under OCV condition in CO/H_2O= 97/3.

The performance of CO-fueled fuel cells is presented in Figure 60, where humidified CO (3% humidity) is utilized as the stream fed to the fuel electrode. A bubbler was employed to introduce 3% humidity into the fuel feed, a common practice in the literature [157,158]. It is evident that the OCVs in the fuel cell mode, as depicted in Figure 60, surpass those in the electrolysis mode. This discrepancy arises from the variation in gas composition supplied to the fuel electrode, as predicted by the Nernst equation. The PPD achieved was 0.68 W cm^{-2}, 0.41 W cm^{-2}, and 0.19 W cm^{-2} at 700 °C, 650 °C, and 600 °C, respectively. In contrast, the performance when using a CO-CO_2 gas mixture is considerably lower, signifying that the introduction of CO_2 increases the activation energy of the CO oxidation reaction. When compared to the existing literature results, our CO-fueled SOFC not only demonstrate superior performance but also manages to lower the operating temperature (Table C5). This achievement has the potential of bringing several advantages, including quicker startup, enhanced stability, and reduced component costs, among others. Figures 62 show the CO_2 electrolysis stability testing of two MS-SOCs under distinct conditions. The CO_2 SOECs exhibit good stability, even when subjected to high current densities and reduced operating temperature, showing minimal degradation.

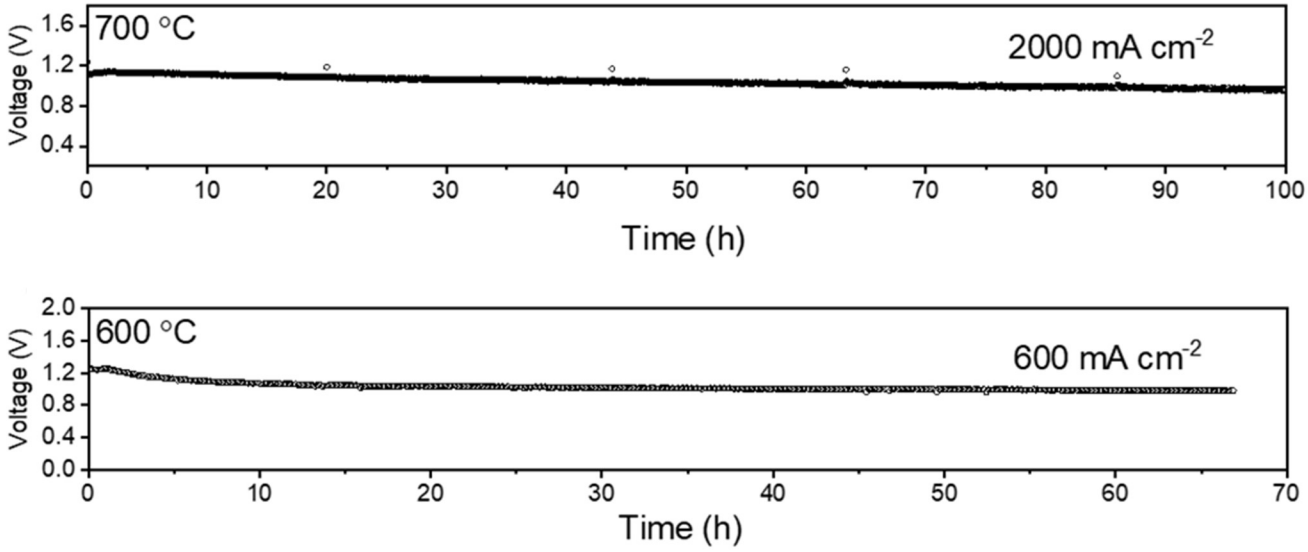

Figure 61. CO_2 electrolysis stability testing under a current density of 2000 mA cm^{-2} at 700 °C, and under a current density of 600 mA cm^{-2} at 600 °C.

5.5 CO_2 electrolysis comparison

The advent of electrochemical technologies presents the potential to revolutionize CO production, offering the prospect of small, on-site facilities that can be activated as needed, thereby obviating the need for CO gas transport [51]. In studies involving low-temperature electrolysis, H-type cells are predominantly employed, in which the solubility of CO_2 in water is only 34×10^{-3} M, limiting the current density to < 100 mA cm^{-2} [159,160]. However, in the context of industrial applications, it is imperative to achieve substantially higher current densities, typically exceeding 200 mA cm^{-2}, to meet the commercially relevant needs [161]. The Faradaic efficiency (FE) represents the selectivity for CO in relation to other products of CO_2 reduction reaction. Inadequate selectivity not only diminishes the utilization rate but also escalates the expenses associated with separating the desired product from by-products. In contrast to SOECs, where the FE approaches 100%, low-temperature electrolyzers confront the common complications arising from the hydrogen evolution reaction (HER), especially in acidic environment [51,159].

Energy efficiency (EE) is defined in Equation 6, and it serves as a metric that characterizes the effectiveness of the conversion of electrical energy into chemical energy stored within the product. EE reflects the energy losses attributed to side reactions and polarization losses. It is worth noting that efficiency losses stemming from other processes, such as those associated with blowers and electrolyte recirculation pumps in low-temperature electrolysis, or poor thermal management and slow reactants diffusion in SOECs are not factored into this calculation [51,162]. As illustrated in Figure 63, the SOEC developed in this study consistently maintains a superior EE (>91%) even when high current densities (900–2000 mA cm^{-2}) are applied across a broad temperature range (550-750 °C). The reason electrolysis at elevated

temperature (550-900 °C) has an EE exceed 100% is that the cost for heat (TΔS) is not accounted for. In contrast, EE values for low-temperature electrolyzers range from 51.1% to 27.3% when operating at commercially relevant current densities of 200-425 mA cm^{-2}. In addition to the previously mentioned advantage of superior FE which is commonly shared in SOECs, the low overpotentials observed in our cells at high current densities also contribute to the enhanced EE.

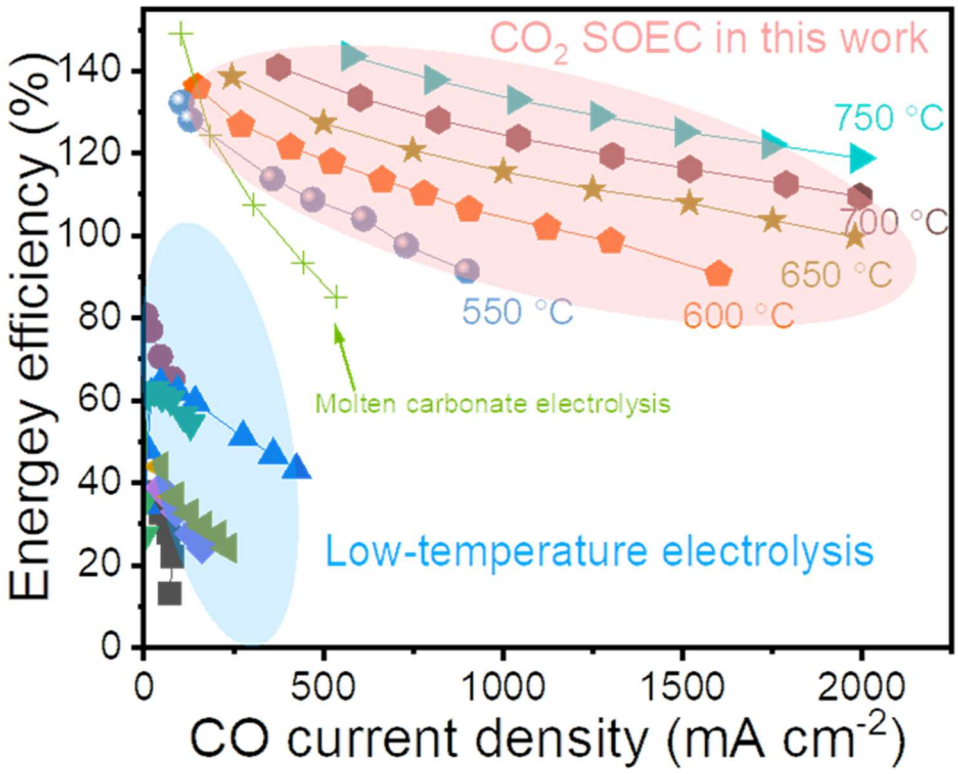

Figure 62. Comparisons of our CO_2 SOEC with other electrolysis technologies regarding their energy efficiencies. The details of low-temperature electrolysis references are in Table S6.

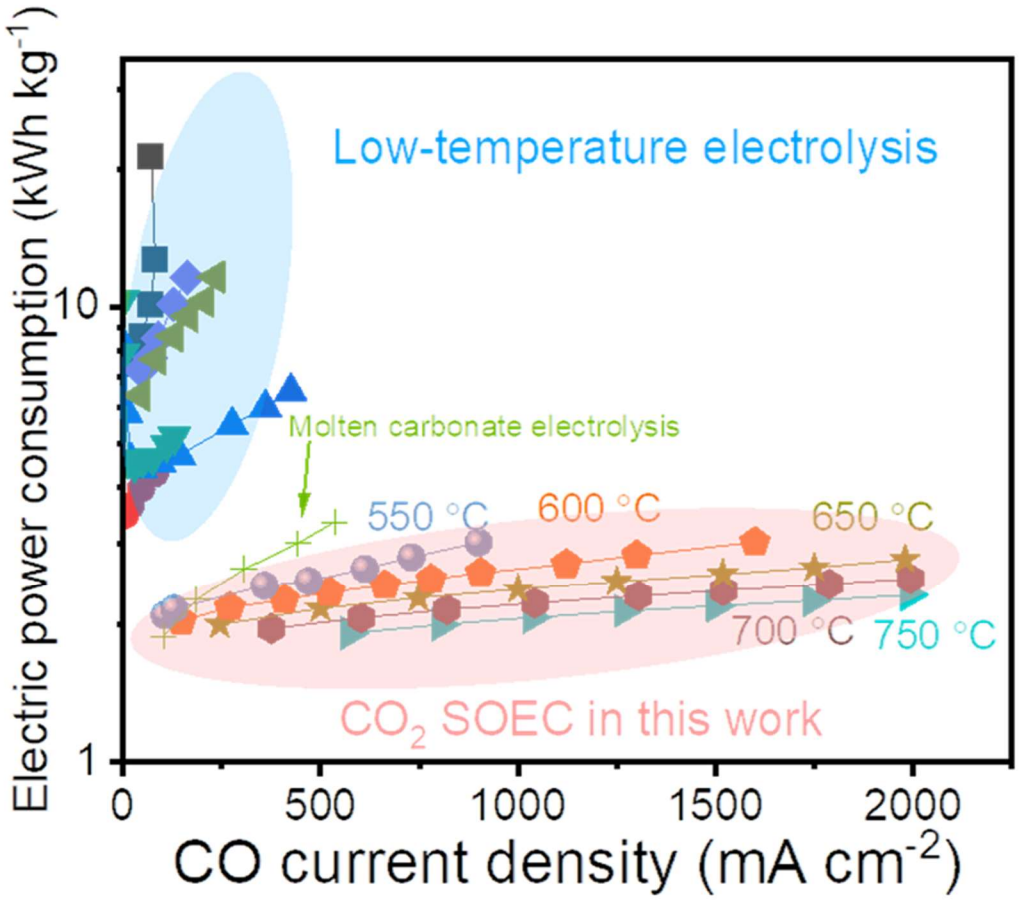

Figure 63. Comparisons of our CO_2 SOEC with other electrolysis technologies regarding electric power consumption. The details of low-temperature electrolysis references are in Table S6.

Another frequently employed metric is the electric power consumption (EPC), as defined in Equation 2.11 which quantifies the amount of electric energy needed to produce 1 kg of CO [51]. Given the thermodynamic characteristics of this process, a substantial amount of the energy required for the CO_2 reduction reaction can be met in the form of heat at elevated temperature [88]. Consequently, the Joule heat that is inevitably generated due to internal resistance could be utilized. And in this way, the power consumption demands for SOEC can be reduced. As shown in Figure 64, EPC values for multiple electrolyzers and our cell operating at 550-750 °C were logarithmically plotted with respect to the CO-specific current density. The EPC for our SOEC remains below 3.0 kWh kg^{-1} even when operating at very high current densities and lower temperatures. In contrast, the EPC for low-temperature electrolyzers is significantly higher. For instance, Pan et al. [163] developed an acid-fed membrane electrode assembly capable of operating at a current density of 140 mA cm^{-2} with a FE of 58% and an EPC of 12.7 kWh kg^{-1} at room temperature. When compared to the theoretical value (operating at the reversible cell voltage of 1.33 V with 100% FE), which stands at 2.6 $kWhkg^{-1}$, 8.2 kWh are lost as heat and 1.9 kWh are wasted to produce by-products for every kg of CO produced.

In Figure 65, a comprehensive review of state-of-the-art SOECs operating at 750 °C and 1.5 V for CO_2 electrolysis is presented. The current density of our cell is the highest compared to all other reported results regardless of the electrolytes and electrodes used.

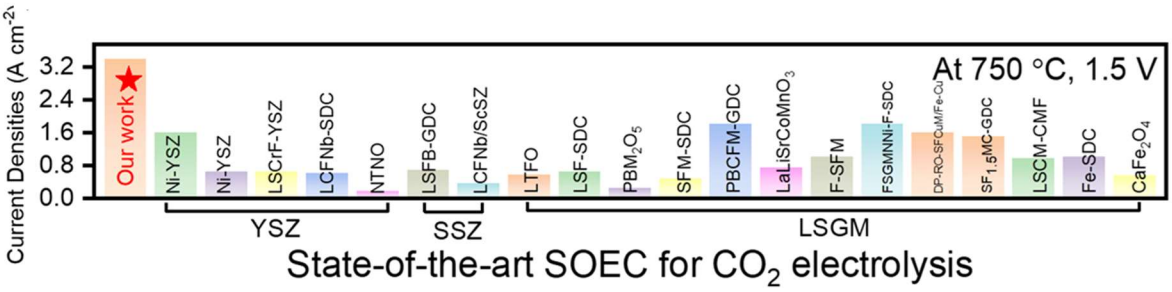

Figure 64. Comparison of the current density of our SOEC with other state-of-the-art SOECs at 750 °C and 1.5 V.

5.6 Conclusion

In this study, we successfully demonstrated RSOCs in both H_2-H_2O and CO-CO_2 fuel mixture with superior performance and durable operation. Furthermore, we discussed the vital role of RSOCs in shaping the sustainable future energy system. For instance, the potentials of RSOCEVs were analyzed, and further compared to ICEVs and BEVs regarding various merits like power densities, energy densities, charging/refueling time, fuel economy and so on. We also assessed the efficiency of our CO_2 electrolysis among other SOECs and low-temperature counterparts through comparison of energy efficiency, electric consumption, and current densities. The high-performance RSOCs in this work demonstrated its potential for applications in powering electric vehicles, energy storage and CO_2 conversion.

Chapter 6 - Conclusion

For this dissertation, I successfully designed oxygen and fuel electrode materials via novel fabricating methods which are straightforward and scale-up friendly, to enhance the efficiency of power and fuel generation in SOCs. The proposed oxygen and fuel electrode materials could be incorporated into the next-generation SOCs with excellent performance. And the validated electro-catalyst design in an effortless and efficient manner could contribute to the electrochemistry society and other catalyst-developing societies.

To address the key challenges of oxygen electrode material development, for instance, the need for a buffer layer between oxygen electrode and electrolyte layers, several times of high-temperature sintering, demands for complicated and costly fabricating instruments, a novel hybrid oxygen electrode material, which is composed of $Pr_{1.39}Ba_{0.14}Sr_{0.53}Co_{1.48}Fe_{0.76}O_{6-\delta}$ and $Ba_{0.66}Sr_{0.34}CoO_{3-\delta}$, have been proposed and studied. This hybrid electrode enhances the oxygen transport kinetics, specifically the surface oxygen exchange and bulk diffusion coefficients of oxygen, which leads to the enhancement of both oxygen reduction reaction and oxygen evolution reaction activity. When YSZ-based fuel electrode-supported SOCs are equipped with the $Pr_{1.39}Ba_{0.14}Sr_{0.53}Co_{1.48}Fe_{0.76}O_{6-\delta}$-$Ba_{0.66}Sr_{0.34}CoO_{3-\delta}$ electrode, unprecedented performance was achieved in both fuel cell and electrolysis cell modes. At 750 °C, a peak power density of 2.4 W cm^{-2} was achieved using H_2 as the fuel. With propane fed to the fuel electrode, a peak power density of 2.6 W cm^{-2} was attained, representing the record in this field. In steam electrolysis mode, a current density of 4.4 A cm^{-2} was demonstrated at 1.3 V and 750 °C, which outperforms all previously reported YSZ-based SOECs. Furthermore, accelerated durability testing showed decent stability under harsh conditions (e.g. charging at 5.0 A cm^{-2}). This research may open the possibility of finding a breakthrough for next-generation electrochemical systems exhibiting

desirable electrocatalytic properties, without the need for complex and costly fabricating procedures.

Leveraging the efficient $Pr_{1.39}Ba_{0.14}Sr_{0.53}Co_{1.48}Fe_{0.76}O_{6-\delta}$-$Ba_{0.66}Sr_{0.34}CoO_{3-\delta}$ electrode, I demonstrated reversible operations with durability and superior performance under different conditions in metal-supported SOCs. Specifically, the SOCs exhibit high electrochemical performances in both fuel cell (PPD = 1.6 W cm^{-2} at 750 °C) and electrolysis mode (current density = 2.0 A cm^{-2} at 1.3 V, 750 °C) with a H_2-H_2O fuel mixture fed to the fuel electrode. Based on the experimental results, I established an ideal RSOC stack under reasonable assumptions, and further discussed its potential of powering the electric vehicles by analyzing and comparing major metrics, such as gravimetric and volumetric power density, gravimetric and volumetric energy density, refueling/charging time, and fuel economy of RSOCEVs, ICEVs, and BEVs. Furthermore, superior performance was also demonstrated in CO-CO_2, with a word-record high current density of 3.4 A cm^{-2} at 750 °C in electrolysis mode, and a PPD of 0.68 W cm^{-2} at 700 °C. Moreover, I evaluated the efficiency of CO_2 electrolysis of our SOECs by comparison of their energy efficiency and electric power consumption with other electrolysis technologies. In summary, the RSOCs technology could be in the center of a future energy system with abundant clean energy sources.

To enhance the hindered CO_2RR in CO_2 electrolysis, I proposed a fuel electrode material where *in situ* exsolved Ni-Co alloy nanoparticles on doped ceria surface greatly improves the performance of CO_2 SOECs. The doping percentages of Ni-Co were optimized between 15% to 30% to elevate the mass transport limitation and achieve maximized current density at thermoneutral voltage. Furthermore, I found that the synergetic effort of Ni-Co alloy plays an

important role in enhancing the CO_2RR activity when compared to single metallic dopant, i.e., Ni or Co.

Bibliography

1 B. T. Na, T. Yang, J. Liu, S. Lee, H. Abernathy, T. Kalapos and G. Hackett, *Solid State Ionics*, 2021, **361**, 115561.
2 H. Li and Z. Lü, *Electrochimica Acta*, 2020, **361**, 137054.
3 J. Kim, *Solid State Ionics*, 2001, **143**, 379–389.
4 A. Leonide, V. Sonn, A. Weber and E. Ivers-Tiffée, *J. Electrochem. Soc.*, 2008, **155**, B36.
5 A. Leonide, B. Rüger, A. Weber, W. A. Meulenberg and E. Ivers-Tiffée, *J. Electrochem. Soc.*, 2010, **157**, B234.
6 Z. Jiang, Z. Lei, B. Ding, C. Xia, F. Zhao and F. Chen, *International Journal of Hydrogen Energy*, 2010, **35**, 8322–8330.
7 C. Graves, S. D. Ebbesen, S. H. Jensen, S. B. Simonsen and M. B. Mogensen, *Nature Mater*, 2015, **14**, 239–244.
8 Y. Wang, T. Su, A. D. Brocato and X.-D. Zhou, *ECS Trans.*, 2019, **91**, 1527–1533.
9 K. Joong Yoon, M. Biswas, H.-J. Kim, M. Park, J. Hong, H. Kim, J.-W. Son, J.-H. Lee, B.-K. Kim and H.-W. Lee, *Nano Energy*, 2017, **36**, 9–20.
10 Y. Liu, Y. Tian, W. Wang, Y. Li, S. Chattopadhyay, B. Chi and J. Pu, *ACS Appl. Mater. Interfaces*, 2020, **12**, 57941–57949.
11 Y. Liu, Y. Tian, W. Wang, Y. Li, S. Chattopadhyay, B. Chi and J. Pu, *ACS Appl. Mater. Interfaces*, 2020, **12**, 57941–57949.
12 H. Shimada, T. Yamaguchi, H. Kishimoto, H. Sumi, Y. Yamaguchi, K. Nomura and Y. Fujishiro, *Nat Commun*, 2019, **10**, 5432.
13 M. S. Khan, X. Xu, R. Knibbe and Z. Zhu, *Renewable and Sustainable Energy Reviews*, 2021, **143**, 110918.
14 Z. Teng, Z. Xiao, G. Yang, L. Guo, X. Yang, R. Ran, W. Wang, W. Zhou and Z. Shao, *Materials Today Energy*, 2020, **17**, 100458.
15 B.-H. Yun, K. J. Kim, D. W. Joh, M. S. Chae, J. J. Lee, D. Kim, S. Kang, D. Choi, S.-T. Hong and K. T. Lee, *J. Mater. Chem. A*, 2019, **7**, 20558–20566.
16 S.-L. Zhang, H. Wang, M. Y. Lu, A.-P. Zhang, L. V. Mogni, Q. Liu, C.-X. Li, C.-J. Li and S. A. Barnett, *Energy Environ. Sci.*, 2018, **11**, 1870–1879.
17 Y. Yang, X. Tong, A. Hauch, X. Sun, Z. Yang, S. Peng and M. Chen, *Chemical Engineering Journal*, 2021, **417**, 129260.
18 J. Cao, Y. Li, Y. Zheng, S. Wang, W. Zhang, X. Qin, G. Geng and B. Yu, *Advanced Energy Materials*, 2022, 2200899.
19 Y. Zhang, F. Yan, B. Hu, C. Xia and M. Yan, *J. Mater. Chem. A*, 2020, **8**, 17442–17448.
20 F. Zhou, Y. Liu, X. Zhao, W. Tang, S. Yang, S. Zhong and M. Wei, *International Journal of Hydrogen Energy*, 2018, **43**, 18946–18954.
21 Y.-M. Kim, P. Kim-Lohsoontorn and J. Bae, *Journal of Power Sources*, 2010, **195**, 6420–6427.
22 L. Jiang, T. Wei, R. Zeng, W.-X. Zhang and Y.-H. Huang, *Journal of Power Sources*, 2013, **232**, 279–285.
23 L. Lu, C. Ni, M. Cassidy and J. T. S. Irvine, *J. Mater. Chem. A*, 2016, **4**, 11708–11718.
24 Y. Jiang, F. Chen and C. Xia, *Journal of Power Sources*, 2021, **493**, 229713.
25 D. J. L. Brett, A. Atkinson, N. P. Brandon and S. J. Skinner, *Chem. Soc. Rev.*, 2008, **37**, 1568.

26 A. M. Abdalla, S. Hossain, A. T. Azad, P. M. I. Petra, F. Begum, S. G. Eriksson and A. K. Azad, *Renewable and Sustainable Energy Reviews*, 2018, **82**, 353–368.
27 S. Y. Gómez and D. Hotza, *Renewable and Sustainable Energy Reviews*, 2016, **61**, 155–174.
28 K. Chen, N. Li, N. Ai, M. Li, Y. Cheng, W. D. A. Rickard, J. Li and S. P. Jiang, *J. Mater. Chem. A*, 2016, **4**, 17678–17685.
29 Y. Tian, W. Wang, Y. Liu, A. Naden, M. Xu, S. Wu, B. Chi, J. Pu and J. T. S. Irvine, *ACS Catal.*, 2021, **11**, 3704–3714.
30 W. Zhang, Y. Zhou, A. M. Hussain, D. Song, Y. Miura, Y. Chen, Z. Luo, N. Kane, Y. Niu, N. Dale, Y. Fukuyama and M. Liu, *ACS Appl. Mater. Interfaces*, 2021, **13**, 4993–4999.
31 Z. Chen, L. Jiang, S. He, C. Guan, Y. Zou, Z. Yue, N. Ai, S. P. Jiang, Y. Shao and K. Chen, *Applied Catalysis B: Environmental*, 2022, **305**, 121056.
32 Y. Song, X. Zhang, K. Xie, G. Wang and X. Bao, *Adv. Mater.*, 2019, **31**, 1902033.
33 R. Banerjee, A. Phan, B. Wang, C. Knobler, H. Furukawa, M. O'Keeffe and O. M. Yaghi, *Science*, 2008, **319**, 939–943.
34 J. Alcalde, S. Flude, M. Wilkinson, G. Johnson, K. Edlmann, C. E. Bond, V. Scott, S. M. V. Gilfillan, X. Ogaya and R. S. Haszeldine, *Nat Commun*, 2018, **9**, 2201.
35 W. Gao, T. Zhou, Y. Gao, B. Louis, D. O'Hare and Q. Wang, *Journal of Energy Chemistry*, 2017, **26**, 830–838.
36 B. Seoane, J. Coronas, I. Gascon, M. E. Benavides, O. Karvan, J. Caro, F. Kapteijn and J. Gascon, *Chem. Soc. Rev.*, 2015, **44**, 2421–2454.
37 Y. Zhang, Q. Zhu, X. Lin, Z. Xu, J. Liu, Z. Wang, J. Zhou and K. Cen, *Applied Energy*, 2013, **108**, 1–7.
38 J. Wang, G. Li, Z. Li, C. Tang, Z. Feng, H. An, H. Liu, T. Liu and C. Li, *Sci. Adv.*, 2017, **3**, e1701290.
39 A. Hauch, R. Küngas, P. Blennow, A. B. Hansen, J. B. Hansen, B. V. Mathiesen and M. B. Mogensen, *Science*, 2020, **370**, eaba6118.
40 L. Fang, F. Liu, D. Diercks, P. Kumar, F. Zhao, D. Ding and C. Duan, *J. Mater. Chem. A*, 2023, **11**, 21251–21262.
41 F. Liu, H. Deng, D. Diercks, P. Kumar, M. H. A. Jabbar, C. Gumeci, Y. Furuya, N. Dale, T. Oku, M. Usuda, P. Kazempoor, L. Fang, D. Chen, B. Liu and C. Duan, *Nat Energy*, 2023, **8**, 1145–1157.
42 *US EPA_ARB Application - Model S - L2S.xlsx*, .
43 *2020 Toyota Mirai*, .
44 Z. Salameh, in *Renewable Energy System Design*, Elsevier, 2014, pp. 201–298.
45 T. A. Schmauss and S. A. Barnett, *ACS Energy Lett.*, 2021, **6**, 3180–3184.
46 *2022 Toyota Camry ebrochure*, .
47
48 P. L. Anderson and A. D'Souza, *Comparison: Real World Cost of Fueling EVs and ICE Vehicles*, 2021.
49 C. E. Thomas, *International Journal of Hydrogen Energy*, 2009, **34**, 6005–6020.
50 C. Duan, R. Kee, H. Zhu, N. Sullivan, L. Zhu, L. Bian, D. Jennings and R. O'Hayre, *Nat Energy*, 2019, **4**, 230–240.
51 R. Küngas, *J. Electrochem. Soc.*, 2020, **167**, 044508.
52 Z. Shao, W. Zhou and Z. Zhu, *Progress in Materials Science*, 2012, **57**, 804–874.
53 M. Liu, M. E. Lynch, K. Blinn, F. M. Alamgir and Y. Choi, *Materials Today*, 2011, **14**, 534–546.

54 P. A. Connor, X. Yue, C. D. Savaniu, R. Price, G. Triantafyllou, M. Cassidy, G. Kerherve, D. J. Payne, R. C. Maher, L. F. Cohen, R. I. Tomov, B. A. Glowacki, R. V. Kumar and J. T. S. Irvine, *Adv. Energy Mater.*, 2018, **8**, 1800120.
55 M. Singh, D. Zappa and E. Comini, *International Journal of Hydrogen Energy*, 2021, **46**, 27643–27674.
56 M. C. Offutt, *Department of Energy Funding for Hydrogen and Fuel Cell Technology Programs FY2022*, DOE, 2023.
57 Y. Niu, Y. Zhou, W. Lv, Y. Chen, Y. Zhang, W. Zhang, Z. Luo, N. Kane, Y. Ding, L. Soule, Y. Liu, W. He and M. Liu, *Adv. Funct. Mater.*, 2021, **31**, 2100034.
58 B.-K. Park and S. A. Barnett, *J. Mater. Chem. A*, 2020, **8**, 11626–11631.
59 B.-K. Park, R. Scipioni, Q. Zhang, D. Cox, P. W. Voorhees and S. A. Barnett, *J. Mater. Chem. A*, 2020, **8**, 11687–11694.
60 X. Tong, Y. Xu, Đ. Tripković, P. V. Hendriksen, W.-R. Kiebach and M. Chen, *J. Mater. Chem. A*, 2020, **8**, 9039–9048.
61 G. Li, Y. Gou, X. Cheng, Z. Bai, R. Ren, C. Xu, J. Qiao, W. Sun, Z. Wang and K. Sun, *ACS Appl. Mater. Interfaces*, 2021, **13**, 34282–34291.
62 H. Liu, X. Zhu, M. Cheng, Y. Cong and W. Yang, *Chem. Commun.*, 2011, **47**, 2378–2380.
63 L. Zhang, D. Li and S. Zhang, *Ceramics International*, 2017, **43**, 2859–2863.
64 Y. Zhu, W. Zhou, Y. Chen and Z. Shao, *Angew. Chem. Int. Ed.*, 2016, **55**, 8988–8993.
65 T. Chen, Y. Zhou, M. Liu, C. Yuan, X. Ye, Z. Zhan and S. Wang, *Electrochemistry Communications*, 2015, **54**, 23–27.
66 H. Yu, H. Im and K. T. Lee, *Adv Funct Materials*, 2022, 2207725.
67 J. H. Park, C. H. Jung, K. J. Kim, D. Kim, H. R. Shin, J.-E. Hong and K. T. Lee, *ACS Appl. Mater. Interfaces*, 2021, **13**, 2496–2506.
68 J. Kim, S. Im, S. H. Oh, J. Y. Lee, K. J. Yoon, J.-W. Son, S. Yang, B.-K. Kim, J.-H. Lee, H.-W. Lee, J.-H. Lee and H.-I. Ji, *Sci. Adv.*, 2021, **7**, eabj8590.
69 J. Yan, Z. Zhao, L. Shang, D. Ou and M. Cheng, *Journal of Power Sources*, 2016, **319**, 124–130.
70 K. Joong Yoon, M. Biswas, H.-J. Kim, M. Park, J. Hong, H. Kim, J.-W. Son, J.-H. Lee, B.-K. Kim and H.-W. Lee, *Nano Energy*, 2017, **36**, 9–20.
71 Y. Chen, S. Yoo, Y. Choi, J. H. Kim, Y. Ding, K. Pei, R. Murphy, Y. Zhang, B. Zhao, W. Zhang, H. Chen, Y. Chen, W. Yuan, C. Yang and M. Liu, *Energy Environ. Sci.*, 2018, **11**, 2458–2466.
72 D. Ding, X. Li, S. Y. Lai, K. Gerdes and M. Liu, *Energy Environ. Sci.*, 2014, **7**, 552.
73 M. Choi, J. Paik, D. Kim, D. Woo, J. Lee, S. J. Kim, J. Lee and W. Lee, *Energy Environ. Sci.*, 2021, **14**, 6476–6483.
74 H. Abernathy, T. Yang, J. Liu and B. Na, 2021.
75 T. H. Wan, M. Saccoccio, C. Chen and F. Ciucci, *Electrochimica Acta*, 2015, **184**, 483–499.
76 Y. Chen, Y. Choi, S. Yoo, Y. Ding, R. Yan, K. Pei, C. Qu, L. Zhang, I. Chang, B. Zhao, Y. Zhang, H. Chen, Y. Chen, C. Yang, B. deGlee, R. Murphy, J. Liu and M. Liu, *Joule*, 2018, **2**, 938–949.
77 H. Ren, Y. H. Lee, E. A. Wu, H. Chung, Y. S. Meng, E. E. Fullerton and N. Q. Minh, *ACS Appl. Energy Mater.*, 2020, **3**, 8135–8142.
78 Y. Takeda, R. Kanno, M. Noda, Y. Tomida and O. Yamamoto, *J. Electrochem. Soc.*, 1987, **134**, 2656–2661.
79 D. A. Osinkin, *Electrochimica Acta*, 2021, **372**, 137858.

80 J. Hayd and E. Ivers-Tiffée, *J. Electrochem. Soc.*, 2013, **160**, F1197–F1206.
81 A. A. Kurteeva, S. M. Beresnev, D. A. Osinkin, B. L. Kuzin, G. K. Vdovin, V. D. Zhuravlev, N. M. Bogdanovich, D. I. Bronin, A. A. Pankratov and I. Yu. Yaroslavtsev, *Russ J Electrochem*, 2011, **47**, 1381–1388.
82 Y. Tian, J. Li, Y. Liu, J. Yang, B. Liu, L. Jia, J. Jiang, B. Chi, J. Pu and J. Li, *International Journal of Hydrogen Energy*, 2018, **43**, 12603–12609.
83 Y. Song, X. Zhang, K. Xie, G. Wang and X. Bao, *Advanced Materials*, 2019, **31**, 1902033.
84 M. C. O. Monteiro, M. F. Philips, K. J. P. Schouten and M. T. M. Koper, *Nat Commun*, 2021, **12**, 4943.
85 Y. Yang, Y. Li, Y. Jiang, M. Zheng, T. Hong, X. Wu and C. Xia, *Electrochimica Acta*, 2018, **284**, 159–167.
86 Y. Li, X. Chen, Y. Yang, Y. Jiang and C. Xia, *ACS Sustainable Chem. Eng.*, 2017, **5**, 11403–11412.
87 X. Yang, K. Sun, M. Ma, C. Xu, R. Ren, J. Qiao, Z. Wang, S. Zhen, R. Hou and W. Sun, *Applied Catalysis B: Environmental*, 2020, **272**, 118968.
88 T. M. Gür, *Progress in Energy and Combustion Science*, 2022, **89**, 100965.
89 M. C. Tucker, *Journal of Power Sources*, 2010, **195**, 4570–4582.
90 S. Lee, M. Kim, K. T. Lee, J. T. S. Irvine and T. H. Shin, *Adv. Energy Mater.*, 2021, **11**, 2100339.
91 Y. Li, B. Hu, C. Xia, W. Q. Xu, J. P. Lemmon and F. Chen, *J. Mater. Chem. A*, 2017, **5**, 20833–20842.
92 Y. Song, Z. Zhou, X. Zhang, Y. Zhou, H. Gong, H. Lv, Q. Liu, G. Wang and X. Bao, *J. Mater. Chem. A*, 2018, **6**, 13661–13667.
93 H. Li, G. Sun, K. Xie, W. Qi, Q. Qin, H. Wei, S. Chen, Y. Wang, Y. Zhang and Y. Wu, *International Journal of Hydrogen Energy*, 2014, **39**, 20888–20897.
94 Y. Li, K. Xie, S. Chen, H. Li, Y. Zhang and Y. Wu, *Electrochimica Acta*, 2015, **153**, 325–333.
95 Q. Liu, X. Dong, G. Xiao, F. Zhao and F. Chen, *Adv. Mater.*, 2010, **22**, 5478–5482.
96 M. Li, B. Hua, J. Chen, Y. Zhong and J.-L. Luo, *Nano Energy*, 2019, **57**, 186–194.
97 W. C. Chueh, Y. Hao, W. Jung and S. M. Haile, *Nature Mater*, 2012, **11**, 155–161.
98 J. G. Lee, O. S. Jeon, H. J. Hwang, J. Jang, Y. Lee, S. H. Hyun and Y. G. Shul, *Electrochimica Acta*, 2016, **191**, 677–686.
99 Y. Jiang, L. Ye, S. Zhang and C. Xia, *J. Mater. Chem. A*, 2022, **10**, 9380–9383.
100 T. L. Skafte, B. R. Sudireddy, P. Blennow and C. Graves, *ECS Trans.*, 2016, **72**, 201–214.
101 T. L. Skafte, Z. Guan, M. L. Machala, C. B. Gopal, M. Monti, L. Martinez, E. Stamate, S. Sanna, J. A. Garrido Torres, E. J. Crumlin, M. García-Melchor, M. Bajdich, W. C. Chueh and C. Graves, *Nat Energy*, 2019, **4**, 846–855.
102 E. M. Sala, N. Mazzanti, M. B. Mogensen and C. Chatzichristodoulou, *Solid State Ionics*, 2022, **375**, 115833.
103 Z. A. Feng, M. L. Machala and W. C. Chueh, *Phys. Chem. Chem. Phys.*, 2015, **17**, 12273–12281.
104 Z. Zhao, M. Uddi, N. Tsvetkov, B. Yildiz and A. F. Ghoniem, *Phys. Chem. Chem. Phys.*, 2017, **19**, 25774–25785.
105 Z. A. Feng, C. Balaji Gopal, X. Ye, Z. Guan, B. Jeong, E. Crumlin and W. C. Chueh, *Chem. Mater.*, 2016, **28**, 6233–6242.

106 H. Lv, L. Lin, X. Zhang, D. Gao, Y. Song, Y. Zhou, Q. Liu, G. Wang and X. Bao, *J. Mater. Chem. A*, 2019, **7**, 11967–11975.
107 K. T. Bae, I. Jeong, A. Akromjon, H.-N. Im and K. T. Lee, *Chemical Engineering Journal*, 2023, **472**, 145015.
108 T. Tan, Z. Wang, M. Qin, W. Zhong, J. Hu, C. Yang and M. Liu, *Adv Funct Materials*, 2022, 2202878.
109 Y. Zheng, J. Wang, B. Yu, W. Zhang, J. Chen, J. Qiao and J. Zhang, *Chem. Soc. Rev.*, 2017, **46**, 1427–1463.
110 R. Xing, Y. Wang, Y. Zhu, S. Liu and C. Jin, *Journal of Power Sources*, 2015, **274**, 260–264.
111 S. Wang, B. Qian, Y. Tang, Q. Ni, Y. Zheng, H. Chen, L. Ge and H. Yang, *Electrochimica Acta*, 2023, **439**, 141659.
112 T. Li, T. Wang, T. Wei, X. Hu, Z. Ye, Z. Wang, D. Dong, B. Chen, H. Wang and Z. Shao, *Small*, 2021, **17**, 2007211.
113 M. Wang, N. Li, Q. Shen, Z. Zhan and C. Chen, *Sustainable Energy Fuels*, 2022, **6**, 2038–2044.
114 L. Ye, K. Zhu, Y. Jiang, S. Zhang, R. Peng and C. Xia, *J. Mater. Chem. A*, 2023, **11**, 10646–10658.
115 K. Amarsingh Bhabu, J. Theerthagiri, J. Madhavan, T. Balu, G. Muralidharan and T. R. Rajasekaran, *J Mater Sci: Mater Electron*, 2016, **27**, 1566–1573.
116 A. Ashok, A. Kumar, J. Ponraj, S. A. Mansour and F. Tarlochan, *J. Electrochem. Soc.*, 2018, **165**, J3301–J3309.
117 H. Uchida, E. H. Da'as, H. Nishino, R. Ramachandran, Y. Takahashi and Y. Yamada, *ECS Trans.*, 2023, **111**, 737–742.
118 W. Wattanathana, C. Veranitisagul, S. Wannapaiboon, W. Klysubun, N. Koonsaeng and A. Laobuthee, *Ceramics International*, 2017, **43**, 9823–9830.
119 Y. Xiao, P. Zhang, X. Zhang, X. Dai, Y. Ma, Y. Wang, Y. Jiang, M. Liu and Y. Wang, *J. Mater. Chem. A*, 2017, **5**, 15901–15912.
120 Z. Hao, J. Shen, S. Lin, X. Han, X. Chang, J. Liu, M. Li and X. Ma, *Applied Catalysis B: Environmental*, 2021, **286**, 119922.
121 F. Liu, D. Diercks, A. M. Hussain, N. Dale, Y. Furuya, Y. Miura, Y. Fukuyama and C. Duan, *ACS Appl. Mater. Interfaces*, 2022, **14**, 53840–53849.
122 Y. Tian, L. Zhang, Y. Liu, L. Jia, J. Yang, B. Chi, J. Pu and J. Li, *J. Mater. Chem. A*, 2019, **7**, 6395–6400.
123 Y. Li, Y. Li, S. Zhang, C. Ren, Y. Jing, F. Cheng, Q. Wu, P. Lund and L. Fan, *ACS Appl. Mater. Interfaces*, 2022, **14**, 9138–9150.
124 S. Zhang, Y. Jiang, H. Han, Y. Li and C. Xia, *ACS Appl. Mater. Interfaces*, 2022, **14**, 28854–28864.
125 X. Sun, Y. Ye, M. Zhou, H. Chen, Y. Li, P. Chen, D. Dong, Y. Ling, M. Khan and Y. Chen, *J. Mater. Chem. A*, 2022, **10**, 2327–2335.
126 A. Wu, M. Xiong, Y. Zhang, S. Hanson, J. Wang, W. Guan and S. C. Singhal, *Chemical Engineering Journal*, 2023, **466**, 143275.
127 M. B. Mogensen, M. Chen, H. L. Frandsen, C. Graves, J. B. Hansen, K. V. Hansen, A. Hauch, T. Jacobsen, S. H. Jensen, T. L. Skafte and X. Sun, *Clean Energy*, 2019, **3**, 175–201.
128 M. Perez and R. Perez, *Solar Energy Advances*, 2022, **2**, 100014.

129 D. Udomsilp, J. Rechberger, R. Neubauer, C. Bischof, F. Thaler, W. Schafbauer, N. H. Menzler, L. G. J. de Haart, A. Nenning, A. K. Opitz, O. Guillon and M. Bram, *Cell Reports Physical Science*, 2020, **1**, 100072.
130 B. Tanç, H. T. Arat, E. Baltacıoğlu and K. Aydın, *International Journal of Hydrogen Energy*, 2019, **44**, 10120–10128.
131 Z. P. Cano, D. Banham, S. Ye, A. Hintennach, J. Lu, M. Fowler and Z. Chen, *Nat Energy*, 2018, **3**, 279–289.
132 A. Ajanovic and R. Haas, *International Journal of Hydrogen Energy*, 2021, **46**, 10049–10058.
133 J. Shin, W.-S. Hwang and H. Choi, *Technological Forecasting and Social Change*, 2019, **143**, 239–248.
134 J. Rechberger, A. Kaupert, J. Hagerskans and L. Blum, *Transportation Research Procedia*, 2016, **14**, 3676–3685.
135 R. T. Leah, A. Bone, E. Hammer, A. Selcuk, M. Rahman, A. Clare, S. Mukerjee and M. Selby, *ECS Trans.*, 2017, **78**, 87–95.
136 V. V. Krishnan, *WIREs Energy Environ*, 2017, **6**, e246.
137 P. Boldrin and N. P. Brandon, *Nat Catal*, 2019, **2**, 571–577.
138 M. C. Tucker, *International Journal of Hydrogen Energy*, 2020, **45**, 24203–24218.
139 M. M. Welander, B. Hu and M. C. Tucker, *International Journal of Hydrogen Energy*, 2023, **48**, 21578–21585.
140 F. Shen, R. Wang and M. C. Tucker, *Journal of Power Sources*, 2020, **474**, 228618.
141 F. Shen, M. Reisert, R. Wang, P. Singh and M. C. Tucker, *ACS Appl. Energy Mater.*, 2022, **5**, 9383–9391.
142 D. Huan, N. Shi, L. Zhang, W. Tan, Y. Xie, W. Wang, C. Xia, R. Peng and Y. Lu, *ACS Appl. Mater. Interfaces*, 2018, **10**, 1761–1770.
143 M. Jo, H. Bae, K. Park, M. Asif Hamayun, G.-M. Park, J. H. Kim, K. T. Lee, K.-S. Lee, S.-J. Song and J.-Y. Park, *Chemical Engineering Journal*, 2023, **451**, 138954.
144 Y. Li, B. Hu, C. Xia, W. Q. Xu, J. P. Lemmon and F. Chen, *J. Mater. Chem. A*, 2017, **5**, 20833–20842.
145 Y. Li, Y. Li, Y. Wan, Y. Xie, J. Zhu, H. Pan, X. Zheng and C. Xia, *Adv. Energy Mater.*, 2019, **9**, 1803156.
146 X. Xi, Y. Fan, J. Zhang, J.-L. Luo and X.-Z. Fu, *J. Mater. Chem. A*, 2022, **10**, 2509–2518.
147 H. Lv, L. Lin, X. Zhang, R. Li, Y. Song, H. Matsumoto, N. Ta, C. Zeng, Q. Fu, G. Wang and X. Bao, *Nat Commun*, 2021, **12**, 5665.
148 M. Jouny, W. Luc and F. Jiao, *Nat Catal*, 2018, **1**, 748–755.
149 Y. Numata, K. Nakajima, H. Takasu and Y. Kato, *ISIJ Int.*, 2019, **59**, 628–633.
150 S. Wang, A. Inoishi, J. Hong, Y. Ju, H. Hagiwara, S. Ida and T. Ishihara, *J. Mater. Chem. A*, 2013, **1**, 12455.
151 H. Lv, T. Liu, X. Zhang, Y. Song, H. Matsumoto, N. Ta, C. Zeng, G. Wang and X. Bao, *Angew. Chem. Int. Ed.*, 2020, **59**, 15968–15973.
152 H. Lv, L. Lin, X. Zhang, R. Li, Y. Song, H. Matsumoto, N. Ta, C. Zeng, Q. Fu, G. Wang and X. Bao, *Nat Commun*, 2021, **12**, 5665.
153 B. Pang, S. Hu, L. Zhang, P. Zhang, X. Zhu and W. Yang, *ACS Sustainable Chem. Eng.*, 2022, **10**, 11969–11976.
154 D. He, W. Ruan, J. Li, J. Ni and C. Ni, *Chemical Engineering Journal*, 2022, **433**, 133632.
155 X. Hu and K. Xie, *Journal of Power Sources*, 2019, **430**, 20–24.

156 H. Seong, M. Choi, S. Park, H. Kim, J. Kim, W. Kim, J. S. Yoo and D. Lee, *ACS Energy Lett.*, 2022, **7**, 4177–4184.
157 Y. Liu, Y. Bai and J. Liu, *J. Electrochem. Soc.*, 2013, **160**, F13–F17.
158 W. Zhang and Y. H. Hu, *Energy Science & Engineering*, 2023, **11**, 3276–3288.
159 G. Wang, J. Chen, Y. Ding, P. Cai, L. Yi, Y. Li, C. Tu, Y. Hou, Z. Wen and L. Dai, *Chem. Soc. Rev.*, 2021, **50**, 4993–5061.
160 S. Jin, Z. Hao, K. Zhang, Z. Yan and J. Chen, *Angewandte Chemie*, 2021, **133**, 20795–20816.
161 T. Burdyny and W. A. Smith, *Energy Environ. Sci.*, 2019, **12**, 1442–1453.
162 S. Hu, L. Zhang, L. Cai, Z. Cao, Q. Jiang, W. Yu, Y. Wu, X. Zhu and W. Yang, *J. Mater. Chem. A*, 2020, **8**, 21053–21061.
163 B. Pan, J. Fan, J. Zhang, Y. Luo, C. Shen, C. Wang, Y. Wang and Y. Li, *ACS Energy Lett.*, 2022, **7**, 4224–4231.
164 Z. Teng, Z. Xiao, G. Yang, L. Guo, X. Yang, R. Ran, W. Wang, W. Zhou and Z. Shao, *Materials Today Energy*, 2020, **17**, 100458.
165 T. Chen, Y. Zhou, M. Liu, C. Yuan, X. Ye, Z. Zhan and S. Wang, *Electrochemistry Communications*, 2015, **54**, 23–27.
166 G. Li, Y. Gou, X. Cheng, Z. Bai, R. Ren, C. Xu, J. Qiao, W. Sun, Z. Wang and K. Sun, *ACS Appl. Mater. Interfaces*, 2021, **13**, 34282–34291.
167 Z. Li, B. Yang, B. Qian, S. Wang, Y. Zheng, L. Ge and H. Chen, *Separation and Purification Technology*, 2023, **308**, 123002.
168 K. T. Bae, I. Jeong, D. Kim, H. Yu, H.-N. Im, A. Akromjon, C.-W. Lee and K. T. Lee, *Chemical Engineering Journal*, 2023, **461**, 142051.
169 T. Liu, Y. Wang, Y. Zhang, S. Fang, L. Lei, C. Ren and F. Chen, *Electrochemistry Communications*, 2015, **61**, 106–109.
170 D. Kim, J. W. Park, M. S. Chae, I. Jeong, J. H. Park, K. J. Kim, J. J. Lee, C. Jung, C.-W. Lee, S.-T. Hong and K. T. Lee, *J. Mater. Chem. A*, 2021, **9**, 5507–5521.
171 Y. Tan, A. Wang, L. Jia, D. Yan, B. Chi, J. Pu and J. Li, *International Journal of Hydrogen Energy*, 2017, **42**, 4456–4464.
172 D. Heidari, S. Javadpour and S. H. Chan, *Energy Conversion and Management*, 2017, **136**, 78–84.
173 M. A. Laguna-Bercero, H. Monzón, A. Larrea and V. M. Orera, *J. Mater. Chem. A*, 2016, **4**, 1446–1453.
174 M.-B. Choi, B. Singh, E. D. Wachsman and S.-J. Song, *Journal of Power Sources*, 2013, **239**, 361–373.
175 H.-J. Choi, Y.-H. Na, M. Kwak, T. W. Kim, D.-W. Seo, S.-K. Woo and S.-D. Kim, *Ceramics International*, 2017, **43**, 13653–13660.
176 K. J. Kim, I. Thaheem, I. Jeong, H. Yu, J. H. Park and K. T. Lee, *Journal of Power Sources*, 2022, **539**, 231611.
177 Y. Tian, W. Wang, Y. Liu, L. Zhang, L. Jia, J. Yang, B. Chi, J. Pu and J. Li, *ACS Appl. Energy Mater.*, 2019, **2**, 3297–3305.
178 Z. Yue, L. Jiang, Z. Chen, N. Ai, Y. Zou, S. P. Jiang, C. Guan, X. Wang, Y. Shao, H. Fang, Y. Luo and K. Chen, *ACS Appl. Mater. Interfaces*, 2023, **15**, 8138–8148.
179 Y. Tian, W. Wang, Y. Liu, A. Naden, M. Xu, S. Wu, B. Chi, J. Pu and J. T. S. Irvine, *ACS Catal.*, 2021, **11**, 3704–3714.

180 X. Xi, Z.-S. Cao, X.-Q. Shen, Y. Lu, J. Li, J.-L. Luo and X.-Z. Fu, *Journal of Power Sources*, 2020, **459**, 228071.
181 K.-Y. Lai and A. Manthiram, *Chem. Mater.*, 2018, **30**, 2515–2525.
182 O. Kwon, S. Sengodan, K. Kim, G. Kim, H. Y. Jeong, J. Shin, Y.-W. Ju, J. W. Han and G. Kim, *Nat Commun*, 2017, **8**, 15967.
183 C. Yang, J. Li, Y. Lin, J. Liu, F. Chen and M. Liu, *Nano Energy*, 2015, **11**, 704–710.
184 S. Sengodan, S. Choi, A. Jun, T. H. Shin, Y.-W. Ju, H. Y. Jeong, J. Shin, J. T. S. Irvine and G. Kim, *Nature Mater*, 2015, **14**, 205–209.
185 Z. Wang, Z. Wang, W. Yang, R. Peng and Y. Lu, *Journal of Power Sources*, 2014, **255**, 404–409.
186 L. Yang, Y. Choi, W. Qin, H. Chen, K. Blinn, M. Liu, P. Liu, J. Bai, T. A. Tyson and M. Liu, *Nat Commun*, 2011, **2**, 357.
187 Z. Zhan and S. Barnett, *Solid State Ionics*, 2005, **176**, 871–879.
188 L. Zhang, C. Yang, A. I. Frenkel, S. Wang, G. Xiao, K. Brinkman and F. Chen, *Journal of Power Sources*, 2014, **262**, 421–428.
189 M. Qin, T. Tan, K. Li, Z. Wang, H. Yang, Z. Liu, M. Zhou, T. Liu, C. Yang and M. Liu, *International Journal of Hydrogen Energy*, 2020, **45**, 21464–21472.
190 J. Nielsen, Å. H. Persson, T. T. Muhl and K. Brodersen, *J. Electrochem. Soc.*, 2018, **165**, F90–F96.
191 E. Dogdibegovic, Y. Fukuyama and M. C. Tucker, *Journal of Power Sources*, 2020, **449**, 227598.
192 M. Li, K. Chen, B. Hua, J. Luo, W. D. A. Rickard, J. Li, J. T. S. Irvine and S. P. Jiang, *J. Mater. Chem. A*, 2016, **4**, 19019–19025.
193 Z. Gao, D. Kennouche and S. A. Barnett, *Journal of Power Sources*, 2014, **260**, 259–263.
194 J. S. Cronin, Y. K. Chen-Wiegart, J. Wang and S. A. Barnett, *Journal of Power Sources*, 2013, **233**, 174–179.
195 Y. Chen, Y. Chen, D. Ding, Y. Ding, Y. Choi, L. Zhang, S. Yoo, D. Chen, B. deGlee, H. Xu, Q. Lu, B. Zhao, G. Vardar, J. Wang, H. Bluhm, E. J. Crumlin, C. Yang, J. Liu, B. Yildiz and M. Liu, *Energy Environ. Sci.*, 2017, **10**, 964–971.
196 Z. Duan, M. Yang, A. Yan, Z. Hou, Y. Dong, Y. Chong, M. Cheng and W. Yang, *Journal of Power Sources*, 2006, **160**, 57–64.
197 H. A. Ishfaq, M. Z. Khan, Y. M. Shirke, S. Qamar, A. Hussain, M. T. Mehran, R.-H. Song and M. Saleem, *Applied Catalysis B: Environmental*, 2023, **323**, 122178.
198 J. Huang, Q. Liu, S. P. Jiang, L. Zhao, N. Ai, X. Wang, Y. Shao, C. Guan, H. Fang, Y. Luo and K. Chen, *Applied Catalysis B: Environmental*, 2023, **321**, 122080.
199 Z. Li, B. Guan, F. Xia, J. Nie, W. Li, L. Ma, W. Li, L. Zhou, Y. Wang, H. Tian, J. Luo, Y. Chen, M. Frost, K. An and X. Liu, *ACS Appl. Mater. Interfaces*, 2022, **14**, 24363–24373.
200 K. Xu, K. Pei, B. Zhao, Y. Zhao, Q. Niu and Y. Chen, *International Journal of Hydrogen Energy*, 2021, **46**, 32242–32249.
201 Y. Liu, Y. Tian, Y. Wang, Y. Li, J. Pu, F. Ciucci and B. Chi, *Electrochimica Acta*, 2022, **430**, 141032.
202 J. Kim, S. Im, S. H. Oh, J. Y. Lee, K. J. Yoon, J.-W. Son, S. Yang, B.-K. Kim, J.-H. Lee, H.-W. Lee, J.-H. Lee and H.-I. Ji, *Sci. Adv.*, 2021, **7**, eabj8590.
203 A. Nechache, F. Han, R. Semerad, G. Schiller and R. Costa, *ECS Trans.*, 2017, **78**, 3039–3047.
204 G. Schiller, A. Ansar, M. Lang and O. Patz, *J Appl Electrochem*, 2009, **39**, 293–301.

205 S.-H. Wu and Y.-N. Cheng, *Performance Test for Anode-Supported And Metal-Supported Solid Oxide Electrolysis Cell Under Different Current Densities*, .
206 X. Yue and J. T. S. Irvine, *J. Mater. Chem. A*, 2017, **5**, 7081–7090.
207 C. Xu, S. Zhen, R. Ren, H. Chen, W. Song, Z. Wang, W. Sun and K. Sun, *Chem. Commun.*, 2019, **55**, 8009–8012.
208 Y. Li, Y. Li, Y. Wan, Y. Xie, J. Zhu, H. Pan, X. Zheng and C. Xia, *Advanced Energy Materials*, 2019, **9**, 1803156.
209 Y. Li, X. Chen, Y. Yang, Y. Jiang and C. Xia, *ACS Sustainable Chem. Eng.*, 2017, **5**, 11403–11412.
210 O. Costa-Nunes, R. J. Gorte and J. M. Vohs, *Journal of Power Sources*, 2005, **141**, 241–249.
211 M. Homel, T. M. Gür, J. H. Koh and A. V. Virkar, *Journal of Power Sources*, 2010, **195**, 6367–6372.
212 Y. Jiang and A. V. Virkar, *J. Electrochem. Soc.*, 2003, **150**, A942.
213 H. Zhang, J. Chen and J. Zhang, *International Journal of Hydrogen Energy*, 2013, **38**, 16354–16364.
214 L. Bian, L. Wang, C. Duan, C. Cai, X. Song and S. An, *International Journal of Hydrogen Energy*, 2019, **44**, 32210–32218.
215 S. Wang, H. Tsuruta, M. Asanuma and T. Ishihara, *Advanced Energy Materials*, 2015, **5**, 1401003.
216 Z. Yin, H. Peng, X. Wei, H. Zhou, J. Gong, M. Huai, L. Xiao, G. Wang, J. Lu and L. Zhuang, *Energy Environ. Sci.*, 2019, **12**, 2455–2462.
217 T. Zheng, K. Jiang, N. Ta, Y. Hu, J. Zeng, J. Liu and H. Wang, *Joule*, 2019, **3**, 265–278.
218 T. Haas, R. Krause, R. Weber, M. Demler and G. Schmid, *Nat Catal*, 2018, **1**, 32–39.
219 V. Kaplan, E. Wachtel, K. Gartsman, Y. Feldman and I. Lubomirsky, *J. Electrochem. Soc.*, 2010, **157**, B552.

Appendix A - Boosting the performance of reversible solid oxide electrochemical cells with a novel hybrid oxygen electrode, $Pr_{1.39}Ba_{0.14}Sr_{0.53}Co_{1.48}Fe_{0.76}O_{6-\delta}$-$Ba_{0.66}Sr_{0.34}CoO_{3-\delta}$- $Ba_{0.66}Sr_{0.34}CoO_{3-\delta}$

Appendix A Figure A1. XRD patterns of the previous PBSCF-a phase and the hybrid electrode. The previous PBSCF-a is a single-phase double perovskite, which was synthesized by a wet chemistry method and sintered at 900 °C for 5 hours. The hybrid electrode consists of two phases, PBSCF-b and BSC, which was prepared by the same wet chemistry method and sintered at 750-770 °C.

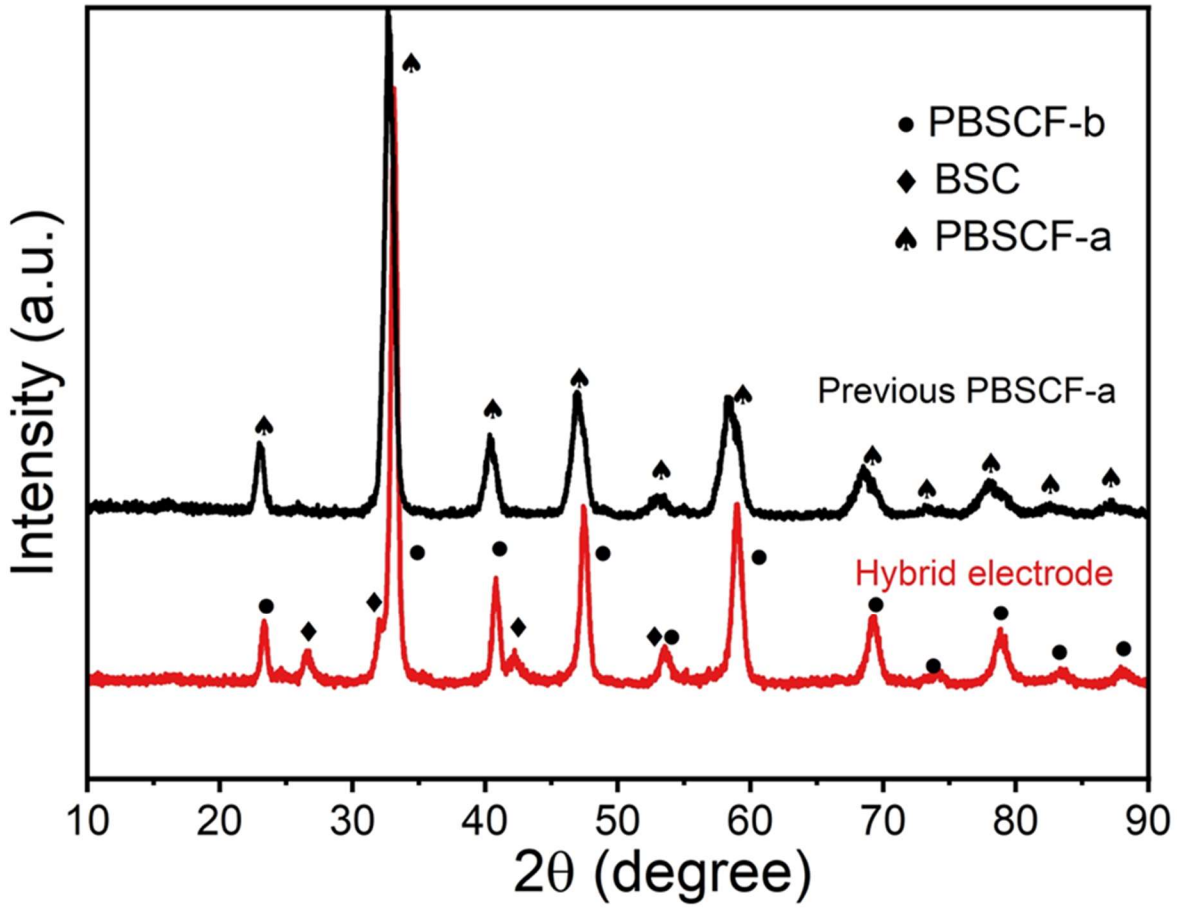

Appendix A Figure A2. (A) TEM images of the hybrid electrode. (B) SAED patterns indicate the hybrid electrode is composed of the PBSCF-b phase and BSC phase. (C) HR-TEM image of the hybrid electrode grain and the zoomed-in areas: (D) and (E). The lattice fringes with the d-spacing of 0.271 nm, correspond to the (102) planes of the new PBSCF-b phase.

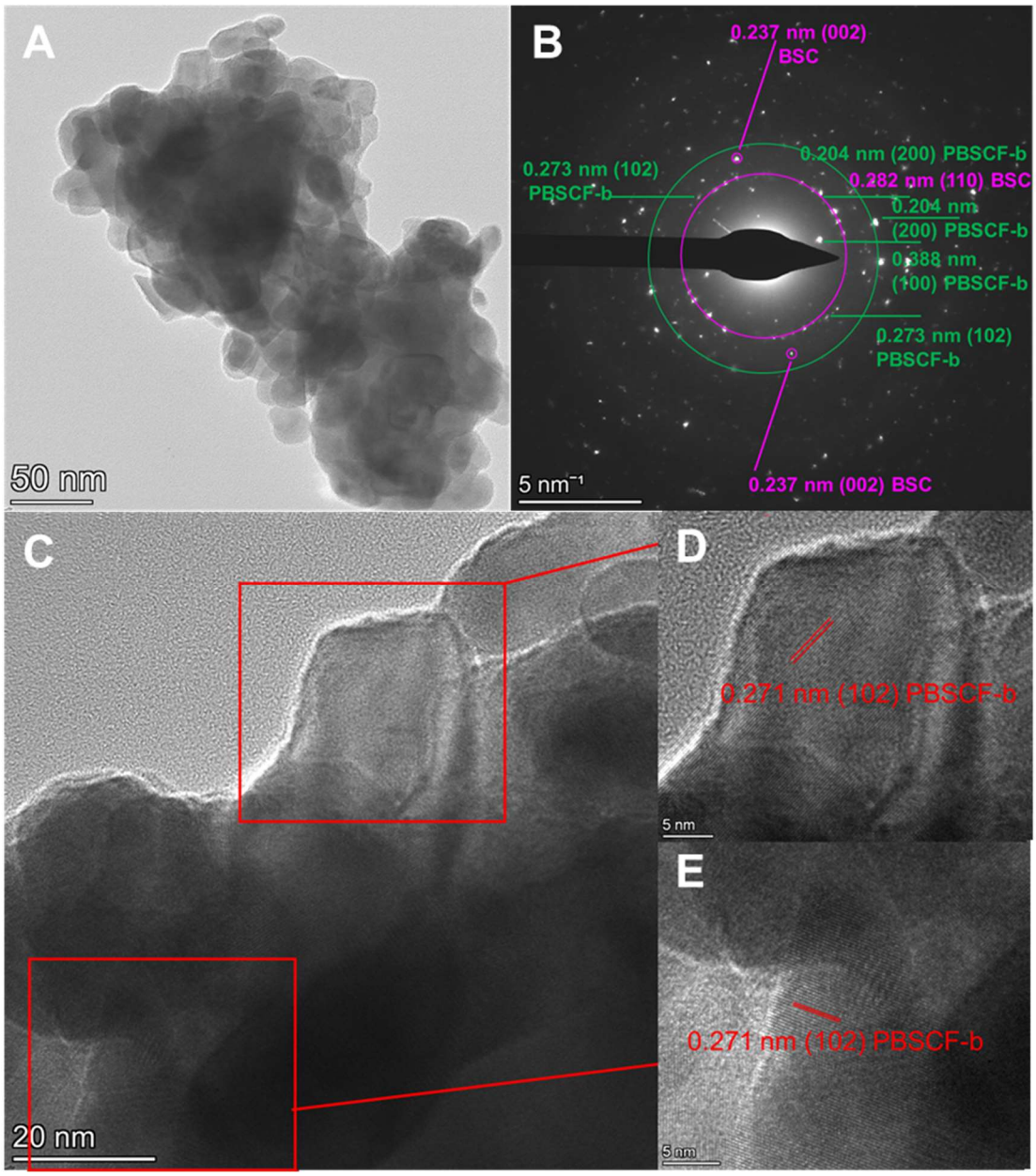

Appendix A Figure A3. (A) Additional TEM images of the hybrid electrode. (B) Additional SAED patterns show the hybrid electrode is composed of a new PBSCF-b phase and the BSC phase. (C) EDS mapping images of the hybrid electrode show the BSC phase mainly contains Ba, Sr, Co, and O elements. (D) HR-TEM image of the hybrid electrode grain and the zoomed-in areas. (E) HR-TEM image shows lattice planes with d-spacing of 0.380 nm, corresponding to the (002) planes of the new PBSCF-b phase)

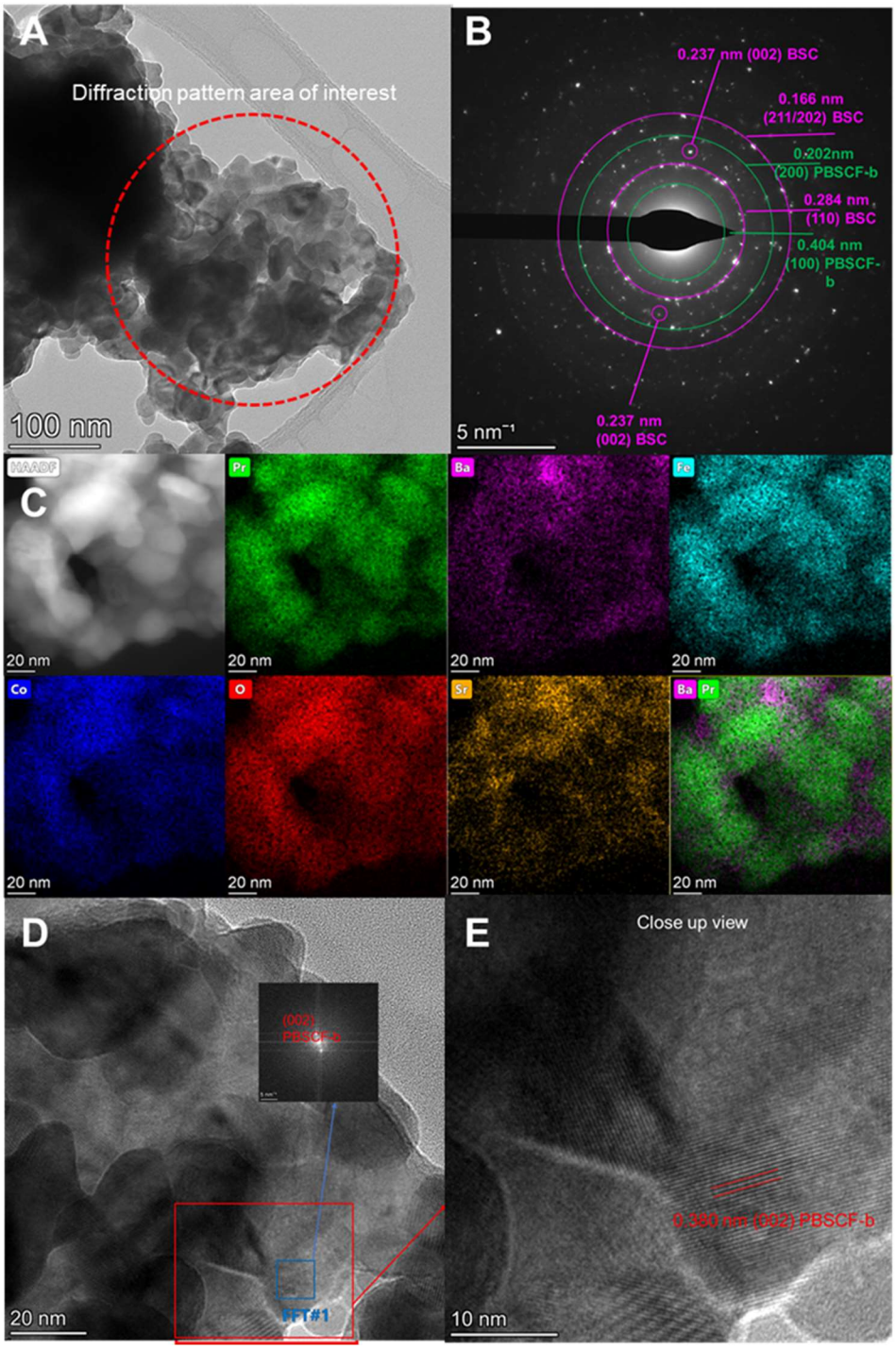

Appendix A Figure A4. (A) TEM image of the hybrid electrode. (B) SAED patterns show the lattices with the d-spacings of 0.382 nm, 0.155 nm, 0.190 nm, 0.270 nm, and 0.219 nm, corresponding to the (002), (212/114), (004), (102/110), and (112) planes of PBSCF-b, respectively. And those with the d-spacing of 0.329 nm and 0.240 nm correspond to the (101) and (200) planes of BSC, respectively. (C) EDS mapping images of the hybrid electrode confirm that it is a composite of PBSCF-b and BSC phases.

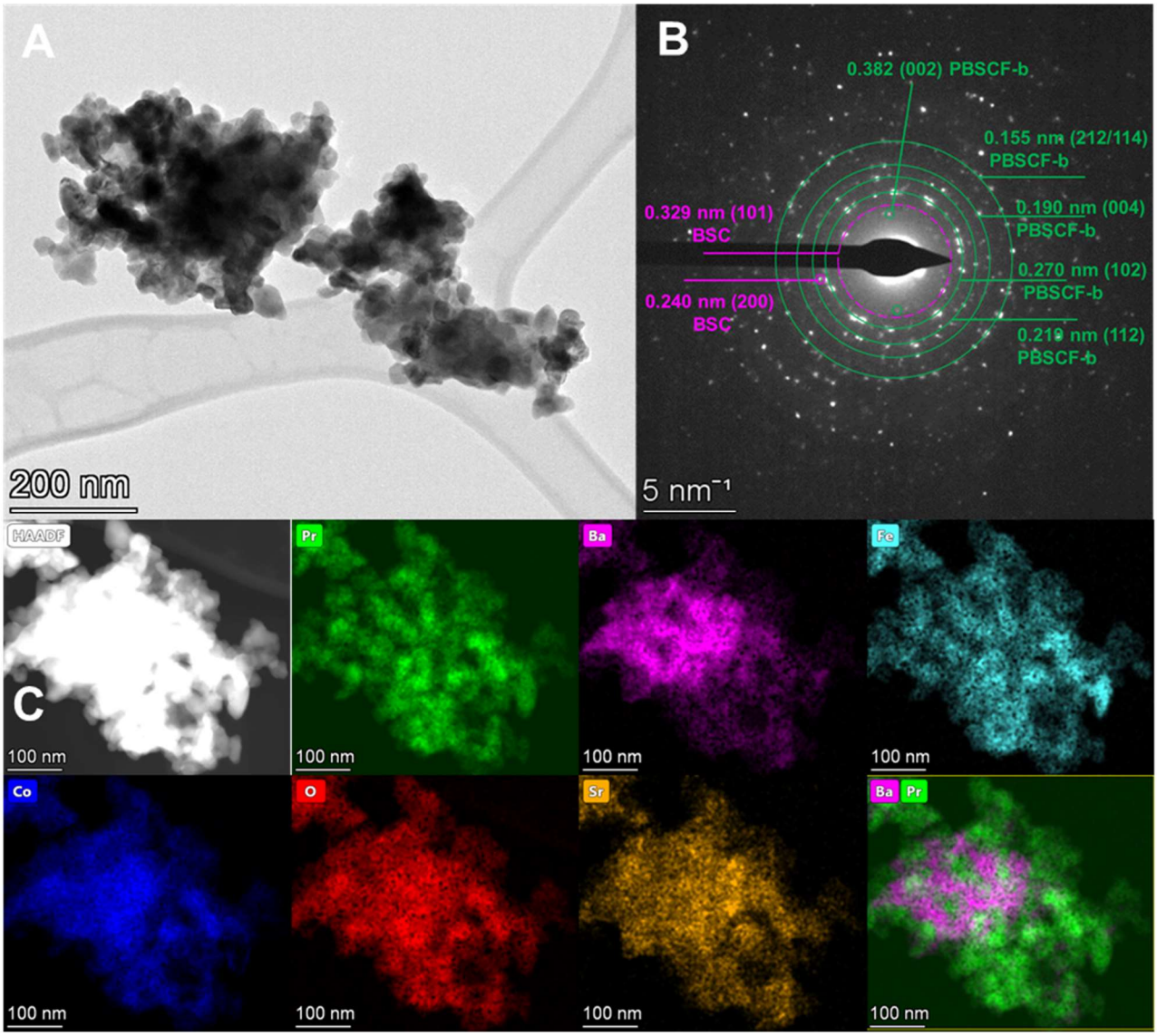

Appendix A Figure A5. ECR experimental results and the fitted results for PBSCF-b coated with BSC at 550 °C, 600 °C, 650 °C, and 700 °C after changing the oxygen partial pressure from 2 vol.% (490 sccm Ar + 10 sccm O_2) to 20 vol.% (400 sccm Ar + 100 sccm O_2).

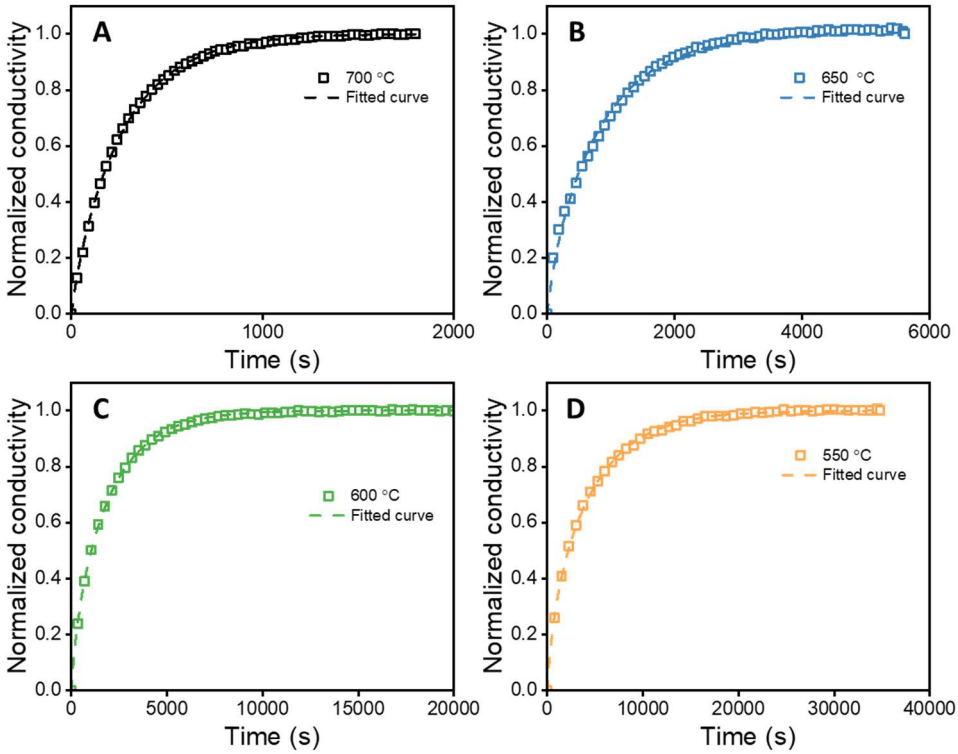

Appendix A Figure A6. ECR experimental results and the fitted results for the previous PBSCF-a at 625 °C, 650 °C, 675 °C, and 700 °C after changing the oxygen partial pressure from 2 vol.% (490 sccm Ar + 10 sccm O_2) to 20 vol.% (400 sccm Ar + 100 sccm O_2).

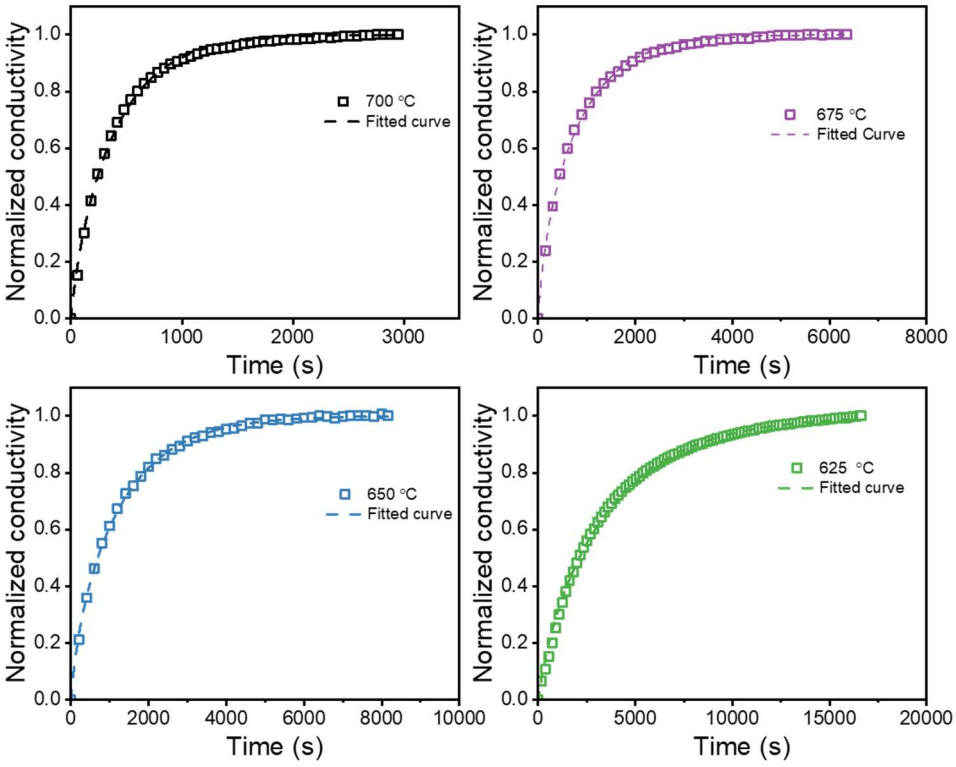

Appendix A Figure A7. Photos of a representative fuel electrode-supported SOEC fabricated in this work to evaluate the oxygen electrodes. The oxygen electrode effective area is 0.5 cm^2.

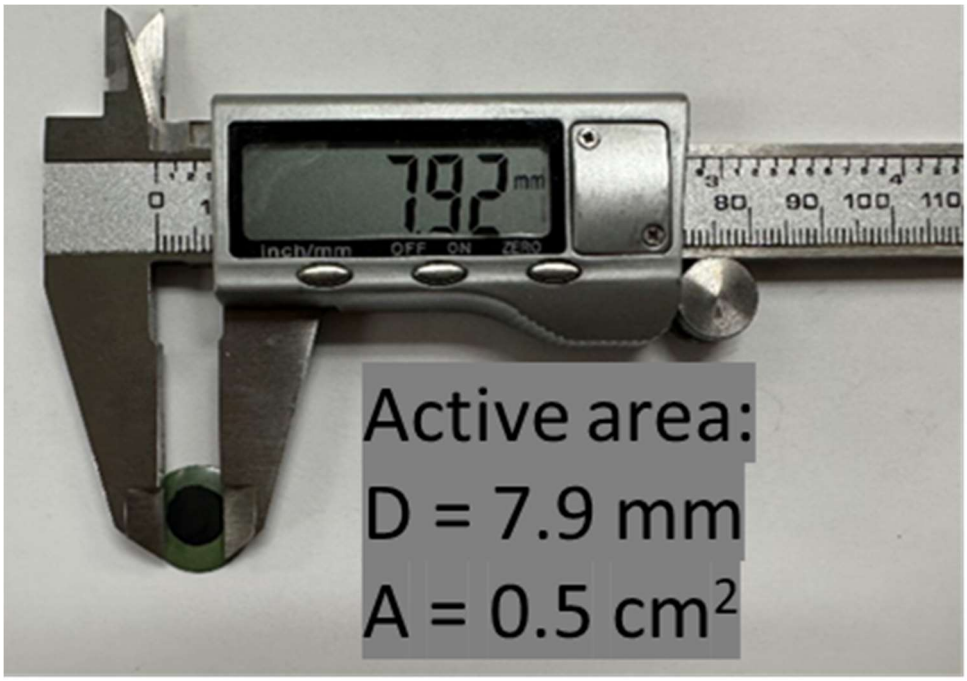

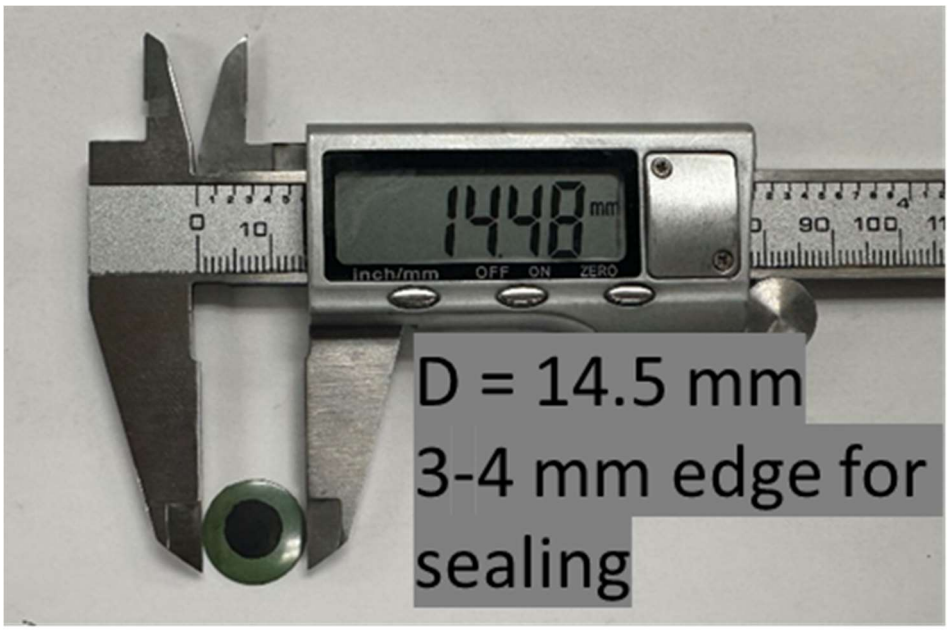

Appendix A Figure A8. Representative SEM images of SOECs studied in this work, which are highly reproducible, highly uniform, and defect-free, and have dense electrolytes (thickness of electrolyte = ~8 μm).

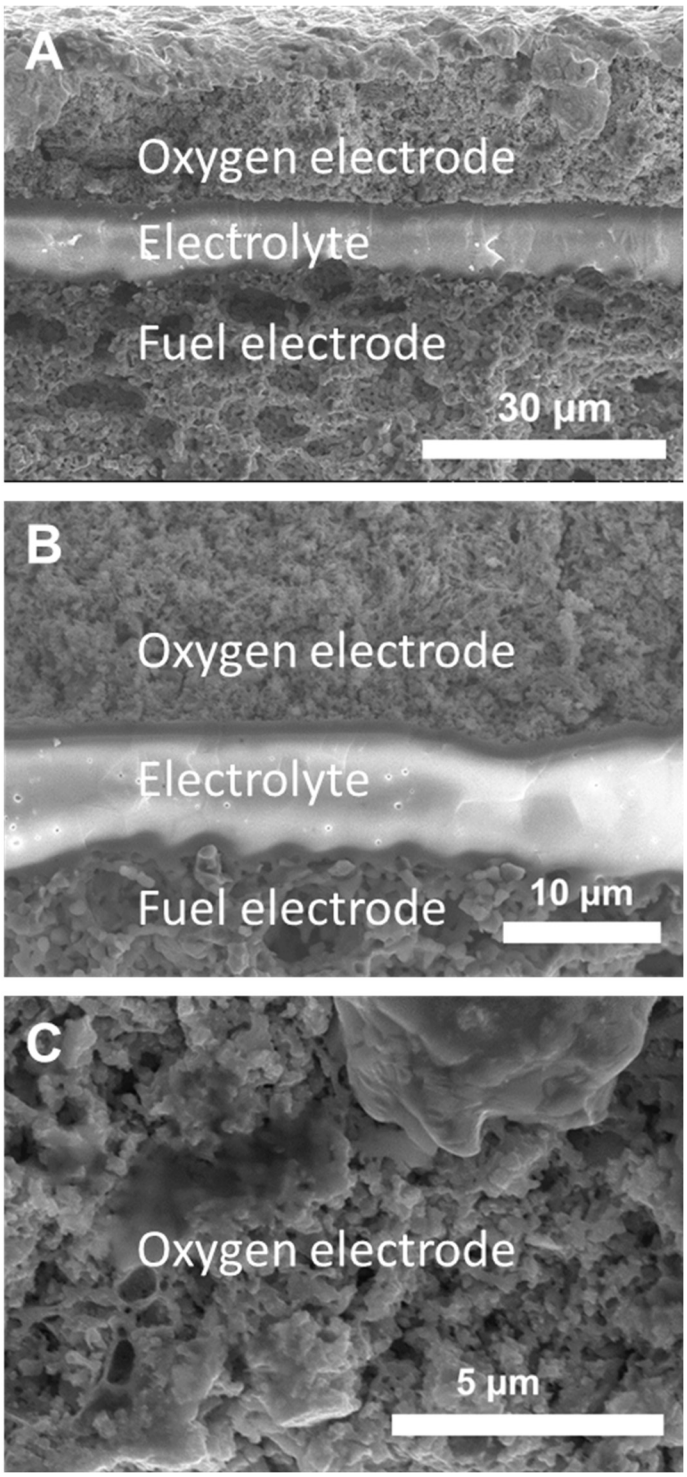

Appendix A Figure A9. SEM images of the SOEC with PBSCF-b+BSC hybrid electrode after performance evaluation in steam electrolysis mode. No cracking or electrolyte-electrode delamination were observed.

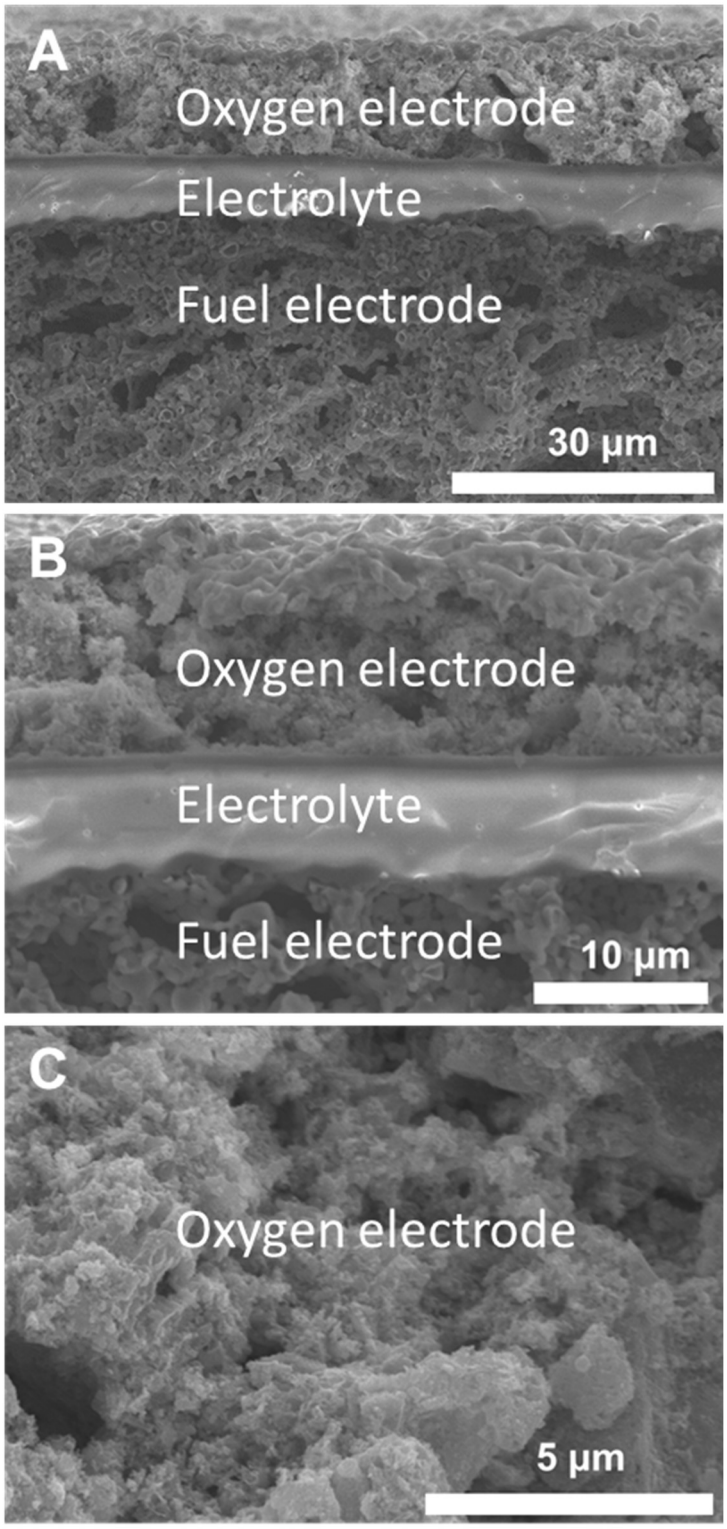

Appendix A Figure A10. EIS spectra collected at an applied voltage of 1.3 V and an operating temperature ranging from 550 to 750 °C for SOEC with the hybrid electrode.

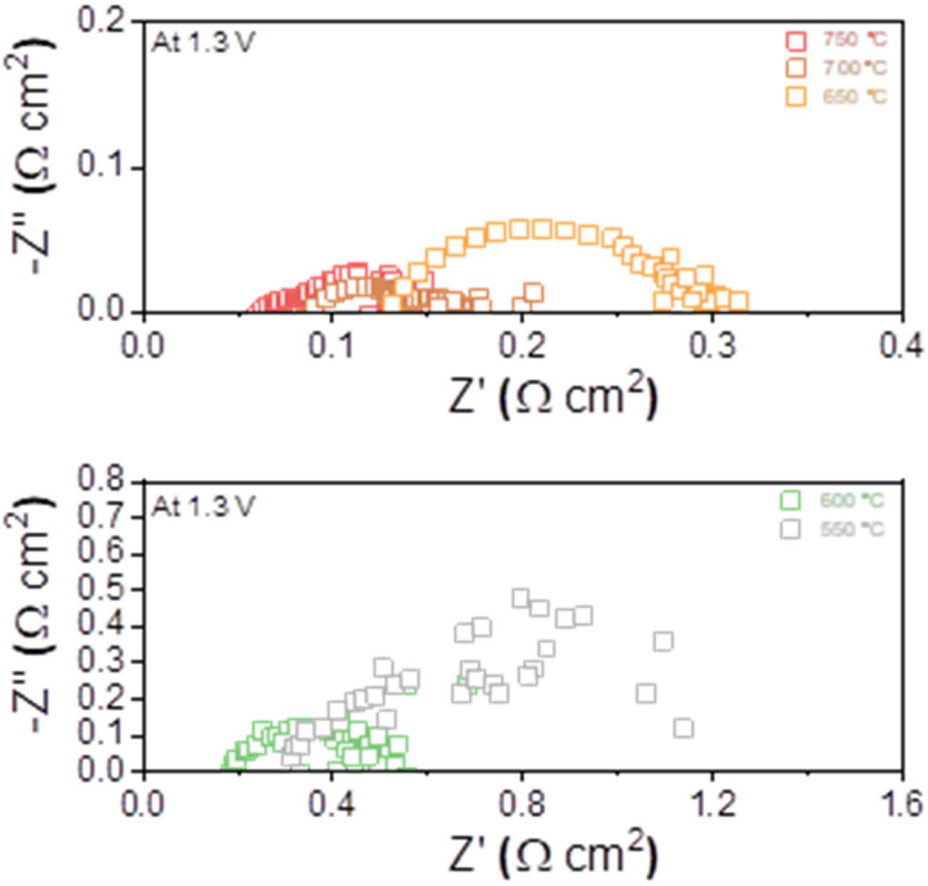

Appendix A Table A1. Comparisons YSZ electrolyte-based SOEC performance.

Half-cell configuration	Oxygen electrode materials	Temperature (°C)	Current densities at 1.3 V (A cm^{-2})	Literature
Ni-YSZ|YSZ	Hybrid electrode	750	4.4	This work
		700	2.3	
		650	1.4	
		600	0.9	
		550	0.46	
Ni-YSZ|YSZ|GDC	SSC-SDC	800	4.08	12
		750	3.13	
		700	1.9	
		650	1.1	
Ni-YSZ|YSZ|GDC	STFC	800	3	16
		750	2.3	
		700	1.5	
		650	1	
		600	0.6	
LSCFN55|YSZ	SSNC	800	0.7	164
		750	0.45	
430L|YSZ|SSZ	SSZ-Nd_2O_3/NNO	800	2.05	165
		750	1.62	
		700	1.06	
		650	0.6	
Ni-YSZ|Ni-SSZ|SSZ|SNDC	PBSCF-GDC	750	2.1	66
		700	1.45	
		650	0.94	
		600	0.51	

Ni-YSZ|YSZ	LSM-DYSB	700	1.32	15
		650	0.9	
		600	0.47	
Ni-YSZ|YSZ|SNDC	LSCF-SNDC	750	1.37	67
		700	0.97	
		650	0.58	
Ni-YSZ|YSZ|GDC	LSCF-GDC	800	2.75	68
		750	1.7	
		700	1.25	
		650	0.6	
Ni-YSZ|YSZ	LSM-YSB	800	1.52	69
		750	0.97	
		700	0.7	
		650	0.46	
Ni-YSZ|YSZ|GDC	STFC-PrOx	800	4.25	59
		750	3.6	
		700	2.9	
		650	2.25	
		600	1.25	
		550	0.5	
Ni-YSZ|YSZ|GDC	PBFZr-GDC	700	2.14	166
Ni-YSZ|YSZ|GDC	LSCF-GDC	750	2.1	70
Ni-YSZ|YSZ|GDC	PBNF0.1	750	0.65	167
Ni-YSZ|YSZ	PBSM3	750	2.75	168
		700	1.85	
Ni-YSZ|YSZ	LSM-YSZ	700	0.40	169

Ni-YSZ|YSZ|GDC	LSCF	700	0.82	[170]
Ni-YSZ|YSZ	LSCF-YSZ	750	0.91	[171]
Ni-YSZ|YSZ|SDC	BSCF-SDC	750	0.23	[172]
Ni-YSZ|YSZ	PNO	700	0.28	[173]
Ni-YSZ|YSZ|GDC	LSCF-GDC	750	0.34	[174]
Ni-YSZ|YSZ|GDC	LSCF-GDC	750	0.77	[175]
Ni-YSZ|ScSZ	Mn1.3Co1.3Cu0.4O4-ScSZ	750	1.4	[176]
Ni-YSZ|YSZ|GDC	LSFN-GDC	750	0.53	[177]
Ni-YSZ|YSZ|GDC	BCO-PBCC	750	1.36	[178]

Appendix A Table A2. Performance comparison of this work and other state-of-the-art YSZ anode-supported hydrogen-fueled SOFCs reported recently.

Half-cell configuration	Oxygen electrode materials	Peak power density at 750 °C (W cm^{-2})	Literature
Ni-YSZ|YSZ	Hybrid electrode	2.4	This work
Ni-YSZ|YSZ|GDC	STFC	1.75	[16]
Ni-YSZ|YSZ|GDC	STFC-PrO_x	3	[59]
Ni-YSZ|YSZ|GDC	LSCF-GDC-PrO_x	2	[57]
Ni-YSZ|YSZ	LSCF-GDC	1.6	[58]
Ni-YSZ|YSZ|GDC	LSF-GDC-Pr_6O_{11}	1.57	[60]
Ni-YSZ|YSZ|GDC	PBFZr-GDC	1.9	[166]
Ni-YSZ|YSZ|GDC	PBCC-GDC	1.74	[31]
Ni-YSZ|YSZ	SCP-GDC	1.4	[28]
Ni-YSZ|YSZ	PBSCF-GDC	1.37	[28]
Ni-YSZ|YSZ	MCO-GDC	0.7	[62]
Ni-YSZ|YSZ	CMO-SDC	0.64	[63]
Ni-YSZ|YSZ|SDC	BCFN/BCO-LSCF	1.4	[57]
Ni-YSZ|YSZ|GDC	BSNM-SDC-Ag	1.3	[64]
Ni-YSZ|YSZ|GDC	SSC-SDC	2.44	[12]
Ni-YSZ|YSZ|ESB	LSM-ESB	1.75	[11]
Ni-YSZ|YSZ|GDC	NBCCF@GDC	1	[179]

Appendix A Table A3. XRD refinement results of the hybrid electrode material.

Sample	Phase	Space group	a, b, c (Å)	α, β, γ (°)	Wt. frac. (%)	Chi	wR_p (%)	R_p (%)	d-spacing
New PBSCF-b+BSC	New PBSCF-b	Tetragonal; P4/mmm	3.88, 3.88, 7.74	90, 90, 90	89.5	1.978	13.68	11.04	0.195 nm, (200); 0.387 nm, (002); 0.273 nm, (102); 0.158 nm, (212);
	BSC	Hexagonal; P63/mmc	5.58, 5.58, 4.63	90, 90, 120	10.5				0.279 nm, (110); 0.167 nm, (202); 0.169 nm, (211); 0.230 nm, (002);

Appendix A Table A4. Comparison in peak power densities at various temperature using different single cell configuration fueled by propane.

Single cell configuration (fuel electrode| electrolyte| oxygen electrode)	Temperature (°C)	Peak power density (W cm^{-2})	Literature
Ni-YSZ|YSZ|Hybrid electrode	750	2.6	This work
	700	1.7	
	650	0.95	
	600	0.54	
	550	0.26	
RP-SFM-SDC|LDC|LSGM|LSCF-SDC	800	0.7	180
	750	0.35	
LSCrFeCo-GDC|LDC|LSGM|LSCF-GDC	800	0.5	181
	750	0.38	
	700	0.18	
L-PBMCO|LDC|LSGM|NBSCF-GDC	800	0.33	182

RP-PSFN-CFA|LDC|LSGM|BCFN	800	0.59	[183]
PBMO|LDC|LSGM|NBSCF-GDC	800	0.75	[184]
	750	0.3	
	700	0.17	
NTO-Ni-YSZ|YSZ|LSM-YSZ	700	0.15	[185]
BaO/Ni-YSZ|YSZ|SDC-LSCF	750	0.9	[186]
Ru-CeO2|PSZ|Ni-YSZ|YSZ|LSCF-GDC	750	0.48	[187]
	700	0.385	
PSCFN-Co-Fe|LSGM|BCFN	800	0.6	[188]
	750	0.32	
RP-PSFR-FRA-GDC|LSGM|LSCF-GDC	800	0.5	[189]
	750	0.25	
	700	0.12	

Appendix A Table A5. Crystal structure results obtained from TEM for the PBSCF-b phase.

Multi.	(h,k,l)	d* / nm^{-1}	Θ_{Scatt} / Deg.	Intens.	Θ_{Bragg} / mRad	V_r [V||nm||e]	V_i [V||nm||e]	Ampli. [V||nm||e]	d / nm	LP factor	s
1	(0,0,0)	0.000	0.000		0.000	12.339	0.935	12.375			
2	(0,0,1)	1.310	0.189	1	1.642	-0.154	0.247	0.291	0.764	0.7636	1
4	(1,0,0)	2.558	0.368	301	3.208	4.917	0.479	4.940	0.391	0.3909	1
2	(0,0,2)	2.619	0.377	561	3.284	9.623	0.699	9.649	0.382	0.3818	4
8	(1,0,1)	2.874	0.413	489	3.604	4.695	0.471	4.719	0.348	0.348	2
4	(1,1,0)	3.617	0.520	1	4.536	0.249	0.256	0.357	0.276	0.2764	2
8	(1,0,2)	3.661	0.527	300	4.591	4.146	0.453	4.170	0.273	0.2731	5
8	(1,1,1)	3.847	0.553	1000	4.824	7.779	0.642	7.806	0.260	0.2599	3
2	(0,0,3)	3.929	0.565	1	4.927	0.266	0.255	0.368	0.255	0.2545	9
8	(1,1,2)	4.466	0.642	2	5.600	0.274	0.252	0.372	0.224	0.2239	6
8	(1,0,3)	4.688	0.674	167	5.879	3.497	0.430	3.523	0.213	0.2133	10
4	(2,0,0)	5.116	0.736	244	6.415	6.259	0.593	6.287	0.195	0.1955	4

2	(0,0,4)	5.238	0.753	114	6.569	6.135	0.589	6.163	0.191	0.1909	16
8	(2,0,1)	5.281	0.759	1	6.622	0.252	0.247	0.353	0.189	0.1894	5
8	(1,1,3)	5.341	0.768	434	6.697	6.034	0.585	6.062	0.187	0.1872	11
8	(2,1,0)	5.720	0.822	98	7.172	2.955	0.408	2.983	0.175	0.1748	5
8	(2,0,2)	5.747	0.826	355	7.207	5.655	0.571	5.684	0.174	0.174	8
8	(1,0,4)	5.830	0.838	93	7.310	2.904	0.405	2.932	0.172	0.1715	17
16	(2,1,1)	5.868	0.844	183	7.358	2.886	0.404	2.915	0.170	0.1704	6
16	(2,1,2)	6.291	0.904	150	7.889	2.700	0.395	2.729	0.159	0.159	9
8	(1,1,4)	6.366	0.915	1	7.983	0.197	0.242	0.312	0.157	0.1571	18
8	(2,0,3)	6.450	0.927	1	8.089	0.192	0.241	0.309	0.155	0.155	13
2	(0,0,5)	6.548	0.941	0	8.211	0.187	0.241	0.305	0.153	0.1527	25
16	(2,1,3)	6.939	0.998	111	8.702	2.444	0.387	2.474	0.144	0.1441	14
8	(1,0,5)	7.030	1.011	54	8.816	2.410	0.385	2.441	0.142	0.1422	26

Appendix A Table A6. Crystal structure results obtained from TEM for the BSC phase.

Multi.	(h,k,l)	d* / nm^{-1}	Θ_{Scatt} / Deg.	Intens.	Θ_{Bragg} / mRad	V_r [V||nm||e]	V_i [V||nm||e]	Ampli. [V||nm||e]	d / nm	LP factor	s
1	(0,0,0)	0.000	0.000		0.000	28.782	2.090	28.858			
6	(1,0,0)	2.084	0.300	168	2.613	4.877	0.693	4.926	0.480	0.480	1
6	(1,1,0)	3.609	0.519	69	4.525	4.112	0.659	4.165	0.277	0.2771	2
6	(2,0,0)	4.167	0.599	1000	5.225	16.942	1.342	16.995	0.240	0.240	4
2	(0,0,2)	4.232	0.609	321	5.307	16.749	1.337	16.805	0.236	0.2363	4
12	(1,0,2)	4.717	0.678	77	5.915	3.482	0.631	3.539	0.212	0.212	5
12	(2,1,0)	5.513	0.793	51	6.913	3.060	0.610	3.121	0.181	0.1814	5
12	(1,1,2)	5.562	0.800	50	6.974	3.036	0.609	3.096	0.180	0.1798	6
12	(2,0,2)	5.939	0.854	783	7.448	12.636	1.197	12.692	0.168	0.1684	8
6	(3,0,0)	6.251	0.899	18	7.838	2.711	0.589	2.775	0.160	0.160	9
24	(2,1,2)	6.950	0.999	51	8.715	2.419	0.579	2.488	0.144	0.1439	9
6	(2,2,0)	7.218	1.038	221	9.051	10.446	1.116	10.506	0.139	0.1386	8
12	(3,1,0)	7.512	1.080	20	9.420	2.210	0.564	2.281	0.133	0.1331	10
12	(3,0,2)	7.548	1.085	20	9.466	2.197	0.563	2.268	0.132	0.1325	13
6	(4,0,0)	8.334	1.198	139	10.451	8.905	1.043	8.966	0.120	0.120	16
12	(2,2,2)	8.367	1.203	275	10.492	8.864	1.041	8.925	0.120	0.1195	12

2	(0,0,4)	8.464	1.217	44	10.614	8.743	1.034	8.804	0.118	0.1181	16
24	(3,1,2)	8.622	1.240	25	10.812	1.855	0.533	1.930	0.116	0.116	14
12	(1,0,4)	8.716	1.253	12	10.930	1.828	0.531	1.904	0.115	0.1147	17
12	(3,2,0)	9.082	1.306	10	11.389	1.728	0.521	1.805	0.110	0.1101	13
12	(1,1,4)	9.201	1.323	10	11.538	1.697	0.517	1.774	0.109	0.1087	18
12	(4,0,2)	9.347	1.344	187	11.721	7.716	0.978	7.778	0.107	0.107	20
12	(2,0,4)	9.434	1.356	181	11.830	7.622	0.973	7.684	0.106	0.106	20
12	(4,1,0)	9.548	1.373	9	11.973	1.610	0.507	1.688	0.105	0.1047	17
24	(3,2,2)	10.020	1.440	14	12.565	1.500	0.494	1.580	0.100	0.0998	17

Appendix A Table A7. Summary of the stability testing results of our SOECs with the hybrid electrode

Operation	**Fuel humidity**	**Current density**	**Temperature**	**Degradation rate**
Discharging	3% humidified H_2	0.8 A cm^{-2}	650 °C	2 mV/h
	3% humidified H_2	0.2 A cm^{-2}	550 °C	1 mV/h
	3% humidified C_3H_8	0.4 A cm^{-2}	600 °C	8 mV/h
Charging	40% humidified H_2	0.8 A cm^{-2}	650 °C	3 mV/h
	40% humidified H_2	3.0 A cm^{-2}	650 °C	8 mV/h
	40% humidified H_2	5.0 A cm^{-2}	750 °C	4 mV/min

Appendix B - Tuning the *in situ* exsolution of Ni-Co alloy nanoparticles on doped ceria for improved performance in CO_2 electrolysis

Appendix B Figure B1. Electrochemical performance of the SOEC with SDCNiCo15 electrode with CO_2/CO = 90/10 fed to the fuel electrode side. (A) I-V curves from 0.9 V to 1.6 V, and (B) Nyquist plots under OCV conditions from 750 °C to 650 °C.

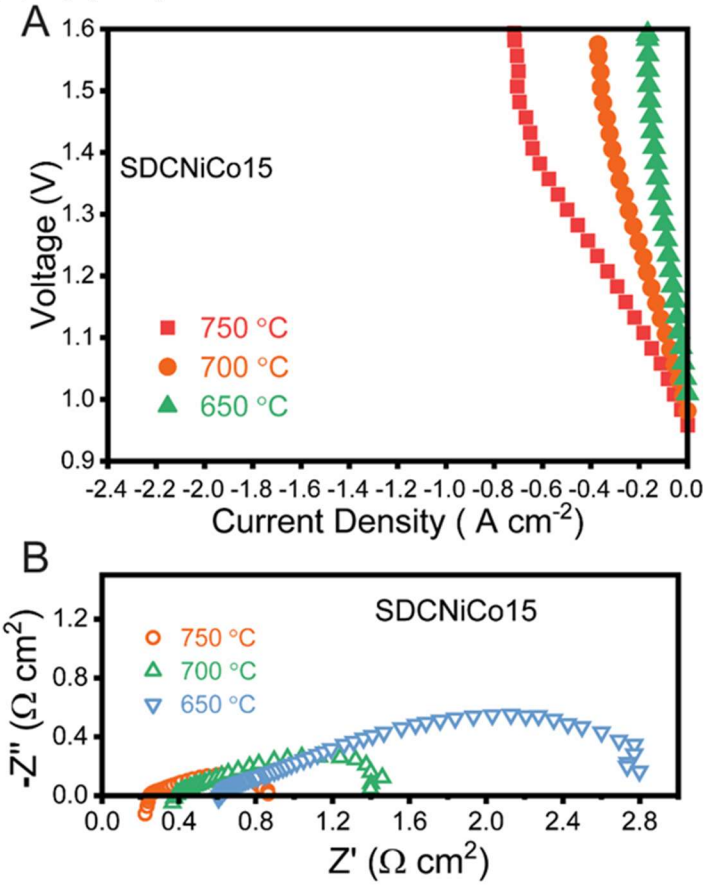

Appendix B Figure B2. Electrochemical performance of the SOEC with SDCNiCo20 electrode with CO_2/CO = 90/10 fed to the fuel electrode side. (A) I-V curves from 0.9 V to 1.6 V, and (B) Nyquist plots under OCV conditions from 750 °C to 650 °C.

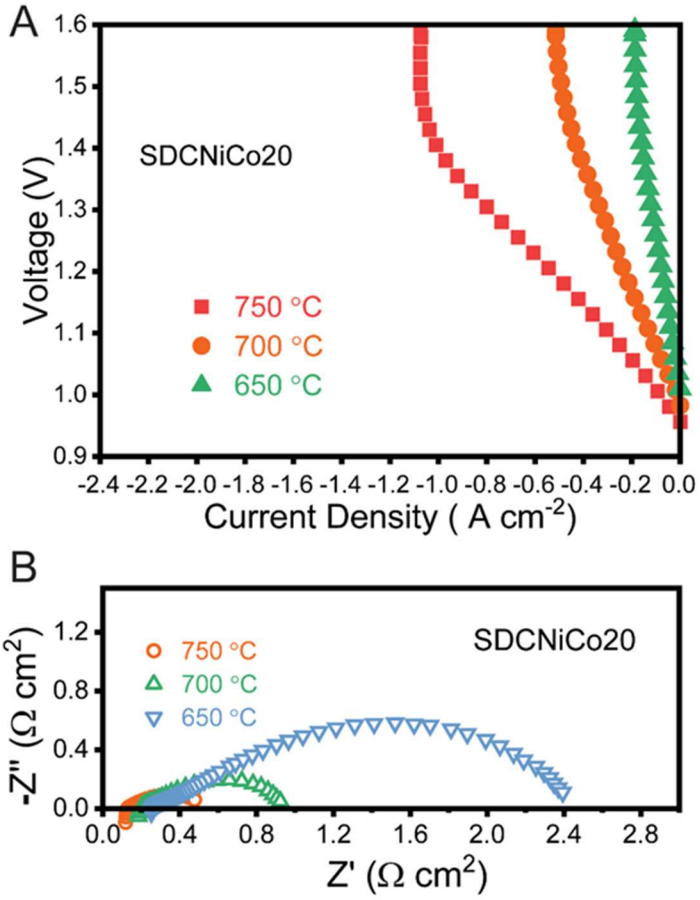

Appendix B Figure B3. Electrochemical performance of the SOEC with SDCNiCo30 electrode with CO_2/CO = 90/10 fed to the fuel electrode side. (A) I-V curves from 0.8 V to 1.6 V, and (B) Nyquist plots under OCV conditions from 750 °C to 650 °C.

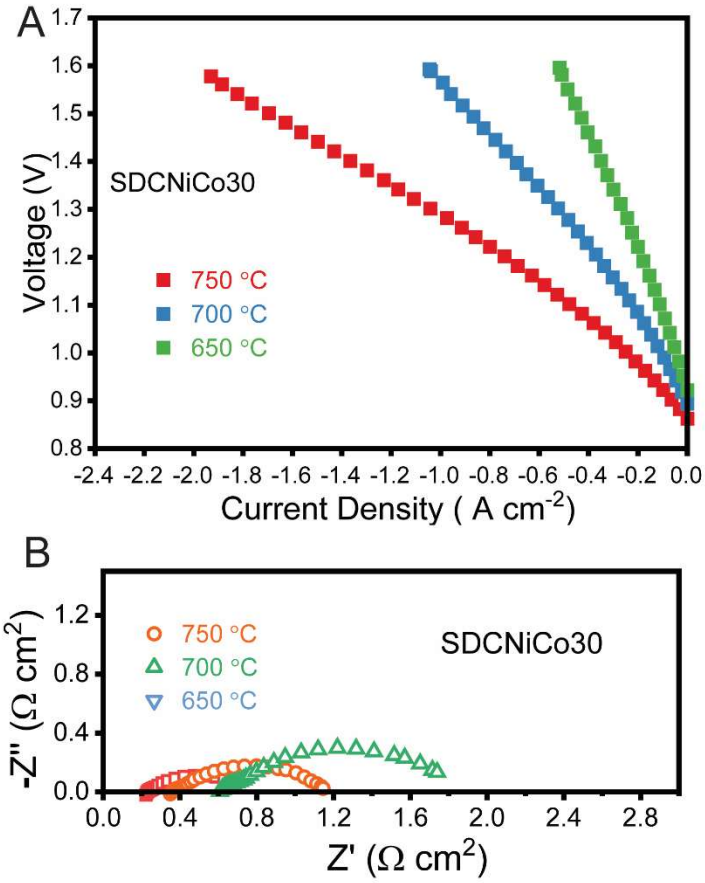

Appendix B Figure B4. Electrochemical performance of the SOFC/SOEC with SDCNi25 electrode. (A) I-V-P curves, and (C) Nyquist plots under OCV conditions from 750 °C to 650 °C with dry hydrogen fed to the fuel electrode side. (B) I-V curves from 0.8 V to 1.6 V, and (D) Nyquist plots under OCV conditions from 750 °C to 650 °C with CO_2/CO = 90/10 fed to the fuel electrode side.

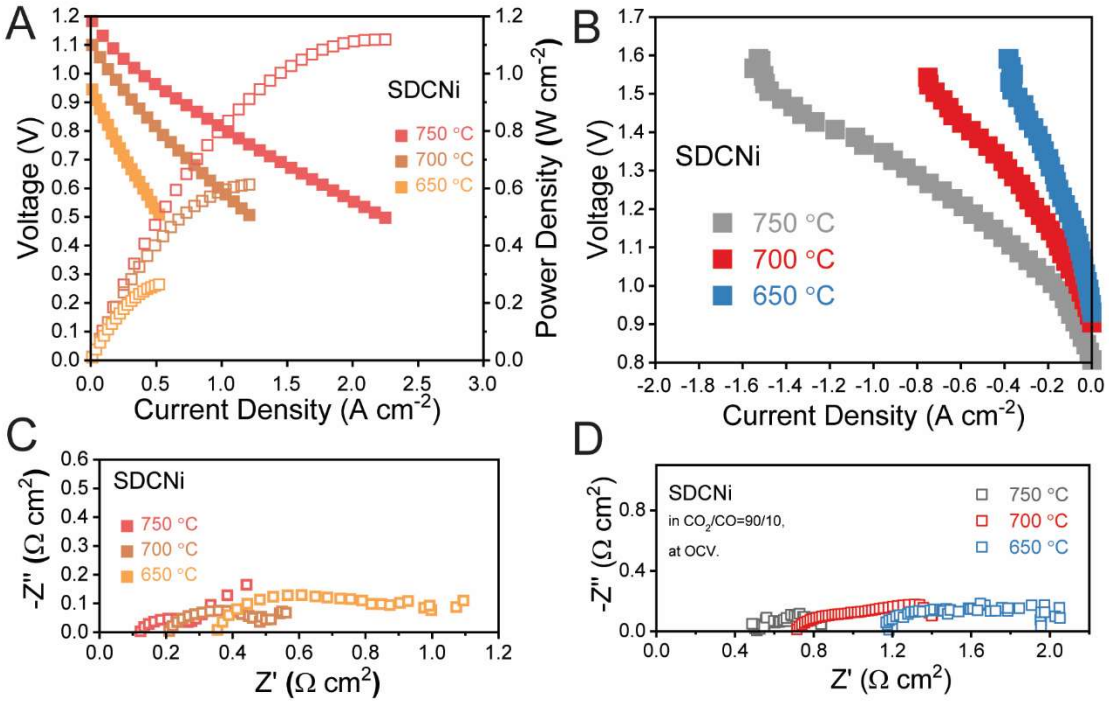

Appendix B Figure B5. Electrochemical performance of the SOFC/SOEC with SDCCo25 electrode. (A) I-V-P curves, and (C) Nyquist plots under OCV conditions from 750 °C to 650 °C with dry hydrogen fed to the fuel electrode side. (B) I-V curves from 0.8 V to 1.6 V, and (D) Nyquist plots under OCV conditions from 750 °C to 650 °C with CO_2/CO = 90/10 fed to the fuel electrode side.

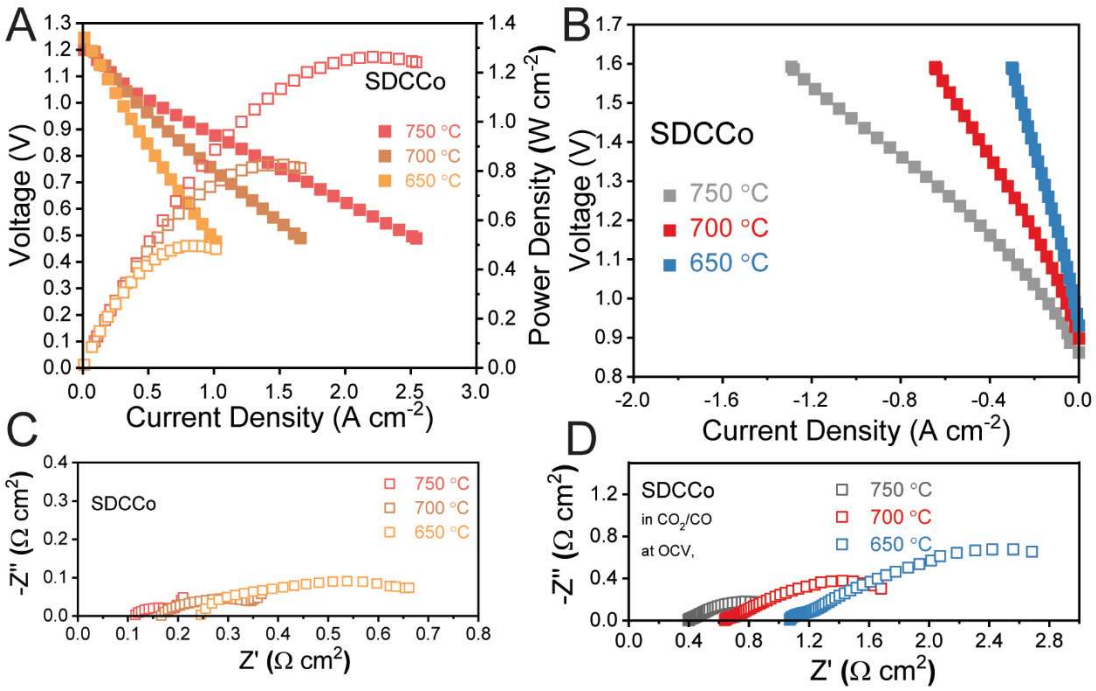

Appendix C - High-performance reversible solid oxide cells for powering electric vehicles, long-term energy storage, and CO_2 conversion

Appendix C Figure C1. MS-SOFC Performance in H_2. (A) Nyquist curves at applied voltages of 0.8 V. (B) Nyquist curves at applied voltages of 0.9 V.

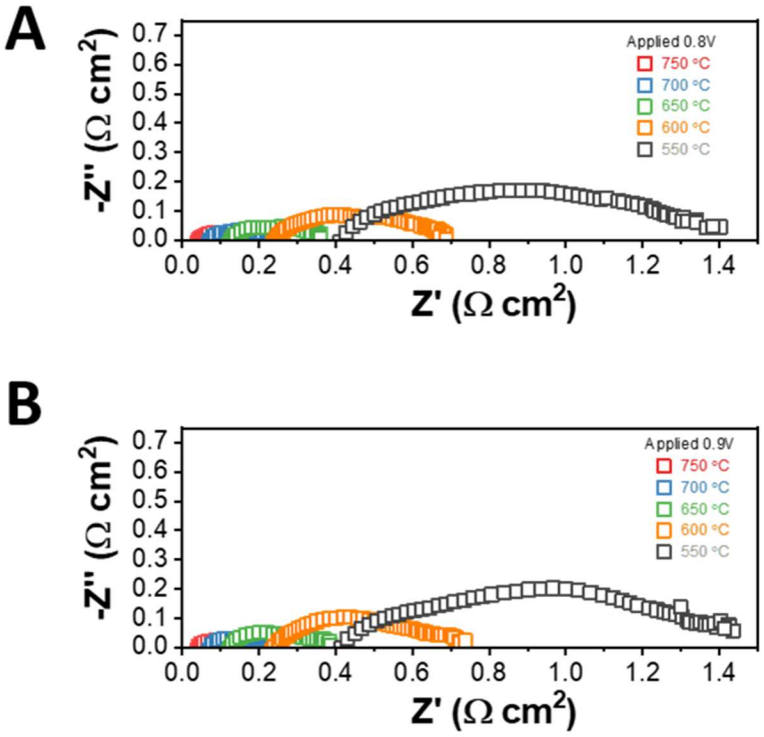

Appendix C Figure C2. MS-SOFC performance in CO_2/CO = 50/50. (A)I-V-P curves at various temperature. (B)EIS spectra at the applied voltage of 0.8 V.

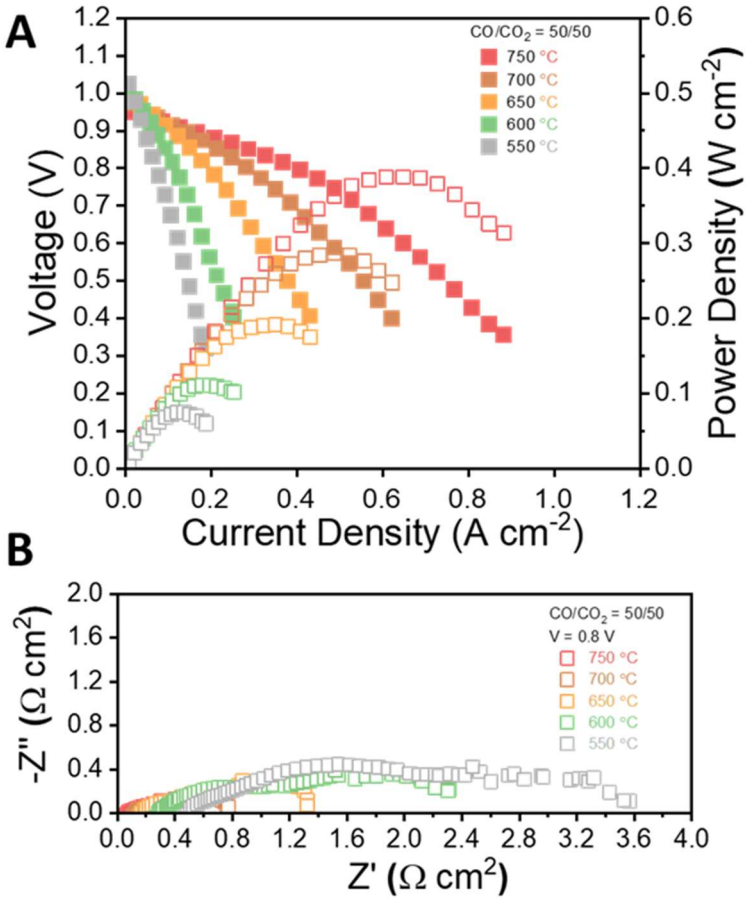

Appendix C Table C1. Peak power densities of single cells with similar fuel electrode and electrolyte components at various temperature in hydrogen fuel.

Single cell components	Temperature (°C)	PPDs (W cm^{-2})	References
Fe-Cr|Ni/YSZ|Ni/GDC|YSZ|LSCF|LSC	750	3.0	129
	700	2.5	
	650	2.0	
Fe-Cr|Ni/YSZ|Ni/GDC|ScYSZ|GDC|LSC	750	1.6	190
	700	1.2	
	650	0.8	
P343L alloy|Ni/SDC|10Sc1CeSZ|PrO_x	700	0.3	191

Ni/YSZ|YSZ|PBSCF-GDC	**750**	**1.4**	[192]
Ni/YSZ|YSZ|GDC|NBCCF/GDC	**750**	**1.0**	[179]
Ni/YSZ|YSZ|GDC|GDC/PBCC	**750**	**1.7**	[31]
Ni/YSZ|YSZ|GDC|LSCF/GDC	**750**	**1.3**	[193]
	700	**0.9**	
	650	**0.5**	
Ni/YSZ|YSZ|LSM/YSZ	**700**	**0.6**	[194]
Ni/YSZ|YSZ|LSCF	**750**	**0.8**	[195]
Ni/YSZ|YSZ|BSCF	**750**	**1.2**	[196]

Appendix C Table C2. ASR_{Ω} and ASR_p of single cells with similar fuel electrode and electrolyte components at OCV and various temperature in hydrogen fuel.

Single cell components	Temperature (°C)	ASR_{Ω} (ohms cm^{-2})	$ASRp$ (ohms cm^{-2})	References
Fe-Cr|Ni/ScYSZ|ScYSZ|PBSCF-BSC	**750**	**0.07**	**0.08**	**This work**
	700	**0.11**	**0.11**	
	650	**0.18**	**0.20**	
	600	**0.36**	**0.45**	
Ni/YSZ|YSZ|SDC|LSCF/BCFN/BCO	**750**	**0.10**	**0.07**	[57]
	700	**0.15**	**0.20**	
	650	**0.20**	**0.43**	
Ni/YSZ|YSZ|GDC|STF/STFC	**750**	**0.09**	**0.27**	[16]
	700	**0.12**	**0.31**	
	650	**0.16**	**0.41**	
	600	**0.23**	**0.62**	
Ni/YSZ|YSZ|LSCF/GDC/PrO_x	**700**	**0.08**	**0.34**	[58]
Ni/YSZ|YSZ|GDC|LSF	**750**	**0.09**	**0.35**	[60]
	700	**0.14**	**0.43**	
	650	**0.24**	**0.64**	
Ni/YSZ|YSZ|LSM-DYSB	**700**	**0.08**	**0.42**	[15]
Ni/YSZ|YSZ|LSCF/GPDC	**700**	**0.23**	**0.30**	[197]

Ni/YSZ|YSZ|GDC|$BaCO_3$/LSCF	**800**	**0.08**	**0.27**	[198]
Ni/YSZ|YSZ|GDC|LSPYB	**750**	**0.10**	**0.34**	[199]
	700	**0.16**	**0.54**	
	650	**0.26**	**0.94**	
Ni/YSZ|YSZ|GDC|LSCF	**750**	**0.10**	**0.60**	[200]
	700	**0.16**	**1.20**	
Ni/YSZ|YSZ|GDC|PNCO-LSCF	**800**	**0.10**	**0.29**	[201]
	750	**0.14**	**0.32**	
	700	**0.18**	**0.42**	

Appendix C Table C3. Current densities of single cells with similar fuel electrode and electrolyte components at various temperature and 1.3 V in steam electrolysis

Single cell components	**Temperature (°C)**	**Current density at 1.3 V (A cm^{-2})**	**References**
Fe/Cr|Ni/ScYSZ|ScYSZ|PBSCF/BSC	**750**	**2.0**	**This work**
	700	**1.5**	
	650	**0.9**	
	600	**0.4**	
Ni/YSZ|YSZ| LSCF/YSZ	**750**	**0.9**	[171]
P434L|Ni/SDC|ScSZ|LSCF-SDC/CMO|P434L	**700**	**0.9**	[141]
Ni/YSZ|YSZ|GDC|PBCC/BCO	**750**	**1.4**	[178]
Ni/YSZ|YSZ|GDC|SSC/SDC	**800**	**4.1**	[12]
	750	**3.1**	
	700	**1.9**	
	650	**1.1**	
Ni/YSZ|YSZ|GDC|LSCF-GDC	**800**	**2.8**	[202]
	750	**1.7**	
	700	**1.3**	
	650	**0.6**	

Ni/LST/GDC|YSZ|GDC|LSCF	**750**	**1.6**	**203**
430L|Ni/SDC/430L/YSZ|SSZ|Nd_2O_3/NNO/SSZ	**800**	**2.0**	**165**
	750	**1.6**	
	700	**1.0**	
	650	**0.6**	
Fe/Cr|LSCC|Ni/YSZ|YSZ|LSM	**800**	**0.8**	**204**
	750	**0.5**	
Ni/Mo|Ni/YSZ|Ni/GDC|LDC|LSGM|LDC|SDC/SSC	**700**	**1.1**	**205**
Ni/YSZ|YSZ|LSM/YSZ	**700**	**0.40**	**169**

Appendix C Table C4. ASR_Ω and ASR_p of single SOECs at OCV condition and various temperature in CO_2 electrolysis.

Single cell components	**Temperature (°C)**	***ASR_Ω* (ohms cm^{-2})**	***ASRp* (ohms cm^{-2})**	**References**
Ni/YSZ|YSZ|GDC/LSCM	900	3.50	0.65	206
Ni/GDC|YSZ|GDC|LSF/GDC	800	0.24	0.08	112
SDC/LSCF|LSGM|SDC|SFMNF-SDC/NiFe	800	0.12	0.31	124
	750	0.14	0.67	
SFM|LSGM|LSCF-GDC	750	N/A	1.83	207
SFCM|LSGM|LSCF-GDC	750	N/A	1.13	207
SFM	800	N/A	1.13	145
SFMF	800	N/A	0.66	208
SFM|LSGM|LSCF/GDC	800	0.50	0.90	209
	750	0.75	1.25	
	700	1.20	3.30	
	650	2.00	6.65	
$CaFe_2O_4$|LSGM|LDC	850	0.24	0.29	153
	800	0.34	0.55	
	750	0.62	1.03	

$Ca_2Fe_2O_5$|LSGM|LDC	850	0.39	0.54	[153]
	800	0.56	0.89	
	750	0.71	1.76	

Appendix C Table C5. ***PPDs*** **of state-of-the-art SOFCs at various temperature utilizing CO as the primary fuel.**

Single cell components	**Temperature (°C)**	**PPDs (W cm^{-2})**	**References**
Ni/YSZ|YSZ/Cu-CeO_2-YSZ	700	0.37	[210]
NiFe-MgO-YSZ|YSZ|LSM-YSZ	800	0.43	[157]
Ni/YSZ|YSZ|YSZ-LSM	850	0.67	[211]
Ni/YSZ|YSZ|SDC|YSZ-LSC	800	0.70	[212]
Ni/YSZ|YSZ|YSZ-LSM	800	0.65	[213]
	700	0.25	
LSFNb|GDC|YSZ/GDC|LSFNb	850	0.34	[214]
	700	0.07	
LSFNb|LSGM|LSFNb	850	0.71	
	700	0.18	

Appendix C Table C6. Stability testing results of CO_2 SOECs reported recently

Cell structure	Temperature(˚C)	Current density (A cm^{-2})	Duration(h)	References
BLC64|LSGM|Ni-Fe-LSFM	800	0.5	98	[215]
NiFe@SFMNi-F−SDCSDC/LSGM//LSCoF−SDC	750	0.35	140	[124]
SFMSDC|LSGM|LSCF-SDC	800	1.1	105	[209]
CoFe@LSCFM-GDC|LSGM|LSCF-GDC	800	0.65	100	[151]

PBCFM-GDC|LDC|LSGM|PBSCF-GDC	750	0.78	100	[107]
SFMN-SDC|SDC|YSZ|LSM-YSZ	800	1.16	500	[144]
$FeNi_3$@SFMN-GDC|LDC|LSGM|LSCF-GDC	800	0.37	40	[146]
CoFe-STCF-SDC|LSGM|LSC-SDC-PrOx	800	0.5	100	[125]
Ni/Cr_2O_3LSTMN|LSGM|BSCF	800	0.75	50	[155]
PSNFM-NFA@FeO|LSGM|LSCG-GDC	800	0.5	500	[108]

Appendix C Table C7. Low-temperature electrolysis and molten carbonate literature shown in Figure 6A and 6B.

Symbol	Authors	Temperature	CO_2 gas feed	Reference
	Pan et al.	room temperature	humidified CO_2	[163]
	Seong et al.	room temperature	humidified CO_2	[156]
	Yin et al.	30-80 °C	humidified CO_2	[216]
	Zheng et al.	room temperature	humidified CO_2	[217]
	Monteiro et al.	room temperature	humidified CO_2	[84]
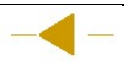	Haas et al.	30 °C	humidified CO_2	[218]
	Kaplan et al.	900 °C	pure CO_2	[219]